

FIG. 5. (Color online) Compressive stress dependence of  $\varepsilon'$  and  $\tan \delta$  at a frequency of 100 kHz for the samples of (a) CCTO-Ar and (b) 25% after annealing at 1000 °C for 5 h under flowing argon. The insets of Figs. 5(a) and 5(b) show the absolute change (%) of  $\varepsilon'$  and  $\tan \delta$ . Here,  $\%|\Delta\varepsilon'|$  and  $\%|\Delta \tan \delta|$  are defined as  $|(\varepsilon'_{\sigma} - \varepsilon'_{0})/\varepsilon'_{0}| \times 100(\%)$  and  $|(\tan \delta_{\sigma} - \tan \delta_{0})/\tan \delta_{0}| \times 100(\%)$ , respectively, where  $(\varepsilon'_{\sigma}, \varepsilon'_{0})$ , and  $(\tan \delta_{\sigma}, \tan \delta_{0})$ , are the dielectric constants and dissipation factors with the applied compressive stress and without the applied compressive stress, respectively.

in  $\epsilon'$  was observed for 25%LTNO-Ar. The dielectric properties of both CCTO-Ar and 25%LTNO-Ar samples change significantly with the applied compressive stress, and this can be explained by the stress-induced aging mechanism. The different bases in dielectric behaviors of the two ceramics can be explained by the level of concentration of oxygen vacancies in the grain boundaries after postsintering annealing.

# **ACKNOWLEDGMENTS**

This work is financially supported by The Thailand Research Fund (TRF), and The Commission on Higher Educa-

tion (CHE), The Ministry of Education, Thailand. P.T. would like to thank the Thailand Graduate Institute of Science and Technology (TGIST) for his PhD scholarship.

- <sup>1</sup>M. A. Subramanian, D. Li, N. Duan, B. A. Reisner, and A. W. Sleight, J. Solid State Chem. **151**, 323 (2000).
- <sup>2</sup>A. P. Ramirez, M. A. Subramanian, M. Gardela, G. Blumberg, D. Li, T. Vogt, and S. M. Shapiro, Solid State Commun. 115, 217 (2000).
- <sup>3</sup>C. C. Homes, T. Vogt, S. M. Shapiro, S. Wakimoto, and A. P. Ramirez, Science 293, 673 (2001).
- <sup>4</sup>J. Wu, C. W. Nan, Y. Lin, and Y. Deng, Phys. Rev. Lett. **89**, 217601 (2002).
- Maensiri, P. Thongbai, and T. Yamwong, Acta Mater. 55, 2851 (2007).
   Lin, J. Wang, L. Jiang, Y. Chen, and C. W. Nan, Appl. Phys. Lett. 85, 5664 (2004)
- <sup>7</sup>P. K. Jana, S. Sarkar, and B. K. Chaudhuri, Appl. Phys. Lett. **88**, 182901 (2006).
- Y. Lin, L. Jiang, R. Zhao, and C. W. Nan, Phys. Rev. B 72, 014103 (2005).
   X. Kuang, C. Bridges, M. Allix, J. B. Claridge, H. Hughes, and M. J. Rosseinsky, Chem. Mater. 18, 5130 (2006).
- <sup>10</sup>S. Sarkar, P. K. Jana, B. K. Chaudhuri, and H. Sakata, Appl. Phys. Lett. 89, 212905 (2006)
- <sup>11</sup>S. Maensiri, P. Thongbai, and T. Yamwong, Appl. Phys. Lett. **90**, 202908 (2007).
- <sup>12</sup>D. C. Sinclair, T. B. Adams, F. D. Morrison, and A. R. West, Appl. Phys. Lett. **80**, 2153 (2002).
- <sup>13</sup>S. Y. Chung, I. L. D. Kim, and S. J. L. Kang, Nat. Mater. 3, 774 (2004).
- <sup>14</sup>B. A. Bender and M. J. Pan, Mater. Sci. Eng., B 117, 339 (2005).
- <sup>15</sup>C. C. Wang and L. W. Zhang, Appl. Phys. Lett. 88, 042906 (2006).
- <sup>16</sup>C. C. Wang and L. W. Zhang, Phys. Rev. B 74, 024106 (2006).
- <sup>17</sup>P. Thongbai, C. Masingboon1, S. Maensiri, T. Yamwong, S. Wongsaenmai, and R. Yimnirun, J. Phys.: Condens. Matter 19, 236208 (2007).
- <sup>18</sup>R. Yimnirun, P. J. Moses, R. J. Mayer, and R. E. Newnham, Rev. Sci. Instrum. 74, 3429 (2003).
- <sup>19</sup>C. C. Wang, Y. J. Yan, L. W. Zhang, M. Y. Cui, G. L. Xie, and B. S. Cao, Scr. Mater. **54**, 1501 (2006).
- <sup>20</sup>S. F. Shao, J. L. Zhang, P. Zheng, W. L. Zhong, and C. L. Wang, J. Appl. Phys. **99**, 084106 (2006).
- <sup>21</sup>J. Liu, Y. Sui, C. G. Duan, W. N. Mei, R. W. Smith, and J. R. Hardy, Chem. Mater. 18, 3878 (2006).
- <sup>22</sup>J. L. Zhang, P. Zheng, C. L. Wang, M. L. Zhao, J. C. Li, and J. F. Wang, Appl. Phys. Lett. 87, 142901 (2005).
- <sup>23</sup>L. Zhang and Z. J. Tang, Phys. Rev. B **70**, 174306 (2004).
- <sup>24</sup>A. R. West, T. B. Adams, F. D. Morrison, and D. C. Sinclair, J. Eur. Ceram. Soc. **24**, 1439 (2004).
- <sup>25</sup>G. Chiodelli, V. Massarotti, D. Capsoni, M. Bini, C. B. Azzoni, M. C. Mozzati, and P. Lupotto, Solid State Commun. 132, 241 (2004).
- <sup>26</sup>D. Capsoni, M. Bini, V. Massarotti, G. Chiodelli, M. C. Mozzatic, and C. B. Azzoni, J. Solid State Chem. 177, 4494 (2004).
- <sup>27</sup>C. Masingboon, S. Maensiri, T. Yamwong, P. Anderson, and S. Seraphin, Appl. Phys. A: Mater. Sci. Process. 91, 87 (2008).
- <sup>28</sup>M. Li, A. Feteira, D. C. Sinclair, and A. R. West, Appl. Phys. Lett. **88**,
- 232903 (2006). <sup>29</sup>T. B. Adams, D. C. Sinclair, and A. R. West, J. Am. Ceram. Soc. **89**, 10
- (2006).

  30P. R. Bueno, M. A. Ramírez, J. A. Varela, and E. Longo, Appl. Phys. Lett.
- 89, 191117 (2006).
- <sup>31</sup>R. Yimnirun, M. Unruan, Y. Laosiritaworn, and S. Ananta, J. Phys. D: Appl. Phys. 39, 3097 (2006).



Contents lists available at ScienceDirect

# **Solid State Communications**

journal homepage: www.elsevier.com/locate/ssc



# Correlation between giant dielectric response and electrical conductivity of CuO ceramic

Prasit Thongbai<sup>a</sup>, Teerapon Yamwong<sup>b</sup>, Santi Maensiri<sup>a,\*</sup>

- <sup>a</sup> Department of Physics, Khon Kaen University, Khon Kaen, 40002, Thailand
- <sup>b</sup> National Metals and Materials Technology Center (MTEC), Thailand Science Park, Pathumthani, 12120, Thailand

#### ARTICLE INFO

Article history: Received 30 May 2008 Accepted 17 June 2008 by A.H. MacDonald Available online 20 June 2008

PACS: 68.37.Hk 77.22.Ch 77.22.Gm 77.84.Bw

Keywords:

A. Insulators C. Crystal structure C. Grain boundaries D. Dielectric response

## ABSTRACT

The correlation between high dielectric response and electrical conductivity in CuO ceramic was investigated. The dielectric dispersion was in good agreement with the Debye-like relaxation model at low temperature, but it deviated from the model at low frequencies as the temperature increased. High- $\varepsilon'$  response in our CuO ceramic was attributed to the contributions of grain and GB corresponding to the grain and GB conductivity relaxations, respectively. The conductivity of GB was found to increase with increasing dc bias.

© 2008 Elsevier Ltd. All rights reserved.

In recent years, high dielectric materials have been attracting much attention due to their potential applications in the microelectronic industry. These materials include CaCu<sub>3</sub>Ti<sub>4</sub>O<sub>12</sub> [1-11],  $\text{Li}_x\text{Ti}_y\text{Ni}_{1-x-y}\text{O}$  [12,13], and CuO [14]. Among them, CuO is of great interest because it is a low cost, lead free environmentally friendly material, and is simple compound which is easy to prepare in the pure form and is available commercially on a large scale [15]. So far, only a few studies have reported on the dielectric properties and the origin of high-  $\varepsilon'$  of CuO ceramics [14–16]. Most recently, we reported the giant dielectric constant  $\varepsilon'$  of  $\sim 2.8-3.7\times 10^4$ observed in high purity CuO (99.999%) ceramics with grain sizes of  $4.57 \pm 1.71$  and  $9.57 \pm 3.01 \,\mu m$  [17]. The  $\varepsilon'$  and  $E_a$  were found to increase with an increase in grain size, due to the different electrical properties in the grains. The high dielectric response observed in these CuO ceramics can be described by the IBLC model. We also observed that the resistance of grain boundaries  $(R_{gb})$  and the dielectric constant of the CuO samples decrease with increasing dc bias due to the decrease of grain boundaries capacitance, whereas the resistance of grains  $(R_g)$  remains constant.

It is known that the measurements of ac conductivity can provide the underlying mechanisms of relaxation and also give a

straightforward method to separate the contributions of grain, GB, and electrodes through their frequency and/or temperature dependent response characteristics [18]. Understanding of ac conduction mechanisms can describe the grain and GB contributions to the overall electrical conductivity of materials. To date, only a few studies have reported on the ac conductivity response of high- $\varepsilon'$  CuO ceramic, which is closely related to the formation of high permittivity in CuO ceramic.

In this study, we report the relationship between high- $\varepsilon'$  response and electrical conductivity in CuO ceramic. The results indicate that both the grain and GB contributions are responsible for the high- $\varepsilon'$  value at low and high temperatures, respectively. Both contributions have connections with the apparent grain and GB conductivity relaxations, respectively. Our results also demonstrate that the conductivity of GB strongly increase with increasing the dc bias.

High purity CuO (99.999%, Cerac) powder was used to fabricate a polycrystalline CuO ceramic. The CuO powder was pressed into disk and then sintered at 920 °C for 10 h. The sintered CuO ceramic was characterized by X-ray diffraction (XRD) (Philips PW3040, The Netherlands) and scanning electron microscopy (SEM) (LEO 1450VP, UK). The disk-shaped ceramic sample was polished and electroded by silver paint on both sides. It was allowed to dry overnight. The dielectric response of the sample was measured using a Hewlett Packard 4194A impedance gain phase analyzer

<sup>\*</sup> Corresponding author. Tel.: +66 43 202222; fax: +66 43 202374. E-mail addresses: sanmae@kku.ac.th, santimaensiri@gmail.com (S. Maensiri).

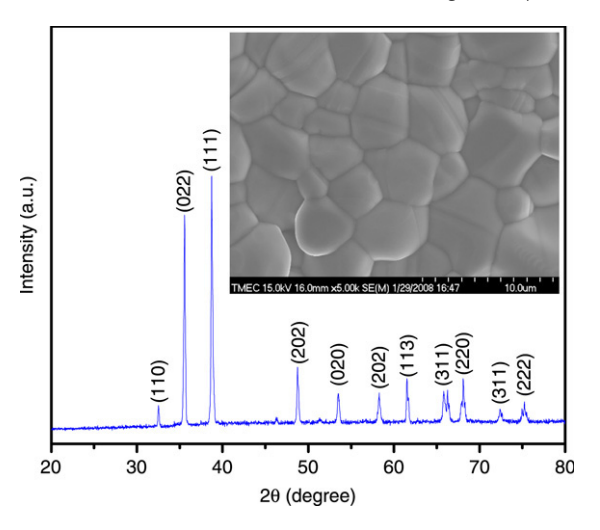


**Fig. 1.** XRD pattern of polycrystalline CuO ceramic; inset is the SEM micrograph of the surface for CuO ceramic.

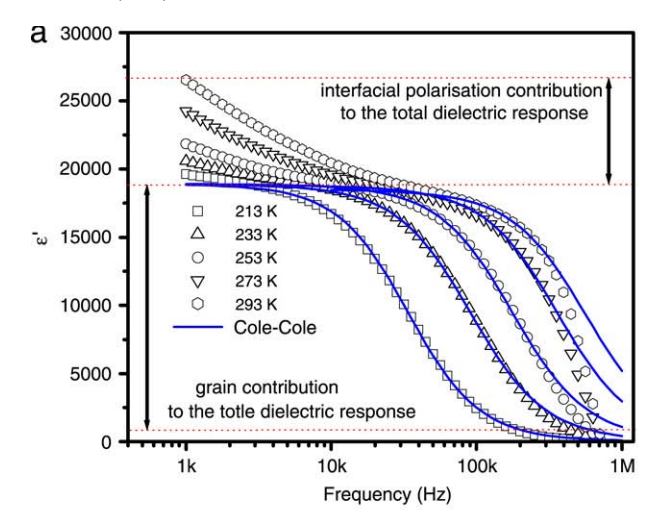
over the frequency ranging from 1 kHz to 1 MHz and at the oscillation voltage of 1.0 V. The measurements were performed over the temperature ranging from 213 to 353 K using an inbuilt cooling–heating system. Each measured temperature was kept constant with an accuracy of  $\pm 1$  K.

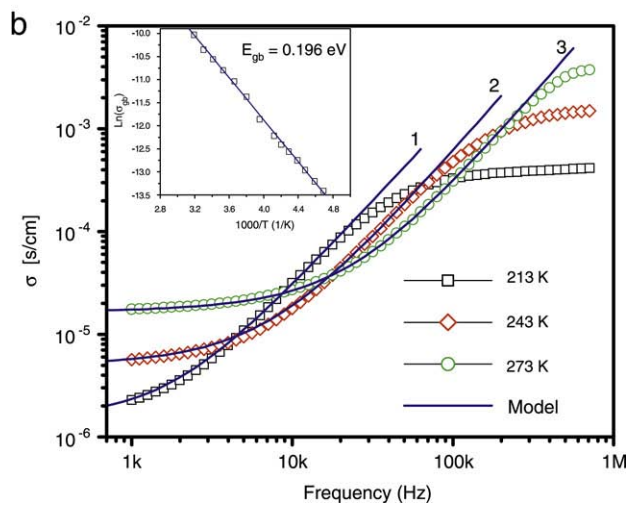
Fig. 1 shows XRD pattern of the CuO ceramic, confirming a main phase of monoclinic CuO (JCPDS card no. 80-0076). As illustrated by the SEM image in the inset of Fig. 1, the CuO ceramic is dense having obvious grain and GB structures. The mean grain size is about  $4.57\pm1.71~\mu m$ .

Fig. 2(a) shows frequency dependence of giant- $\varepsilon'$  as a function of temperature. It is seen that  $\varepsilon'$  shows a Dabye-like relaxation, i.e.,  $\varepsilon'$  decreases dramatically at the frequency where  $\varepsilon''$  shows a relaxation peak, and the relaxation peak in the sample shifts to higher frequency at higher temperature (does not present). This implies that the polarization may fully develop at sufficiently low applied frequencies at fixed temperature, but if the frequency of the applied field is too high then the field is reversed before the polarization responds. However, when the temperature is high, the rate of polarization formed is quick, and thus the relaxation occurs in high frequency. Normally, dielectric relaxation can be empirically described by Debye-like or Cole-Cole relaxation [19]. To understand the physical nature of the giant- $\varepsilon'$  as mentioned above, the frequency dependence of giant- $\varepsilon'$  was plotted, and these data were fitted to the Cole-Cole equation:

$$\varepsilon^* = \varepsilon' - j\varepsilon'' = \varepsilon_{\infty} + \frac{\varepsilon_{s} - \varepsilon_{\infty}}{1 + (j\omega\tau)^{1-\alpha}},\tag{1}$$

where  $\varepsilon_{\rm s}$  and  $\varepsilon_{\infty}$  are respectively the static and high frequency limits of dielectric permittivity,  $\tau$  is the relaxation time, and  $\alpha$  is a constant (0  $\leq \alpha \leq$  1). For an ideal Debye relaxation,  $\alpha =$  0. If  $\alpha > 0$ , it implies that the relaxation has a distribution of relaxation times, leading to a broader peak shape than a Debye peak. As shown in Fig. 2(a), a nearly monodispersive nature of dielectric relaxation is observed in our CuO ceramic with a very small  $\alpha$  parameter (0.05–0.07). The rapid decrease in  $\tau$  (from 4.70 to 0.22  $\mu$ s) with increasing temperature (from 213 to 293 K) is suggestive of an increasing dipole density and faster polarization process [12]. From the fitted results, the dielectric relaxation in CuO ceramic can be concluded as a nearly Debye relaxation, which is attributed to the dipole relaxation related to the defects in the grain interiors or other motions which do not involve long-range displacement of mobile charge carriers [16]. Note that, at low temperature the experimental curves are quite well fitted using Eq. (1). However, with increased temperature, a disagreement between them could





**Fig. 2.** (a) The frequency dependence of  $\varepsilon'$  for CuO ceramic at various temperatures; the solid lines represent calculated values of Eq. (1), assuming a Cole–Cole model. (b) ac conductivity as a function of frequency at various temperatures of CuO ceramics and the solid lines 1–3 are the fittings according to Eq. (2); inset is the Arrhenius plot of the conductivity of the grain boundary.

be observed at low frequencies. This might be attributed to the GB effect, and it can be responsible for up to 30% (at 1 kHz and 293 K) of the total  $\varepsilon'$  of CuO ceramic.

To clarify the electrical conductivity in our polycrystalline CuO ceramic, electrical properties were further characterized by ac conductivity. As demonstrated in Fig. 2(b), there are two plateaus of behavior. First, the plateau at higher frequencies with the conductivity does not increase rapidly at high frequency and is referred to as the bulk conductivity relaxation [20]. This region shifts to higher frequencies as the temperature increases and it moves out of the frequency range of our experiment at higher temperatures (>273 K). Second, at low frequencies, another plateau can be observed. Here, it is referred to as the GB conductivity relaxation [18], and this can be ascribed by the relation

$$\sigma = \sigma_{gb} + A_1 f^p + A_2 f^q, \tag{2}$$

where  $\sigma_{gb}$  is GB conductivity and the parameter  $A_1$ ,  $A_2$ , p, and q are constants. In Eq. (2), the  $\sigma_{gb} + A_1 f^p$  term describes the grain-boundary conductivity relaxation [21]. With f increasing, the conductivity of CuO ceramic changes from the GB conductivity relaxation to the bulk conductivity relaxation [21]. In Fig. 2(b), the solid lines 1–3 are the fitting curves according to Eq. (2). Interestingly, we have observed that the exponents p and q

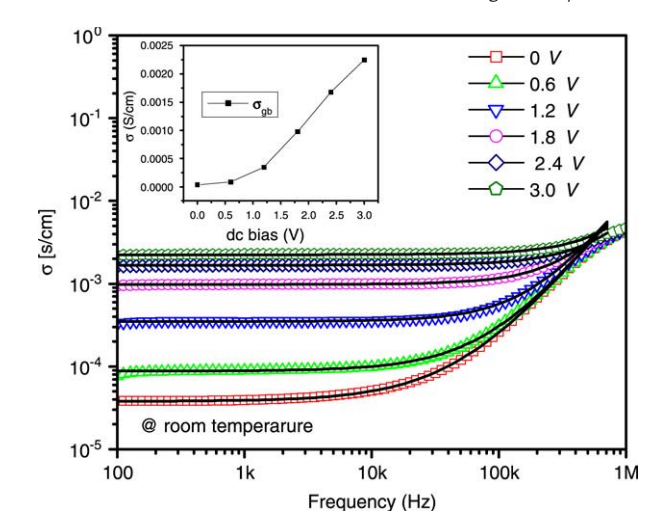


**Fig. 3.** Frequency dependence of conductivity  $\sigma$  at room temperature under different dc bias electric field for CuO ceramic; inset is the frequency dependence of  $\varepsilon'$  for under 0–3 dc bias.

vary from 0.85 to 0.94 and 1.69 to 2, respectively. The value of  $A_1$  increases from 7.8  $\times$  10<sup>-10</sup> to 2.5  $\times$  10<sup>-9</sup> S/cm, while the value of  $A_2$  decreases from 4.8  $\times$  10<sup>-12</sup> to 1.5  $\times$  10<sup>-14</sup> as temperature increases from 213 to 323 K. Note that the fitted  $\sigma_{gb}$  values followed Arrhenious-like equation (inset of Fig. 2(b)),  $\sigma = \sigma_1 \exp(-E_a/k_BT)$  [20], and the activation energy for conduction at GB was obtained to be 0.196 eV. This value is little higher than that of the activation energy required for relaxation, 0.184 eV (does not present) which  $\tau$  is obtained from the fitted values using Eq. (1).

The influence of dc bias on ac conductivity of CuO ceramic was also studied, as presented in Fig. 3. The solid lines 1–3 are the experimental results showing curves fitted according to Eq. (2). The underlying fitted  $\sigma_{gb}$  values, shown in the inset of Fig. 3, increase from  $3.80 \times 10^{-5}$  to  $2.25 \times 10^{-3}$  S/cm as the dc bias increases from 0 to 3 V, revealing the strong electric field dependent nature of  $\sigma_{gb}$ .

We now turn to see the relationship between the observed high- $\varepsilon'$  and the related conduction in CuO ceramic. As shown in Fig. 2(a), there are two main contributions to the high- $\varepsilon'$  response in CuO ceramic: grain and GB contributions. Based on a Debyelike relaxation model, our measured data at low temperature was found to be in good agreement with the model and this indicates that the dielectric response in such material is associated with the permanent dipole orientation and/or the short-range displacement of mobile charge carriers inside the grains [22]. However, the displacement of charge carriers is most likely to be responsible for the dielectric response in CuO ceramic due to the presence of the microscopic amount of Cu<sup>3+</sup> inside the grains [15,16]. This corresponds to the observed bulk conductivity relaxation at low temperature, as shown in Fig. 2(b). Moreover, we think that the presence of defects (such as oxygen vacancies) and existence of domain boundaries (DBs) inside the grains might be responsible for the high- $\varepsilon'$  at low temperature. However, the evidence of such defects and DBs is beyond the scope of our work and further work is needed to make a more detailed explanation. When the temperatures increased, the experimental data deviated from the model at low frequencies. We attribute the deviated data to the effect of the GB dielectric response, which is confirmed by the observed plateau at low frequencies for GB conductivity relaxation, as shown in Fig. 2(b). With the temperature increasing, more charges accumulate at the two sides of the boundary layer, which is responsible for the higher magnitude of the interfacial polarization and contributing to the total dielectric value of CuO ceramic.

In conclusion, high- $\varepsilon'$  dispersion observed in CuO ceramic can be ascribed by a Debye-like relaxation model. High- $\varepsilon'$  response in our CuO ceramic is attributed to the contributions of grain and GB corresponding to the grain and GB conductivity relaxations, respectively. Our result also reveals that the resistance of GB increases with increasing dc bias.

# Acknowledgements

The authors would like to thank the Thai Microelectronics Center (TMEC) for FE-SEM facilities. PT would like to thank the Thailand Graduate Institute of Science and Technology (TGIST) for his PhD scholarship. This work is financially supported by The Thailand Research Fund (TRF), and The Commission on Higher Education (CHE), The Ministry of Education, Thailand.

# References

- [1] M.A. Subramanian, D. Li, N. Duan, B.A. Reisner, A.W. Sleight, J. Solid State Chem. 151 (2000) 323.
- [2] D.C. Sinclair, T.B. Adams, F.D. Morrison, A.R. West, Appl. Phys. Lett. 80 (2002) 2153.
- [3] S.Y. Chung, I.L.D. Kim, S.J.L. Kang, Nat. Mater. 3 (2004) 774.
- [4] P. Lunkenheimer, R. Fichtl, S.G. Ebbinghaus, A. Loidl, Phys. Rev. B. 70 (2004) 172102.
- [5] S. Maensiri, P. Thongbai, T. Yamwong, Appl. Phys. Lett. 90 (2007) 202908.
- [6] S.F. Shao, J.L. Zhang, P. Zheng, W.L. Zhong, C.L. Wang, J. Appl. Phys. 99 (2006) 084106.
- [7] P. Thongbai, C. Masingboon, S. Maensiri, T. Yamwong, S. Wongsaenmai, R. Yimnirun, J. Phys. Condens. Matter. 19 (2007) 236208.
   [8] C. Masingboon, S. Maensiri, T. Yamwong, P.L. Anderson, S. Seraphin, Appl. Phys.
- A 91 (2008) 87.

  [9] C. Masingboon, P. Thongbai, S. Maensiri, T. Yamwong, S. Seraphin, Mater.
- Chem. Phys. 109 (2008) 262. 10] T.T. Fang, H.K. Shiau, J. Amer. Ceram. Soc. 87 (2004) 2027.
- [11] D. Capsoni, M. Bini, V. Massarotti, G. Chiodelli, M.C. Mozzati, C.B. Azzoni, J. Solid State Chem. 177 (2004) 4494.
- [12] J. Wu, C.W. Nan, Y. Lin, Y. Deng, Phys. Rev. Lett. 89 (2002) 217601.
- [13] S. Maensiri, P. Thongbai, T. Yamwong, Acta Mater. 55 (2007) 2851.
- [14] S. Sarkar, P.K. Jana, B.K. Chaudhuri, H. Sakata, Appl. Phys. Lett. 89 (2006) 212905.
- [15] S. Sarkar, P.K. Jana, B.K. Chaudhuri, Appl. Phys. Lett. 92 (2008) 022905.
- [16] S. Sarkar, P.K. Jana, B.K. Chaudhuri, Appl. Phys. Lett. 92 (2008) 142901.
- [17] P. Thongbai, S. Meansiri, T. Yamwong, Effects of grain, grain boundary, and dc electric field on giant dielectric response in high purity CuO ceramics, J. Appl. Phys. 104 (2) (2008) (in press).
- 18] W. Li, W.R. Schwartz, Appl. Phys. Lett. 89 (2006) 242906.
- [19] K.S. Cole, R.H. Cole, J. Chem. Phys. 9 (1941) 342.
- [20] L. Zhang, Z.J. Tang, Phys. Rev. B. 70 (2004) 174306.
- [21] L. Zhang, Appl. Phys. Lett. 87 (2005) 022907.
- 22] D. Ming, J.M. Reau, J. Ravez, J. Gitae, P. Hagenmuller, J. Solid State Chem. 116 (1995) 185.

J. Phys.: Condens. Matter **20** (2008) 395227 (11pp)

# Dielectric relaxation and dielectric response mechanism in (Li, Ti)-doped NiO ceramics

Prasit Thongbai $^1$ , Suwat Tangwancharoen $^1$ , Teerapon Yamwong $^2$  and Santi Maensiri $^{1,3}$ 

<sup>1</sup> Small & Strong Materials Group (SSMG), Department of Physics, Faculty of Science, Khon Kaen University, Khon Kaen 40002, Thailand

E-mail: sanmae@kku.ac.th and santimaensiri@gmail.com

Received 2 April 2008, in final form 5 August 2008 Published 4 September 2008 Online at stacks.iop.org/JPhysCM/20/395227

#### Abstract

Giant dielectric permittivity (Li, Ti)-doped NiO (LTNO) ceramics are prepared by a simple PVA sol-gel method. The dielectric properties are investigated as a function of frequency (10<sup>2</sup>–10<sup>6</sup> Hz) at different temperatures (233–473 K). The concentration of Li has a remarkable effect on the dielectric properties of the LTNO ceramics. The modified Cole-Cole equation, including the conductivity term, is used to describe the experimental dielectric spectra of a high permittivity response with excellent agreement over a wide range of frequencies (10<sup>3</sup>–10<sup>6</sup> Hz) and temperatures (233-313 K). A frequency dielectric dispersion phenomenon in an LTNO ceramic is also analyzed by impedance spectroscopy. A separation of the grain and grain boundary properties is achieved using an equivalent circuit model. The grain and grain boundary conduction and the dielectric relaxation time of the Li<sub>0.05</sub>Ti<sub>0.02</sub>Ni<sub>0.93</sub>O follows the Arrhenius law associated with estimated activation energies of 0.216, 0.369 and 0.391 eV, respectively. Through the analysis by the modified relaxation model and impedance spectroscopy, it is strongly believed that the high dielectric permittivity response of the LTNO is not only contributed by the space charge polarization (Maxwell–Wagner polarization) mechanism at low frequency regions, but also by the defect-dipole polarization mechanism at high frequency regions.

1

(Some figures in this article are in colour only in the electronic version)

# 1. Introduction

High permittivity Bi/Pb-free dielectric materials with good thermal stability have particularly attracted ever-increasing attention for their practical applications in microelectronics such as capacitors and memory devices. These materials include  $CaCu_3Ti_4O_{12}$  (CCTO) [1], some Fe-containing complex perovskites  $A(Fe_{1/2}B_{1/2})O_3$  (A=Ba, Sr, Ca and B=Nb, Ta, Sb) [2, 3], (M, N)-doped NiO (M=Li, Na, K and N=Ti, Al, Si, Ta) [4–10] and CCTO–LTNO composites [11]. They generally exhibit a very high and nearly temperature-independent dielectric permittivity at evaluated

temperatures. Several models have been already proposed to explain the origin of high dielectric permittivity (high  $\varepsilon'$ ) in these compounds [12–15]. Nowadays, it is generally accepted that high  $\varepsilon'$  in CCTO ceramics are electrically heterogeneous consisting of semiconducting grains and insulating grain boundaries [16]. Therefore, high  $\varepsilon'$  in the CCTO is associated with an internal barrier layer capacitance (IBLC) effect due to the development of Schottky barriers at grain boundaries rather than being due to an intrinsic contribution. Hence, polarization effects at insulating grain boundaries between semiconducting grains or other internal barriers generate extrinsic high  $\varepsilon'$ , accompanied by a strong Maxwell–Wagner (MW) relaxation mode. However, some fundamental questions regarding

<sup>&</sup>lt;sup>2</sup> National Metals and Materials Technology Center (MTEC), Thailand Science Park, Pathumthani 12120, Thailand

<sup>&</sup>lt;sup>3</sup> Author to whom any correspondence should be addressed.

the composition–property relationships remain unanswered. For example, what is the origin and composition of the semiconductive grain and insulating grain boundary in CCTO? For other high- $\varepsilon'$  materials apart from CCTO, a grain boundary (internal) barrier layer capacitor has also been evoked to explain these high permittivity phenomena.

For nonperovskite materials (M, N)-doped NiO (M =Li, Na, K and N = Ti, Al, Si, Ta), it is now widely accepted that the high  $\varepsilon'$  at radio frequencies near room temperature is associated with the IBLC effect, arising from core/shell structure, which induces Maxwell-Wagner polarization (i.e. interfacial polarization) at the interfaces between grains (semiconducting/high conducting region) and grain boundaries (insulating/low conducting region) [4, 7, 17, 18]. The N dopant is rich on the grain boundaries (indigent within the grains) and forms a second phase, which acts as an insulator enclosing the core of the grain, which is semiconductive M-doped NiO particles, and the polarization relaxation is closely related to the conductivity in the grain interior [17]. Raevski et al [2] have suggested that the effective dielectric permittivity ( $\varepsilon'$ ) of the core/shell structure at very low frequency can be estimated as  $\varepsilon' \approx \varepsilon_2(t+d)/d$ , where  $\varepsilon_2$  is the dielectric permittivity of the grain boundary (shell) and t and d are the size of the conducting grain (core) and the thickness of the shell, respectively. This relation is consistent with the experimental results, reported by Wu et al [4]. Namely, the dielectric permittivity of LTNO ceramics decreases with increasing Ti dopant (d increased). In contrast, Zhang et al [19] reported that high dielectric permittivity of an (Li, Ti)-doped NiO thin film with 200 nm in thickness increases with increasing Ti content. Moreover, Lin et al [18] have proposed that the huge dielectric permittivity response of  $Li_xTi_yNi_{1-x-y}O$  (LTNO) could also be enhanced by the polarization of defect dipoles. Therefore, the Ti-dopant in LTNO ceramics and thin films may not only act as insulator, which restricts the long-range migration of charge carriers, but also contributes to the dielectric properties.

Unfortunately, only a few studies have focused on the defect-dipole polarization response of these materials to characterize relaxation processes, which are closely related to the formation of high permittivity in LTNO ceramics. Most recently, we reported that the polymerized complex (PC) method can be used to synthesize  $\sim\!39$  nm nanoparticles of Li<sub>0.3</sub>Ti<sub>0.02</sub>Ni<sub>0.68</sub>O and to fabricate ceramics showing  $\varepsilon'\sim10^5-10^6$ . However, the Li<sub>0.3</sub>Ti<sub>0.02</sub>Ni<sub>0.68</sub>O powders prepared by this method contained some second phase (i.e. Ni).

In this paper, a nonperovskite and nonferroelectric high permittivity core/shell structured materials, Li and Ti co-doped NiO ( $\text{Li}_x\text{Ti}_{0.02}\text{Ni}_{0.98-x}\text{O}$ , where x=0.05 0.10 and 0.20), are successfully synthesized by a simple polyvinyl alcohol (PVA) sol–gel method. The PVA sol–gel method is a chemical solution process, which has received considerable attention due to its relative simplicity and usefulness for obtaining a homogeneous and fine powder precursor [20]. The synthesized fine LTNO powders and ceramics are characterized by x-ray diffraction (XRD) and scanning electron microscopy (SEM). The high dielectric permittivity and its relaxation were investigated on the LTNO ceramics. It is suggested that

such a high dielectric response of LTNO could be partially enhanced by the IBLC mechanism through MW relaxation at low frequency (<1 kHz), and partially associated with the polarization of defect dipoles above 1 kHz. Both contributing factors are thermally activated mechanisms.

# 2. Experimental details

Ni(NO<sub>3</sub>)<sub>2</sub>·6H<sub>2</sub>O (99.9%, Kento), LiNO<sub>3</sub> (98%, Panreac), titanium(diisopropoxide) bis(2,4-pentanedionate) 75 wt% in 2-propanol (C<sub>16</sub>H<sub>28</sub>O<sub>6</sub>Ti, Ti solution) (99%, Acros), citric acid (C<sub>6</sub>H<sub>8</sub>O<sub>7</sub>·H<sub>2</sub>O, 99%, BDH) and polyvinyl alcohol (PVA)  $([-CH_2CHOH_{-}]_n, M_n$ = 72 000, Fluka) were employed as starting raw materials. The polycrystalline LTNO ceramic samples with different contents of Li, i.e.  $Li_{0.05}Ti_{0.02}Ni_{0.93}O$  (LTNO-05),  $Li_{0.10}Ti_{0.02}Ni_{0.88}O$  (LTNO-05) 10) and  $Li_{0.20}Ti_{0.02}Ni_{0.78}O$  (LTNO-20) were designed and prepared by the following procedure. Firstly, 5 g of citric acid was dissolved in 95 ml of distilled water (CA solution) with constant stirring using a magnetic stirrer at room temperature, and then 5 g of PVA was added to this solution by stirring at 473 K to obtain the polymer solution network. Secondly, stoichiometric amounts of Ni(NO<sub>3</sub>)<sub>2</sub>·6H<sub>2</sub>O and LiNO<sub>3</sub> were added to this solution. Subsequently, Ti solution was slowly added into the mixed solution, followed by stirring and heating at 353 K to form the transparent gel. Note that the ratio of CA solution: PVA: total amount of the precursors is about 100:5:10 wt%. Then, the gel precursor was dried at 393 K overnight. To obtain the LTNO powders, the dried gel was ground and later calcined at 923 K for 10 h in air. The resulted powders were pressed into pellets 16 mm in diameter and  $\sim$ 1– 2 mm in thickness by a uniaxial pressing method at 200 MPa. Finally, these pellets were sintered at 1523 K for 5 h in air.

To reveal the phase composition and microstructure, the LTNO powders and ceramics were characterized by x-ray diffraction (XRD) (Philips PW3040, The Netherlands), energy-dispersive spectroscopy (EDS), and scanning electron microscopy (SEM) (LEO 1450VP, UK), respectively. The ceramic samples were polished and electroded by silver paint on both sides of the disc-shaped samples. They were allowed to dry overnight. The dielectric response of the samples was measured using a Hewlett Packard 4194A impedance gain phase analyzer over the frequency ranges from 100 Hz to 1 MHz and at the oscillation voltage of 1.0 V. The measurements were performed over the temperature ranges from 233 to 473 K using an inbuilt cooling–heating system. Each measured temperature was kept constant with an accuracy of  $\pm 1~\rm K$ .

The complex impedance  $(Z^*)$  of the samples was calculated from the relation

$$\varepsilon^* = \varepsilon' - j\varepsilon'' = \frac{1}{j\omega C_0 Z^*} \tag{1}$$

where  $\varepsilon'$  and  $\varepsilon''$ , respectively, are the real part and imaginary part of the complex permittivity  $(\varepsilon^*)$ .  $\omega$  is the angular frequency  $(\omega=2\pi f)$  and  $\mathrm{j}=\sqrt{-1}$ .  $C_0=\varepsilon_0 S/d$  is the empty cell capacitance, where S is the sample area and d is the sample thickness. The values of ac conductivity  $(\sigma_{\mathrm{ac}})$  were derived from

$$\sigma_{\rm ac} = \varepsilon_0 \omega \varepsilon''. \tag{2}$$

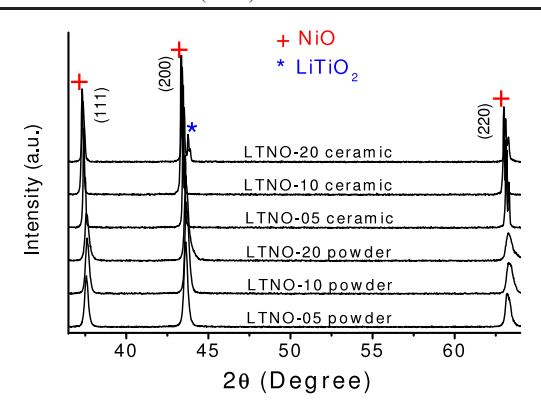


Figure 1. XRD patterns of LTNO powders and ceramics.

**Table 1.** Lattice parameter a and grain size of the LTNO ceramics.

Sample	Lattice parameter (Å)	Grain size (μm)
LTNO-05	4.165	6.29
LTNO-10	4.169	4.80
LTNO-20	4.164	6.99

# 3. Results and discussion

Figure 1 shows the XRD patterns of the LTNO powders and the sintered ceramics with different Li contents, confirming a possibility to produce the LTNO phase at a much lower reaction temperature compared to those prepared by the solgel route [4] and PC method [5]. All of the main peaks are comparable to those of the powder diffraction pattern of NiO in JCPDS card no. 78-0429 and those reported in the literature for cubic NiO [18, 21]. However, the second phase of LiTiO<sub>2</sub> is observed in the sintered LTNO-20 sample (JCPDS card no. 74-2257). The lattice parameters, determined from the diffraction patterns using Cohen's method, are summarized in table 1. These values are close to values reported in JCPDS card no. 78-0429 for cubic NiO with the lattice distortion of  $\sim$ 0.05– 0.3%. The SEM micrographs, shown in figure 2, reveal that the LTNO ceramics are dense and have obvious grain and grain boundary structure. The mean grain sizes are about  $6.29\pm2.11$ ,  $4.8 \pm 1.51$  and  $6.99 \pm 2.28 \ \mu m$  for LTNO-05, LTNO-10 and LTNO-20, respectively.

Figure 3(a) shows a typical SEM image of the fracture surface of the LTNO-05 sample; labeled with numerals 1–3 are the EDS measurement points. The EDS spectrum at point 2 is shown in figure 3(b), confirming the presence of Ti dopant in the microstructure of our LTNO-05 sample. The results of the EDS measurements at the grain and grain boundary regions, shown in figure 3(c), indicate that the Ti component can be found in both the grain and grain boundary layer. However, the concentration of Ti content at the grain boundary (point 2) was higher than that in the grain (points 1 and 3).

The temperature dependence of the real part of the complex permittivity ( $\varepsilon'$ ) and dissipation factor ( $\tan \delta = \varepsilon''/\varepsilon'$ ) of LTNO-05 is shown in figure 4(a) at selected frequencies between 0.5 and 500 kHz.  $\varepsilon'$  is nearly independent of temperature above a characteristic temperature, increasing

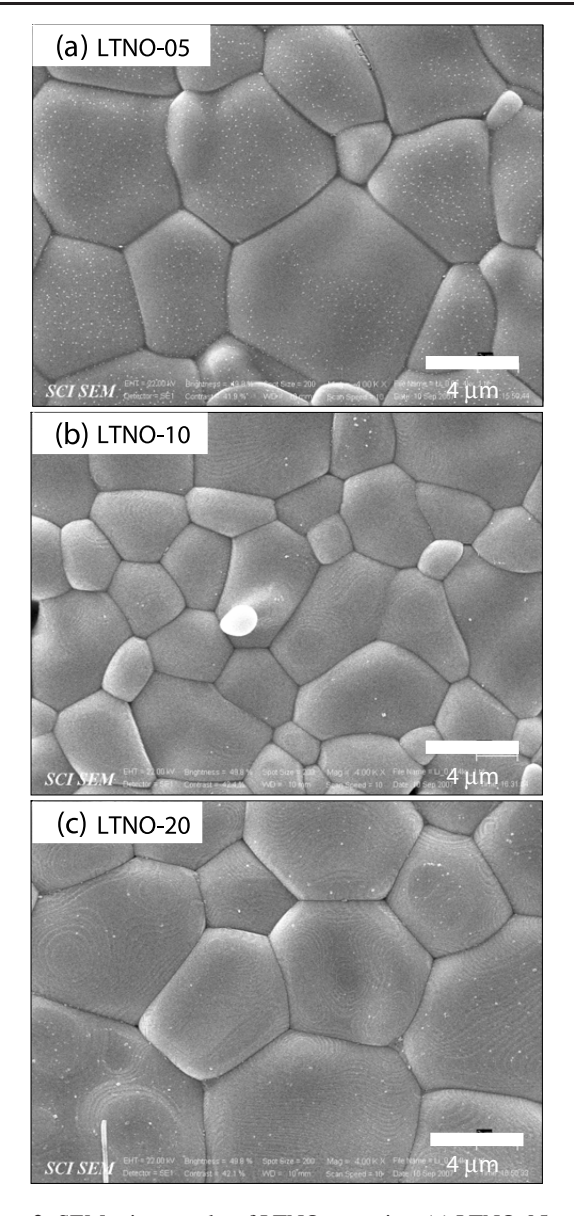


**Figure 2.** SEM micrographs of LTNO ceramics: (a) LTNO-05, (b) LTNO-10 and (c) LTNO-20.

with frequency increase. It attains a high value of  $\varepsilon' \sim 10^4$ , which is close to the value reported in [4] and much larger than that of pure NiO of  $\sim$ 30 (at 1 kHz). The high  $\varepsilon'$  for LTNO is not related to the intrinsic nature of ferroelectricity (a thermally driven phase transition) [4]. Below the characteristic temperature, a rapid decrease of  $\varepsilon'$  by about two orders of magnitude is observed, being accompanied by the appearance of corresponding relaxation peaks in the  $\tan \delta$ . The peak shifts to lower temperature as the frequency decreases. This confirms the thermally activated behavior which is typical for the Maxwell–Wagner relaxation. At high temperature and low frequency, the increase in  $\tan \delta$  may be attributed to the migration of excited electrical particles.

Figure 4(b) shows the temperature dependence of  $\varepsilon'$  and  $\tan \delta$  for LTNO-05, LTNO-10 and LTNO-20 at 1 kHz. The  $\varepsilon'$  values at room temperature for the LTNO-05, LTNO-10 and LTNO-20 samples are 9063, 74499 and 128236,

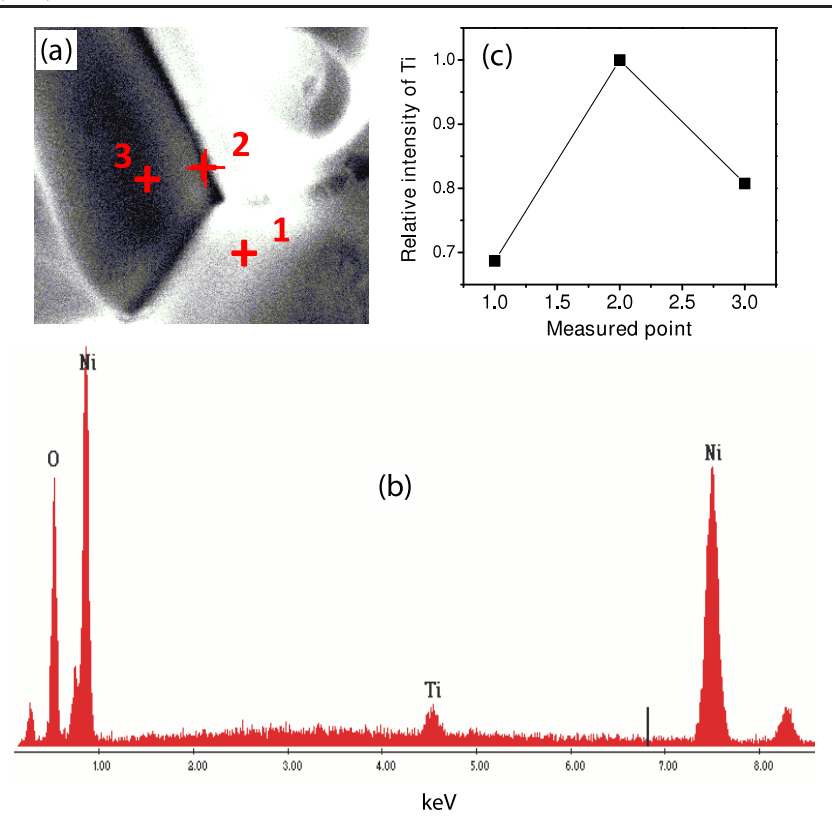
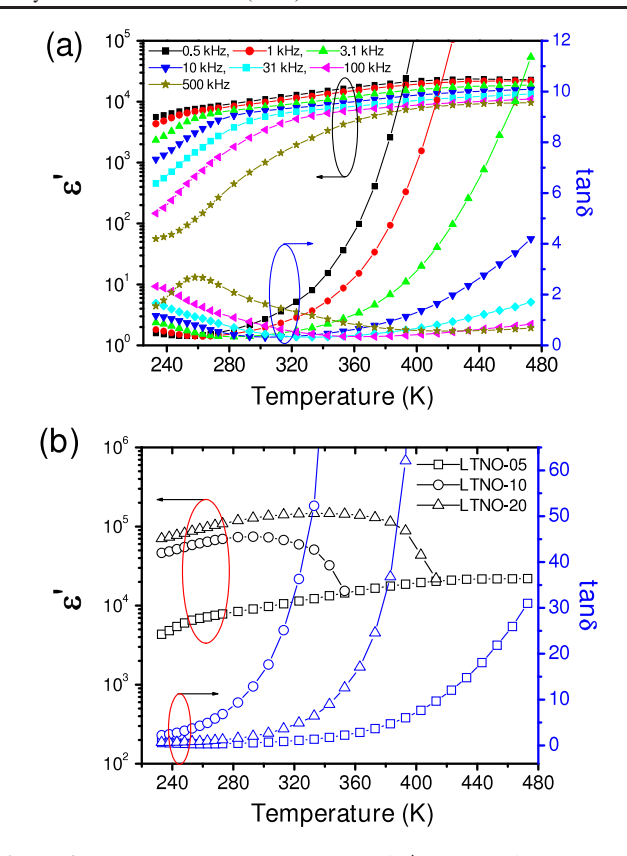


Figure 3. (a) SEM micrograph of the fractured surface of LTNO-05 sample, (b) EDS spectra at point 2 in (a) and (c) Ti element profile obtained from the EDS spectra.

respectively. The  $\varepsilon'$  value for the LTNO-20 sample is nearly 14 times larger than that for the LTNO-05 sample. It is well known that NiO is a Mott-Hubbard insulator at room temperature [22]. However, introduction of Ni<sup>2+</sup> vacancies  $(V_{Ni}'')$  and/or doping with monovalent cation impurities like Li<sup>+</sup> can dramatically increase the conductivity of NiO and thus NiO becomes semiconducting due to these defects [18]. Earlier works [4, 17] have shown that the Ti dopant is rich on the grain boundaries but indigent within the grains in (Li, Ti)doped NiO ceramics. Thus the interiors of the grains for LTNO are semiconducting (i.e. Li-doped NiO), while the shells of the grains are Ti-rich insulating boundaries (e.g. NiTiO<sub>3</sub>). The giant dielectric permittivity observed in our (Li, Ti)-doped NiO ceramics is therefore caused by its microstructure, because of the creation of an effective circuit of parallel capacitors, as found in boundary layer capacitors (BLC) [23]. According to the BLC structure and Maxwell-Wagner models, under an applied electric field the carrier conducting access is blocked by the Ti-rich boundary layer and thus the opposite charges will accumulate at the two edges of the insulator layer, creating a macroscopic electric dipole, which can be considered as a micro-parallel capacitor. As a result, the polarization formation primarily depends on the accumulation of charge via conduction in the grain interior. Therefore, an LTNO ceramic with higher Li concentration will possibly process more polarization and ascribe to the boundary layer capacitance effects. The highest dielectric permittivity seen in the LTNO-20 is therefore due to its higher Li concentration compared to those of the LTNO-10 and LTNO-05 samples. Note that, because the doping concentration of Ti is kept constant, the difference in dielectric behavior of LTNO samples can only be attributed to the effect of Li. As shown in figure 4(b), with the increase in temperature, the  $\varepsilon'$  values of LTNO-10 and LTNO-20 samples drop rapidly. This corresponds to the strong increases in their tan  $\delta$  values at the same temperature range. Such electrical responses of the LTNO-10 and LTNO-20 samples in the high temperature region may be attributed to the migration of excited electrical particles at high temperatures. However, the detailed description of the associated conduction behavior goes beyond the theme of this paper.

To understand the possible mechanism for high permittivity in LTNO-05, the real part  $(\varepsilon')$  and imaginary part  $(\varepsilon'')$ of the complex permittivity are plotted as a function of frequency over a temperature range of 233 and 313 K, as shown in figures 5(a) and (b). It is clear that  $\varepsilon'$  and  $\varepsilon''$  show a Debye-like relaxation, namely  $\varepsilon'$  displaying a step decrease at the frequency and the relaxation peak shifting to higher frequency with increasing temperature. At high temperature,  $\varepsilon'$ increases in the low frequency range (<1 kHz), and with increasing frequency up to  $10^4$ – $10^5$  Hz, a sharp decrease of  $\varepsilon'$ is observed. Normally, space charge (interfacial) polarization occurs when mobile charge carriers are impeded by a physical barrier (i.e. grain boundary) that inhibits charge migration. The charges then pile up at the barrier, producing a localized polarization within grains [24]. With increased temperature, the density of charges contributing to the space charge polarization is sufficiently large. The frequency range of sensitivity for such polarization may extend from  $10^{-3}$  Hz into the kilocycle range,



**Figure 4.** (a) Temperature dependences of  $\varepsilon'$  and  $\tan \delta$  for LTNO-05 at selected frequencies and (b) the temperature dependence of  $\varepsilon'$  and  $\tan \delta$  for LTNO-05, LTNO-10 and LTNO-20 at 1 kHz.

producing a very large  $\varepsilon'$  in this region. Therefore, the increase in  $\varepsilon'$  at low frequency is possibly due to space charge polarization. For the step-like decrease in  $\varepsilon'$  at the frequency range of 10<sup>3</sup>–10<sup>5</sup> Hz (corresponding to the respective relaxation peaks in  $\varepsilon''$ ) as shown in figure 5(b), dielectric relaxation in this region may be ascribed to the defect-dipole polarization effect, which appears at radio-frequency ranges. In general, there are two main effects responsible for the mechanism of polarization: the frequency of applied electric field and temperature. According to the effect of frequency, at fixed temperature, if an alternating field is applied then the polarization may fully develop at sufficiently low applied frequencies (the polarization and the field are in phase) but if the frequency of the applied field is too high then the field is reversed before the polarization has responded and no response will be the result of the net effect. The magnitude of the polarization thus drops off as the frequency is increased. For the effect of temperature [7], at low temperature, the electric dipoles freeze through the relaxation process, and there exists decay in polarization with respect to the applied electric field, which results in the sharp decrease in  $\varepsilon'$ . When the temperature is high, the rate of polarization formed is quick, and thus the relaxation occurs in high frequency as shown in figure 5(a).

In general, the frequency-dependent behavior of  $\varepsilon'$  and  $\varepsilon''$  of high dielectric permittivity can be well described by the simple Cole–Cole relaxation equation, which ignores the effect

of the electrical conduction [25, 26]:

$$\varepsilon^* = \varepsilon' - i\varepsilon'', \tag{3}$$

$$\varepsilon^* = \varepsilon_{\infty} + \frac{\varepsilon_s - \varepsilon_{\infty}}{1 + (j\omega\tau)^{1-\alpha}},\tag{4}$$

where  $\varepsilon_s$  and  $\varepsilon_\infty$  are respectively, the static and high frequency limits of dielectric permittivity,  $\tau$  is the most probable relaxation time and  $\alpha$  is the Cole–Cole parameter with values between 0 and 1. For an ideal Debye relaxation,  $\alpha=0$ . If  $\alpha>0$ , it implies that the relaxation has a distribution of relaxation times, leading to a broader peak shape than a Debye peak. However, when the electrical conductivity is dominated at the low frequency range as shown in figures 5(a) and (b), a contribution term by electrical conduction is generally added to the relaxation equation. The modified Cole–Cole equation that incorporates the conductivity term is given by [3, 27]

$$\varepsilon^* = \varepsilon_{\infty} + \frac{\varepsilon_{s} - \varepsilon_{\infty}}{1 + (j\omega\tau)^{1-\alpha}} - j\frac{\sigma^*}{\varepsilon_{0}\omega^{s}}$$
 (5)

where  $\sigma^*(\sigma^* = \sigma_1 + j\sigma_2)$  is the complex conductivity. Here  $\sigma_1$  is the conductivity due to the free charge carrier (dc conductivity) and  $\sigma_2$  is the conductivity due to the space charges (localized charges) and s is a dimensionless exponent (0 < s < 1). For an ideal complex conductivity, s = 1. If s < 1, it implies that the polarization has a distribution of the carrier polarization mechanism. From this relation, the complex permittivity can be decomposed into the real and imaginary parts. i.e.

$$\varepsilon' = \varepsilon_{\infty} + \frac{(\varepsilon_{s} - \varepsilon_{\infty}) \left\{ 1 + (\omega \tau)^{1 - \alpha} \sin(\alpha \pi / 2) \right\}}{1 + 2 (\omega \tau)^{1 - \alpha} \sin(\alpha \pi / 2) + (\omega \tau)^{2 - 2\alpha}} + \frac{\sigma_{2}}{\varepsilon_{0} \omega^{s}},$$
(6)

and

$$\varepsilon'' = \frac{(\varepsilon_s - \varepsilon_\infty) (\omega \tau)^{1 - \alpha} \cos (\alpha \pi / 2)}{1 + 2 (\omega \tau)^{1 - \alpha} \sin (\alpha \pi / 2) + (\omega \tau)^{2 - 2\alpha}} + \frac{\sigma_1}{\varepsilon_0 \omega^s}.$$
 (7)

It is clearly seen from equations (6) and (7) that the conductivity may have contributions to the dielectric permittivity ( $\varepsilon'$ ) and dielectric loss ( $\varepsilon''$ ). The first term of equation (7) is the part of the losses associated with the dielectric relaxation due to permanent dipole orientation or other motions which do not involve long-range displacement of mobile charge carriers, whereas the second term is the part of the losses associated with long-range migration of carrier response. From the above equations, the charge carrier localization at defect sites and interfaces ( $\sigma_2$ ) can make a large contribution to the dielectric permittivity, while the free charge carrier ( $\sigma_1$ ) contributes to the dielectric loss.

Analysis of the experimental data was carried out on the basis of equations (6) and (7). Typical fitting results are shown in figures 5(a) and (b): the solid lines are the fitted curves of experimental results. As clearly seen from figures 5(a) and (b), the excellent agreement between experimental data and calculated data over the entire range of frequencies and temperatures for both  $\varepsilon'$  and  $\varepsilon''$  is consistent with equations (6) and (7) for LTNO-05 ceramic. We notice a disagreement between the measured and calculated values for  $\varepsilon'$  at low

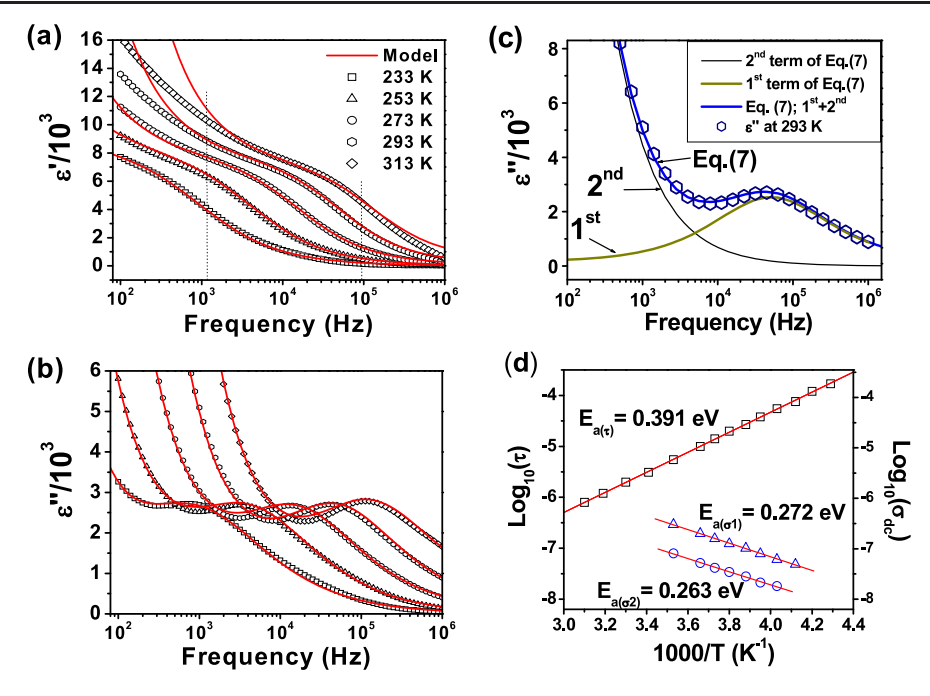


Figure 5. Frequency dependences of  $\varepsilon'$  (a) and  $\varepsilon''$  (b) of LTNO-05 at various temperatures. The solid curves are the best fits to equations (6) and (7) for  $\varepsilon'$  (a) and  $\varepsilon''$  (b), respectively, which include both a Cole–Cole relaxation and a complex conductivity contribution. (c). The evolution of the relaxation and dc conductivity contribute to the dielectric loss. (d) Arrhenius plots of the relaxation time and dc conductivities.

frequencies (<1 kHz) at temperature above 273 K. This may be due to the fact that some parts of the Ti dopant have entered into the NiO crystal lattice [17] and have an influence on the space charge localized inside the grain. Additionally, figure 5(c) shows the evolution of the relaxation and dc conductivity contributing on dielectric loss at 293 K. It is clearly seen that there are two main factors responsible for the dielectric relaxation of LTNO: dipole and conduction relaxation. A complete list of parameters used in the calculation ( $\Delta \varepsilon (\varepsilon_s \varepsilon_{\infty}$ ),  $\tau$ ,  $\alpha$ , s,  $\sigma_1$  and  $\sigma_2$ ) for LTNO-05 is shown in table 2. It is also important to mention that the s values tend to increase  $(s \rightarrow 1)$  with increasing temperature (does not present), indicating that the carrier polarization mechanism is weakly dispersive at higher temperature, which might be attributed to some barrier height extracted. For the value of  $\alpha$ , a relatively lower value of  $1 - \alpha$  corresponds to a more disordered system. Hence it can be inferred from the  $1 - \alpha$  values of LTNO-05 (0.66) and CCTO (0.91) [28] at 233 K that a relatively higher disorder is present in LTNO-05 compared to that of the CCTO system.

In order to elucidate the dielectric relaxation response in LTNO-05, it is important to estimate the activation energy of relaxations. Figure 5(d) shows the plot of  $\log \tau$  with 1/T, in which the solid line is the fitted result obeying the Arrhenius law:

$$\tau = \tau_0 \exp\left(\frac{E_{a(\tau)}}{k_B T}\right),\tag{8}$$

where  $\tau_0$  is the relaxation time at an infinite temperature,  $E_{a(\tau)}$  is the activation energy for the relaxation,  $k_B$  is the Boltzmann constant and T is the absolute temperature. As shown in table 2 and figure 5(d), the rapid decrease in  $\tau$  with increasing

**Table 2.** Fitted results of  $\Delta\varepsilon(\varepsilon_s - \varepsilon_\infty)$ ,  $\tau$ ,  $\alpha$ , s,  $\sigma_1$  and  $\sigma_2$  using the experimental results with equations (6) and (7) in a different temperature range for the LTNO-05.

T (K)	$\Delta \varepsilon = (\varepsilon_s - \varepsilon_\infty)$	α	S	τ (μs)	$\sigma_1$ (10 <sup>-4</sup> S m <sup>-1</sup> )	$\sigma_2$ (10 <sup>-4</sup> S m <sup>-1</sup> )
253 273	8700 8250 7800 7500	0.340 0.320 0.300 0.280	0.8	170 38 10 3.1		
313	7000	0.275	0.85	1.2	1.350	0.640

temperature is suggestive of an increased dipole density and faster polarization process [4]. According to the fitted curve for the LTNO-05 sample, the activation energy  $E_{\rm a(\tau)}$  value of the relaxation process is 0.391 eV and  $\tau_0=6.35\times 10^{-13}$  s. Additionally, the value of  $E_{\rm a(\tau)}$  is higher than that of 0.313 eV as reported by Wu *et al*, for Li<sub>0.05</sub>Ti<sub>0.02</sub>Ni<sub>0.93</sub>O [4]. It is important to note that, with increasing Li concentration, the relaxation peak moves out of the measured frequency range, which is similar to that reported by Wu *et al* [4]. Thus, the  $E_{\rm a(\tau)}$  values of the LTNO-10 and LTNO-20 samples could not be obtained.

As previously mentioned, the addition of  $\text{Li}_2\text{O}$  to NiO leads to an increase in conductivity, and some defects can be introduced due to different valences of doped ions. For every added  $\text{Li}^+$ , one Ni<sup>2+</sup> is promoted to the Ni<sup>3+</sup> state, which is the lost electron filling a state in the oxygen 2p valence band. The lattice now contains Ni<sup>2+</sup> and Ni<sup>3+</sup> ions on equivalent sites and is the model situation for conduction by polaron hopping [29]. In the polaronic scenario, the nearest-neighbor hopping obeys

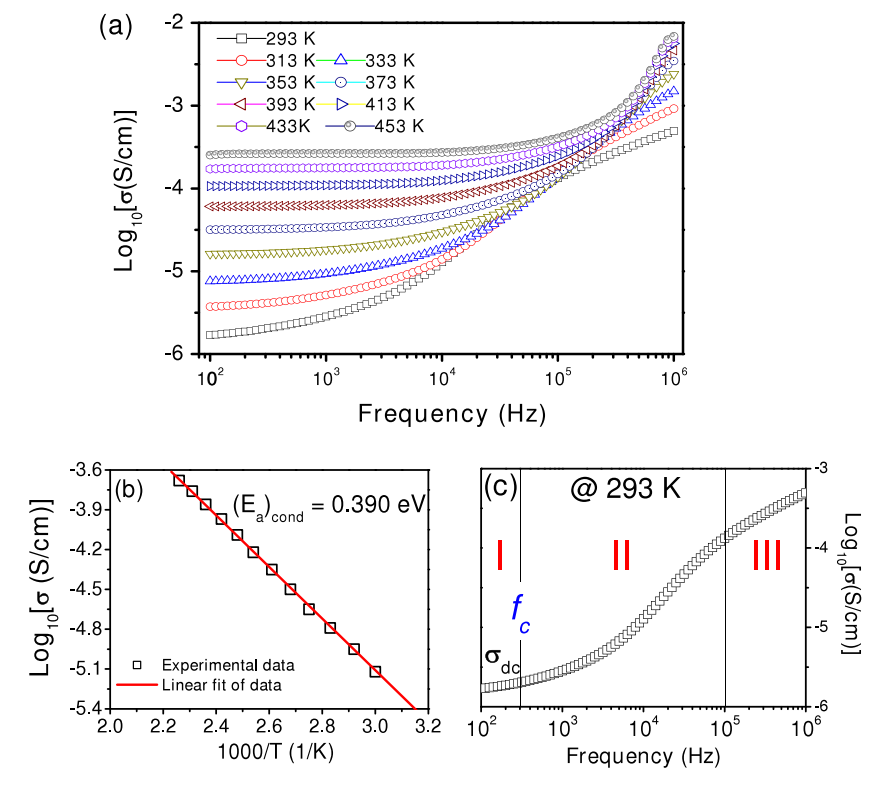


**Figure 6.** (a) Frequency dependence of ac conductivity at various temperatures. (b) Arrhenius plots of the temperature dependence of dc conductivity and (c) shows a typical conductivity spectrum of LTNO-05 ceramic at 293 K.

the Arrhenius-like law [30]

$$\sigma = \sigma_1' \exp\left(\frac{-E_{a(\sigma)}}{k_B T}\right),\tag{9}$$

where  $\sigma_1'$  is a constant and  $E_{a(\sigma)}$  is the conduction activation energy. As shown in figure 5(d), we found that the fitted  $\sigma_1$  and  $\sigma_2$  values at different temperatures follow the Arrhenius-like law, in which the solid line is the fitted result. Accordingly, in the LTNO-05 sample, both of the conduction activation energies for the localized charge and free charge carrier,  $E_{a(\sigma 2)} = 0.263$  eV and  $E_{a(\sigma 1)} = 0.272$  eV, were obtained, respectively. As previously reported [4, 17], the polarization relaxation has a close relation to the conductivity in the grain interior, because the value of  $E_{a(\sigma)}$  is almost the same as the value for  $E_{a(\tau)}$ . However, both values are different from our experimental results, indicating that the dielectric relaxation response in an LTNO-05 ceramic does not correspond to the conductivity in the grain interior.

In order to understand the effect of the conductivity on the dielectric properties of LTNO-05 ceramic, the frequency dependence of ac conductivity ( $\sigma_{ac}$ ) was further characterized over the temperature from 293 to 453 K. As shown in figure 6, the  $\sigma_{ac}$  shows a dispersion that shifts to higher frequency with increasing temperature, and it decreases with decreasing frequency, and then it nearly saturates to a constant value at low frequency. Extrapolating these curves at low frequencies gives the dc conductivity ( $\sigma_{dc}$ ). As illustrated in figure 6(c), the frequency dependence of ac conductivity at 293 K, a typical conductivity–frequency spectrum is divided into three

parts [31]. In region I, according to the jump relaxation model, since at low frequency and/or at high temperature the electric field cannot perturb the hopping conduction mechanism of charged particles, the conductance is approximately equal to the dc value and the conduction mechanism is the same as that for dc conduction as mentioned above, i.e. hopping of charged particles from one localized site to another. conductivity begins to increase nonlinearly after the frequency exceeds the critical frequency  $f_c$  in region II due to the fact that the capacitor admittance becomes numerically larger than the resistor admittance with increasing frequency. In region III, conductivity becomes proportional to frequency, resulting in nearly constant loss (NCL). In most materials, the NCL regime dominates the ac conductivity at high frequency or low temperature [32]. Here, we are interested in only region I (dc conducting region), but detailed descriptions of the associated conduction behavior in regions I and II go beyond the theme of this paper. As shown in figure 6(b), the resulting  $\sigma_{dc}$  follows an Arrhenius-like law in equation (9) with the estimated conduction activation energy of  $E_{a(cond)} = 0.390 \text{ eV}$ . From this result, it is seen that the activation energy required for the relaxation ( $E_{a(\tau)} = 0.391 \text{ eV}$ ) is almost the same value as the activation energy required for hopping of charged particles. However, it is premature to associate the polarization relaxation with the conductivity because the activation energies of the two processes were carried out at different temperature ranges.

In order to clarify the observed behavior as mentioned above, we used impedance spectroscopy (IS) analysis to study the electrical behavior of LTNO-05 ceramic. Conventionally,

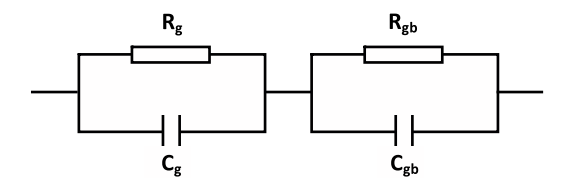


**Figure 7.** Equivalent circuit used to represent the electrical properties of a ceramic sample that exhibits grain  $(R_g, C_g)$  and grain boundary  $(R_{gb}, C_{gb})$  effects.

the bulk and grain boundary contributions to the overall impedance can be resolved by exploiting differences in their responses to an alternating applied field. Separation of the bulk and grain boundary of the material is obtained by fitting the experimental response to that of an equivalent circuit, which is usually considered to comprise a series of parallel resistor–capacitor (R–C) elements, as shown in figure 7. The circuit consists of a series array of two subcircuits, one represents grain effects and the other represents grain boundaries. Each subcircuit is composed of a resistor and capacitor joined in parallel. Let  $(R_g, R_{gb})$  and  $(C_g, C_{gb})$  be the resistances and capacitances of grains and grain boundaries, respectively, then the impedance  $Z^*$  for the equivalent circuit in this system is [15]

$$Z^* = \frac{1}{R_g^{-1} + j\omega C_g} + \frac{1}{R_{ob}^{-1} + j\omega C_{gb}} = Z' - jZ'', \quad (10)$$

where

$$Z' = \frac{R_{\rm g}}{1 + (\omega R_{\rm g} C_{\rm g})^2} + \frac{R_{\rm gb}}{1 + (\omega R_{\rm gb} C_{\rm gb})^2}$$
(11)

and

$$Z'' = R_{g} \left[ \frac{\omega R_{g} C_{g}}{1 + \left( \omega R_{g} C_{g} \right)^{2}} \right] + R_{gb} \left[ \frac{\omega R_{gb} C_{gb}}{1 + \left( \omega R_{gb} C_{g} b \right)^{2}} \right], \tag{12}$$

where Z' and Z'' are the real and imaginary parts of complex impedance. Figure 8(a) shows the frequency dependence of Z''at different temperatures. As shown in figure 8(b), at 233 K, a weak peak at about 500 kHz shifts to higher frequency with decreased intensity as the temperature increases, and it moves out of the frequency range of our experiment. However, with the temperature increased above 273 K, a strong peak appears in the measured frequency range as shown in figure 8(a), which also moves to higher frequencies with a fall in intensity as temperature increases. This implies that both electrical responses are thermally activated. Based on equation (12), the response peaks of the grains and grain boundaries are positioned at  $1/(2\pi R_g C_g)$  and  $1/(2\pi R_{gb} C_{gb})$ , respectively, and the peak values are proportional to associated resistances. In general, the peak frequency for grain boundaries is much lower than that for grains due to their large resistance and capacitance compared with those of grains [12].

Figure 8(c) shows the impedance spectra for the LTNO-05 ceramic at various temperatures. It can be seen that the impedance semicircles became smaller with increasing temperature, and two semicircles were observed and overlapped according to figure 8(d). The appearance of two semicircles strongly suggests that the core–shell model is appropriate for further characterization. Therefore, in the impedance spectra, we attribute the small semicircle at high frequency, which corresponds to the weak peaks in figure 8(b), to the grains, whereas we attribute the big semicircle at low frequency, which corresponds to the strong peaks in figure 8(a), to grain boundaries.

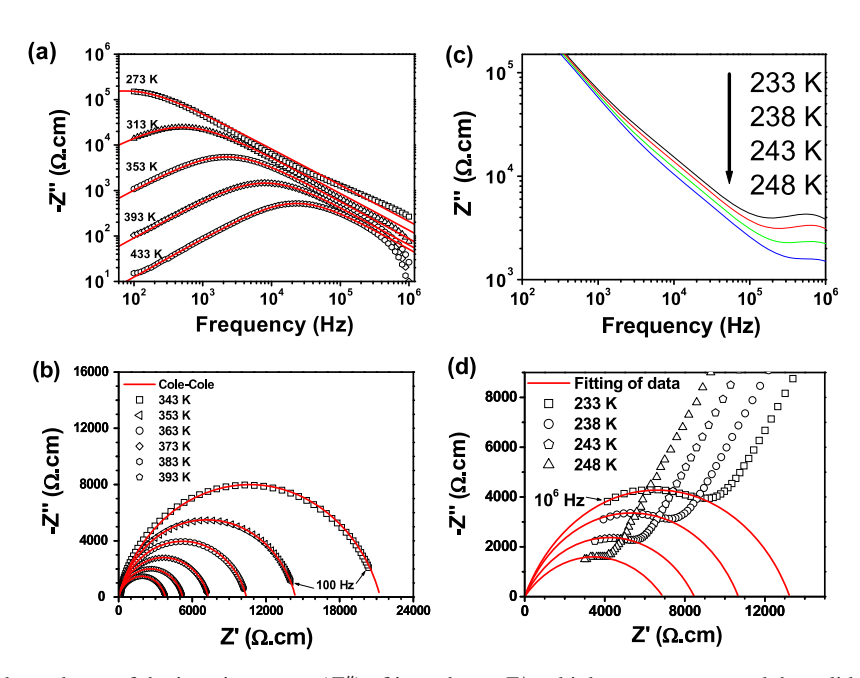


**Figure 8.** (a) Frequency dependence of the imaginary part (Z'') of impedance  $Z^*$  at high temperatures and the solid curves are the best fits to equation (14). (b) Frequency dependence of Z'' at low temperatures. (c) Impedance spectra as a function of temperature and the solid curves are the best fits to equation (14). (d) Impedance plane plot at low temperatures.

**Table 3.** Capacitances and conduction activation energies of grain and grain boundary of the LTNO samples.

	Capacitance (nF)		Resistar	Conduction activation energy (eV)		
Sample	C <sub>g</sub> (233 K)	C <sub>gb</sub> (303 K)	R <sub>g</sub> (233 K)	R <sub>gb</sub> (303 K)	$E_{ m g}$	$E_{ m gb}$
LTNO-05 LTNO-10 LTNO-20	_	5.0 17.0 60.0	1.32 × 10 <sup>4</sup> 99 44	$   \begin{array}{c}     1.01 \times 10^5 \\     0.25 \times 10^3 \\     1.16 \times 10^3   \end{array} $	_	0.369 0.302 0.307

As shown in figure 8(a), it is appropriate to fit the Z'' to a single  $R_{\rm gb}C_{\rm gb}$  parallel circuit due to the fact that the response peaks of the grains are too weak to be analyzed by equation (12), and it already moved out of the measured frequency range. Hence, equation (12) has been reduced to

$$Z^* = \frac{R_{\rm gb}}{1 + j\omega R_{\rm gb} C_{\rm gb}}.$$
 (13)

Unfortunately, equation (13) cannot be used to describe the experimental data very well. However, we found that the complex plane plot of  $Z^*$  is better described by using the Cole–Cole equation [25, 26], which is commonly used for polycrystalline ceramic samples [15]:

$$Z^* = \frac{R_{\rm gb}}{1 + \left(j\omega\tau_{\rm gb}\right)^{1-\alpha}},\tag{14}$$

where  $\tau_{\rm gb}=R_{\rm gb}C_{\rm gb}$  and the parameter  $\alpha$  is constant (0 <  $\alpha\leqslant 1$ ). By fitting the experimental data to equation (14), we obtained the values of  $R_{\rm gb}$ ,  $C_{\rm gb}$  and  $\alpha$  at different temperatures. The fitted values of  $\alpha$  at different temperatures are in the range of 0.21–0.14. The value of  $\alpha$  appears to decrease with increasing temperature.  $R_{\rm gb}$  decreases from  $1.5\times 10^6~\Omega$  at 253 K to  $1.1\times 10^3~\Omega$  at 443 K, whereas  $C_{\rm gb}=5~\rm nF$  is almost constant over the temperature range of 253 and 443 K. As shown in figure 8(d), the electrical response of the grain dominated at low temperatures, and the  $R_{\rm g}$  and  $C_{\rm g}$  values can simply be estimated by the relation that is similar to equation (14), i.e.  $Z^*=R_{\rm g}/[1+(j\omega R_{\rm g}C_{\rm g})^{1-\beta}]$ . The fitted values of  $R_{\rm g}$  and  $C_{\rm g}$  are tabulated in table 3.

Conductivity data,  $\sigma$ , where  $\sigma = R^{-1}$ , were obtained from the fitted  $R_{\rm g}$  and  $R_{\rm gb}$  values for the bulk  $(\sigma_{\rm g})$  and grain boundary ( $\sigma_{gb}$ ) components, and plotted against reciprocal temperature in Arrhenius format, in which the solid lines are the fitted results using equation (9). It is clearly seen from figure 9 that both are well fitted with the Arrheniuslike law. From the slopes of the fitted straight lines, we obtain an activation energy of about 0.369 eV for grain boundary and about 0.216 eV for grain, which indicate that the grain and grain boundary have different electrical transport characteristics. As previously reported, in the intermediate temperature range, heavy doping (5–10%) of Li in NiO induces a drop in activation energy from 0.9 eV to about 0.18 eV below 500 K [33]. It should be noted that the activation energy of the conductivity in the grain interiors for our LTNO-05 sample is about 0.216 eV, which is higher than 0.18 eV as

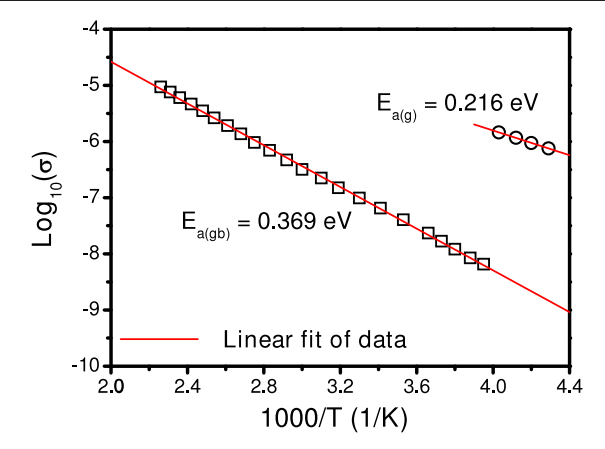


**Figure 9.** The Arrhenius plots of the conductivities of the grain and the grain boundary.

mentioned above. This is due to the fact that some part of Ti is incorporated into the crystal lattice of NiO and some defects are formed [17]. These results have an effect on the electric conductivity in the grains. Note that the value of grain conductivity activation energy in our LTNO sample is lower than that of the LTNO sample prepared by the sol-gel method,  $E_{a(g)} = 0.309$  eV, reported by Wu et al [4]. This may be attributed to the difference in the concentration of the part of the Ti dopant that has entered into the grain interiors due to the difference in the preparation method. In our case, such a part of the Ti dopant may have a low concentration inside the grain. This implies that the distribution of Ti dopant in the LTNO microstructure is the only factor that has an impact on the electrical properties of the bulk LTNO ceramics. It is of special interest to note that the activation energy of the conductivity in the grain interiors ( $E_{a(g)}$   $\sim$ 0.216 eV (figure 9)) is significantly lower than the activation energy required for relaxation ( $E_{a(\tau)} \sim 0.391 \text{ eV (figure 5(c))}$ ) as reported in the literature [7, 17]. In contrast, the value of activation energy for relaxation processes (~0.391 eV) is close to the activation energy of the conductivity in a grain boundary ( $\sim$ 0.369 eV). However, it is premature to associate the high relaxation activation energy of the LTNO-05 sample with its grain boundary conductivity activation energy because there are several factors that have a strong effect on the electrical properties of the LTNO ceramics, such as the defects (vacancies) and internal domain within the grain. This implies that high dielectric response in the LTNO ceramics is not only contributed by the dc conductivity in the grain interiors, but also by the defect dipoles.

It is widely accepted that the giant dielectric permittivity in LTNO is extrinsic in origin, which can be attributed to a Maxwell–Wagner relaxation mechanism in material, and often arises in a material consisting of conductive grains separated by insulating grain boundaries (or other insulating interfaces) [12, 14]. Based on the Maxwell–Wagner relaxation model, the measured ultrahigh dielectric permittivity and the relaxation process in the complex permittivity as a function of frequency can be easily understood. However, it is only a simplified model of interfacial polarization based on an equivalent circuit, and does not provide a physical explanation

for the underlying polarization. Lin *et al* [18] used positron annihilation spectroscopy to investigate defect properties in LTNO and revealed that a large amount of defects exists in the LTNO ceramics. Some defects can be introduced due to the different valence of doped ions. This may be represented by the reaction [18]

$$\operatorname{Li}_{2}\operatorname{O} \xrightarrow{\operatorname{NiO}} 2\operatorname{Li}'_{\operatorname{Ni}} + V_{\operatorname{O}}^{\bullet \bullet} + \operatorname{O}_{\circ}^{x} \tag{15}$$

$$\text{TiO}_2 \xrightarrow{\text{NiO}} \text{Ti}_{\text{Ni}}^{\bullet \bullet} + V_{\text{Ni}}'' + 2O_{\circ}^x.$$
 (16)

It is well known that NiO is p-dopable [34]. At room temperature, free-hole density is low in pure NiO, because the acceptor levels of the hole producer  $V_{\mathrm{Ni}}$  are not close enough to the valence band maximum to ionize most vacancies. In other words, the free-hole density of cation-deficient of NiO is limited by a too large an ionization energy of the Ni vacancy. However, it can be strongly increased by extrinsic dopants (e.g. Li) with shallower acceptor levels [33]. This implies that there is a high density of free holes in the grain interiors of LTNO ceramics. Meanwhile, TiO2 near the grain boundary also creates some Ni vacancies  $(V''_{Ni})$  as seen in equation (16) [17, 18]. Thus the LTNO system contains a large number of hopping charge carriers (and/or vacancies) and the grain boundary is highly disordered. As previously reported [19], the dielectric permittivity of Li<sub>0.10</sub>Ti<sub>x</sub>Ni<sub>0.90-x</sub>O thin films with 200 nm in thickness increases with increasing Ti content. This result strongly indicates that the Ti dopant in LTNO may not only act as an insulating layer, which obstructs the migration of charge carriers, but may also induce the permanent defect dipoles at the grain boundary. As illustrated in figure 5, the experimental results can be well described by the modified Cole-Cole equation, including the conductivity term. Therefore, the conductivity has contributions to the dielectric permittivity and dielectric loss at low frequency regions, and the dielectric relaxation peaks in higher frequency are associated with permanent dipole orientation or other motions, which do not involve long-range displacement of mobile charge carriers. In general, the grain boundary effect on electric conductivity may originate from a grain boundary potential barrier, which should be ascribed to the thin layer of Ti-rich boundary. As mentioned above, we think that the giant dielectric permittivity response of LTNO (or other dielectric material of co-doped NiO) can be partially contributed from Maxwell-Wagner space charge (long-range migration of carriers) effects at low frequency regions due to the difference of potentials barrier between grain (core) and grain boundary (shell). At high frequency, it is partially contributed from the polarization of highly permanent defect dipoles.

# 4. Conclusion

The high dielectric permittivity LTNO ceramics have been successfully synthesized by a simple PVA-sol-gel method. XRD results show the single phase of NiO. The temperature and frequency dependence of dielectric permittivity and dielectric loss were investigated. An excellent fit between

the experimental and simulated data has been obtained over a wide frequency and temperature using the modified Cole–Cole model with the consideration of the conductivity contribution. The high dielectric permittivity response can be ascribed to the Maxwell–Wagner polarization mechanism and defect-dipole polarization.

# Acknowledgments

The authors would like to thank the Department of Physics, Ubon Ratchathani University and the Faculty of Science Electron Microscopy Unit, Khon Kaen University for providing XRD and SEM facilities, respectively. PT and ST would like to thank the National Science and Technology Development Agency (NSTDA) for financial support of their studies through the TGIST and YSTP Programs, respectively. This work was financially supported by the Thailand Research Fund (TRF) and The Commission on Higher Education (CHE), The Ministry of Education, Thailand.

# References

- [1] Subramanian M A, Li D, Duan N, Reisner B A and Sleight A W 2000 J. Solid State Chem. 151 323
   Ramirez A P, Subramanian M A, Gardel M, Blumberg G, Li D, Vogt T and Shapiro S M 2000 Solid State Commun. 115 217
   Homes C C, Vogt T, Shapiro S M, Wakimoto S and Ramirez A P 2001 Science 293 673
- [2] Raevski I P, Prosandeev S A, Bogatin A S, Malitskaya M A and Jastrabik L 2003 J. Appl. Phys. 93 4130
- [3] Abdelkafi Z, Abdelmoula N, Khemakhem H, Bidault O and Maglione M 2006 J. Appl. Phys. 100 114111
- [4] Wu J, Nan C W, Lin Y and Deng Y 2002 Phys. Rev. Lett. 89 217601
- [5] Maensiri S, Thongbai P and Yamwong T 2007 Acta Mater. 55 2851
- [6] Lin Y, Wang J, Jiang L, Chen Y and Nan C W 2004 Appl. Phys. Lett. 85 5664
- [7] Lin Y, Jiang L, Zhao R and Nan C W 2005 Phys. Rev. B 72 014103
- [8] Jana P K, Sarkar S and Chaudhuri B K 2006 Appl. Phys. Lett. 88 182901
- [9] Jana P K, Sarkar S, Sakata H, Watanabe T and Chaudhuri B K 2008 J. Phys. D: Appl. Phys. 41 065403
- [10] Hsiao Y J, Change Y S, Fang T H, Chai T L, Chung C Y and Chang Y H 2007 J. Phys. D: Appl. Phys. 40 863
- [11] Meansiri S, Thongbai P and Yamwong T 2007 Appl. Phys. Lett. 90 202908
- [12] Sinclair D C, Adams T B, Morrison F D and West A R 2002 Appl. Phys. Lett. 80 2153
- [13] Cohen M H, Neaton J B, He L and Vanderbilt D 2003 J. Appl.
- Phys. 94 3299[14] Lunkenheimer P, Fichtl R, Ebbinghaus S G and Loidl A 2004
- *Phys. Rev.* B **70** 172102 [15] Liu J, Duan C, Mei W N, Smith R W and Hardy J R 2005
- J. Appl. Phys. 98 093703
   [16] Chung S Y, Kim I L D and Kang S J L 2004 Nat. Mater. 3 774
- [17] Lin Y H, Li M, Nan C W, Li J, Wu J and He J 2006 Appl. Phys. Lett. **89** 032907
- [18] Lin Y, Zhao R, Wang J, Cai J, Nan C W, Wang Y and Wei L 2005 J. Am. Ceram. Soc. 88 1808
- [19] Zhang Y R, Zhang B P, Dong Y and Li J F 2007 Key Eng. Mater. 336–338 2639
- [20] Yamamoto S, Kakihana M and Kato S 2000 J. Alloys Compounds 297 81

- [21] Wu J B, Nan J, Nan C W, Lin Y, Deng Y and Zhao S 2003 Mater. Sci. Eng. B 99 294
- [22] Terkura K, Williams A R and Oguchi T 1984 *Phys. Rev. Lett.* **52** 1830
- [23] Nan C W 1993 *Prog. Mater. Sci.* 37 1Waser R and Hagenbeck R 2000 *Acta Mater.* 48 797
- [24] Hence L L and West J K 1990 *Principles of Electronic Ceramics* (New York: Wiley)
- [25] Cole K S and Cole R H 1941 J. Chem. Phys. 9 342
- [26] Macdonald J R 2005 Impedance Spectroscopy (New York: Wiley)
- [27] Ming D, Reau J M, Ravez J, Gitae J and Hagenmuller P 1995 J. Solid State Chem. 116 185
- [28] Thongbai P, Masingboon1 C, Maensiri S, Yamwong T, Wongsaenmai S and Yimnirun R 2007 J. Phys.: Condens. Matter 19 236208
- [29] Moulson A J and Herbert J M 2003 *Electroceramics* (New York: Wiley)
- [30] Zhang L and Tang Z J 2004 Phys. Rev. B 70 174306
- [31] Li W and Schwartz R W 2006 Appl. Phys. Lett. 89 242906
- [32] Leon C, Rivera A, Varez A, Sanz J, Santamaria J and Ngai K L 2001 *Phys. Rev. Lett.* **86** 1279
- [33] van Houten S 1960 J. Phys. Chem. Solids 17 7
- [34] Lany S, Guillen J O and Zunger A 2007 *Phys. Rev.* B **75** 241203



Contents lists available at ScienceDirect

# Materials Chemistry and Physics

journal homepage: www.elsevier.com/locate/matchemphys



# Effects of Li and Fe doping on dielectric relaxation behavior in (Li, Fe)-doped NiO ceramics

Prasit Thongbai<sup>a</sup>, Teerapon Yamwong<sup>b</sup>, Santi Maensiri<sup>a,\*</sup>

- <sup>a</sup> Department of Physics, Faculty of Science, Khon Kaen University, Khon Kaen 40002, Thailand
- <sup>b</sup> National Metals and Materials Technology Center (MTEC), Thailand Science Park, Pathumthani 12120, Thailand

#### ARTICLE INFO

Article history: Received 26 May 2009 Received in revised form 25 November 2009 Accepted 28 March 2010

PACS: 77.22.Ch 77.22.Gm 77.84.Dv

Keywords: Ceramics Chemical synthesis Electron microscopy Dielectric properties Electrical properties

# ABSTRACT

High permittivity (Li, Fe)-doped NiO (LFNO) ceramics are prepared by a simple PVA sol–gel route and their dielectric properties are investigated as functions of temperature and frequency. It is found that the concentrations of Li and Fe have strong influences on the microstructure and dielectric properties of the LFNO ceramics. Two thermally activated dielectric relaxations are observed in the  $\rm Li_{0.05}Fe_{0.10}Ni_{0.85}O$  ceramic sample with the activation energies of 0.448 and 0.574 eV for the high- and low-frequency relaxations, respectively. By using a complex impedance analysis, it is believed that the high-frequency relaxation is closely related to the transport properties inside the grains, and the low-frequency relaxation might be ascribed to the interfacial polarization at the interface layers of grain boundaries and/or NiFe $_2O_4$  secondary phase layers.

© 2010 Elsevier B.V. All rights reserved.

# 1. Introduction

High permittivity NiO-based ceramic, a non-perovskite and non-ferroelectric material with a formula  $\mathbf{A}_{x}\mathbf{B}_{y}\mathrm{Ni}_{1-x-y}\mathrm{O}$  (where  $\mathbf{A}$ are monovalents of Li<sup>+</sup>, Na<sup>+</sup>, K<sup>+</sup> and **B** are Ti, Al, Ta, Si, V, W) [1–12], has recently attracted considerable attentions due to its impressive apparent high dielectric permittivity ( $\varepsilon'$ ) value ( $10^3$ – $10^5$ ), which remains constant in the temperature range of -50 to 150 °C at low frequency range. The dielectric and related electrical properties of these material systems are usually modified by changing the compositions of the additives of  $\boldsymbol{A}$  and  $\boldsymbol{B}$  [1,3-6,10,11]. A core/shell structure was found to exist in these NiO-based ceramic systems [4,8-13], which induced an electrically heterogeneous microstructure, consisting of semiconducting grains (Li-doped NiO) and insulating grain boundaries (GBs) (Ti-rich boundary). As a result, the Maxwell-Wagner (MW) polarization (interfacial polarization) mechanism has been used to explain the giant  $\varepsilon'$  response in this material system. The MW polarization usually introduces in materials that have electrically heterogeneous structure consisting of conducting and insulating parts, which are often observed in the grains and GBs, respectively [4,8–13]. Most recently, we found that both the sintering temperature and grain size have remarkable influences on the electrical properties of the NiO-based ceramics [8,14]. These indicate that the electrical transport properties within the materials also strongly depend on defects such as oxygen vacancies and/or internal insulating domains inside the grains. According to two our previous works, we prepared the LTNO powders and ceramics by using polymerized complex (PC) (Ref. [2]) and polyvinyl alcohol (PVA) (Ref. [15]) methods. The PC method can be used to synthesize  $\sim\!39$  nm nanoparticles of Li $_{0.3}$ Ti $_{0.02}$ Ni $_{0.68}$ O. However, this prepared LTNO powders contained some second phase. In the other hand, the PVA method can be used to synthesize the LTNO powders without any impurity phases.

In this paper, we studied the dielectric properties of polycrystalline (Li, Fe)-doped NiO (LFNO) ceramics. Our results indicate that both Li and Fe doping have strong influences on the microstructure and electrical properties of the LFNO ceramics. The dielectric polarization relaxations in this material system might be associated with both the electrical transport (hopping motion) inside the semiconducting grains and the space charge polarization.

# 2. Experimental details

 $Ni(NO_3)_2 \cdot 6H_2O$ , LiNO<sub>3</sub>, Fe(NO<sub>3</sub>)<sub>3</sub>·9H<sub>2</sub>O, citric acid, and polyvinyl alcohol (PVA) ( $M_n$  = 78,000, Fluka) were employed as starting raw materials. The

<sup>\*</sup> Corresponding author. Tel.: +66 43 202222; fax: +66 43 202374.

E-mail addresses: sanmae@kku.ac.th, santimaensiri@gmail.com (S. Maensiri).

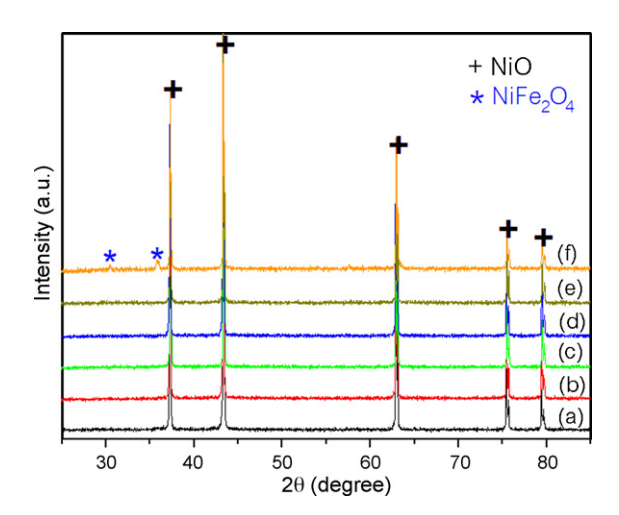


**Fig. 1.** XRD patterns of LFNO ceramics with different Li and Fe contents; (a)  $Fe_{0.02}Ni_{0.98}O$ , (b)  $Li_{0.02}Fe_{0.02}Ni_{0.96}O$ , (c)  $Li_{0.05}Fe_{0.02}Ni_{0.93}O$ , (d)  $Li_{0.10}Fe_{0.02}Ni_{0.88}O$ , (e)  $Li_{0.05}Fe_{0.05}Ni_{0.90}O$ , and (f)  $Li_{0.05}Fe_{0.10}Ni_{0.85}O$ .

polycrystalline LFNO ceramic samples with different addition contents of Li and Fe, i.e., Fe<sub>0.02</sub>Ni<sub>0.98</sub>O, Li<sub>0.02</sub>Fe<sub>0.02</sub>Ni<sub>0.96</sub>O, Li<sub>0.05</sub>Fe<sub>0.02</sub>Ni<sub>0.93</sub>O, Li<sub>0.10</sub>Fe<sub>0.02</sub>Ni<sub>0.88</sub>O, Li<sub>0.05</sub>Fe<sub>0.02</sub>Ni<sub>0.99</sub>O, and Li<sub>0.05</sub>Fe<sub>0.02</sub>Ni<sub>0.88</sub>O, were prepared by the following procedure. Firstly, citric acid 5 g was dissolved in 95 ml of distilled water in with constant stirring using a magnetic stirrer at room temperature, and then PVA 5 g was added to this solution by stirring at 200 °C to obtain the polymer solution network. Secondly, stoichiometric amounts of Ni(NO<sub>3</sub>)<sub>2</sub>-6H<sub>2</sub>O, Fe(NO<sub>3</sub>)<sub>3</sub>-9H<sub>2</sub>O, and LiNO<sub>3</sub> were added to this solution, followed by stirring and heating at 100 °C to form the transparent gel. Then, the gel precursor was dried at 120 °C overnight. To obtain the LFNO powders, the dried gel was ground and later calcined at 750 °C for 10 h in air. The obtained powders were pressed into pellets of 16 mm in diameter and ~1–2 mm in thickness by a uniaxial pressing method at 200 MPa. Finally, these pellets were sintered at 1250 °C for 5 h in air.

The phase composition and microstructure of the LFNO ceramics were characterized by X-ray diffraction (XRD) (Philips PW3040, The Netherlands) and Field-emission scanning electron microscopy (FE-SEM) (Hitachi S-4700, Japan), respectively. The ceramic samples were polished and electroded by silver paint on both sides of the disk-shape samples. They were allowed to dry overnight. The dielectric response of the samples was measured using a Hewlett Packard 4194A impedance gain phase analyzer over the frequency ranges from  $10^2-10^7$  Hz and at the oscillation voltage of 1.0 V. The measurements were performed over the temperature ranges from -50 to  $100\,^{\circ}$ C using an inbuilt cooling–heating system. Each measured temperature was kept constant with an accuracy of  $\pm 1$  K.

# 3. Results and discussion

Fig. 1 shows the XRD patterns of the LFNO ceramics with different addition contents of Li and Fe ions, confirming a main phase of NiO in all samples. All of the main peaks are comparable to that of the powder diffraction pattern of NiO in JCPDS card no. 78-0429 and those reported in the literature for cubic NiO [14-16]. The second phase of NiFe<sub>2</sub>O<sub>4</sub> (JCPDS card no. 74-2081) is only detected in the XRD pattern of the  $Li_{0.05}Fe_{0.10}Ni_{0.85}O$  sample with highest Fe concentration. Since the difference in ionic radius between  $Ni^{2+}$  (0.69 Å),  $Fe^{2+}$  (0.74 Å), and  $Fe^{3+}$  (0.64 Å) ions is small, Fe ions can substitute the Ni<sup>2+</sup> ions in the NiO crystal lattice [17]. The observed NiFe<sub>2</sub>O<sub>4</sub> should be attributed to the Fe-dopant content which is over the solid solution limitation of Fe-Ni-O system. The lattice parameters are calculated from the XRD patterns of the LFNO ceramic samples and are summarized in Table 1. These values are close to the value reported in JCPDS card no. 78-0429 (4.177 Å) for cubic NiO.

Fig. 2 reveals the surface morphologies of the LFNO ceramics, showing obvious grain and GB structure. The microstructural evolution is observed. The SEM image of the  $Fe_{0.02}Ni_{0.98}O$  sample, Fig. 2(a), shows hillock-like morphology and large portion of porosity. However, after the  $Fe_{0.02}Ni_{0.98}O$  sample was increasingly added by Li ions, the ceramic density tended to increase with increasing

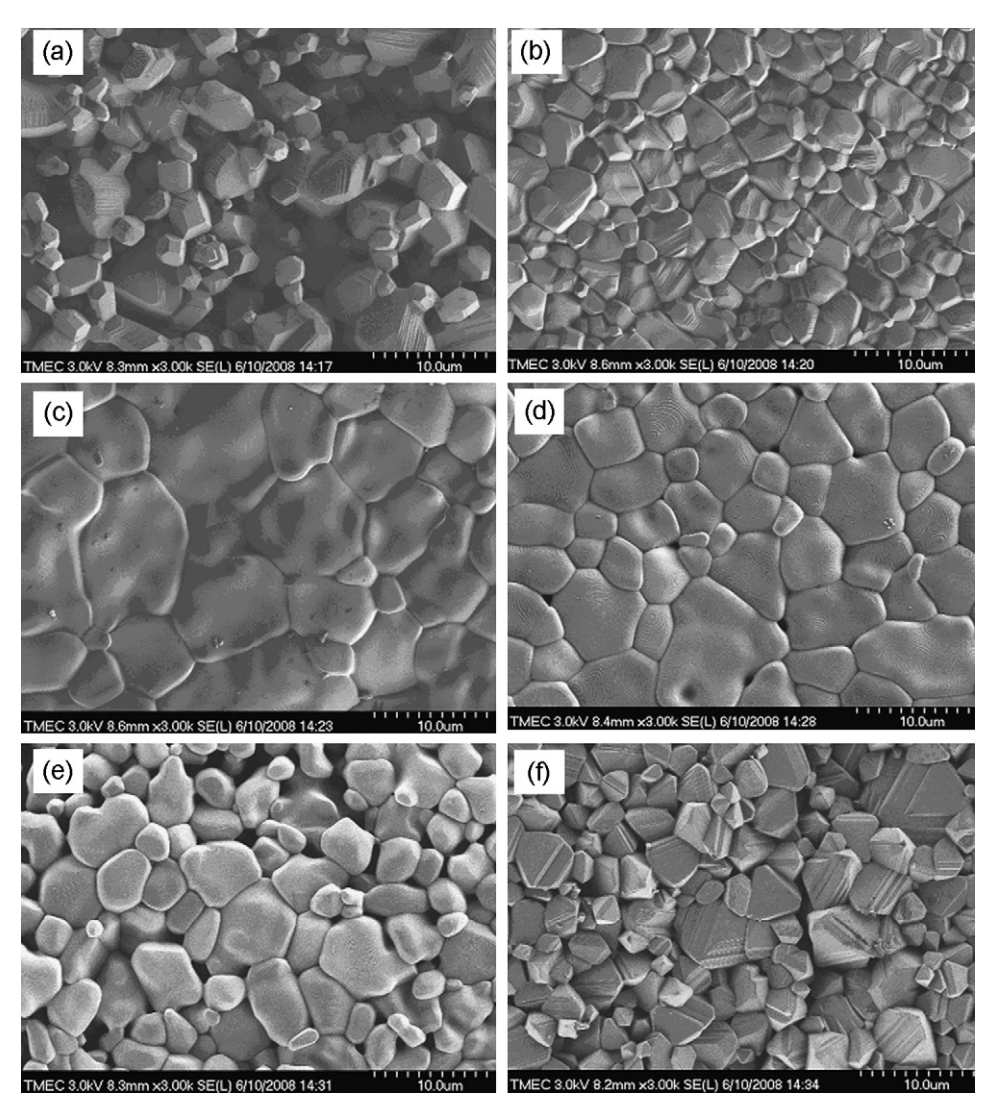
**Table 1**Lattice parameter, relaxation activation energy, and conduction activation energy inside the grain.

Sample	a (Å)	E <sub>a</sub> (eV)	E <sub>g</sub> (eV)
Fe <sub>0.02</sub> Ni <sub>0.98</sub> O	4.176	0.855	0.643
Li <sub>0.02</sub> Fe <sub>0.02</sub> Ni <sub>0.96</sub> O	4.176	0.425	0.418
Li <sub>0.05</sub> Fe <sub>0.02</sub> Ni <sub>0.93</sub> O	4.172	-	-
Li <sub>0.10</sub> Fe <sub>0.02</sub> Ni <sub>0.88</sub> O	4.177	-	-
Li <sub>0.05</sub> Fe <sub>0.05</sub> Ni <sub>0.90</sub> O	4.173	0.353	0.357
Li <sub>0.05</sub> Fe <sub>0.10</sub> Ni <sub>0.85</sub> O	4.172	(HFR) 0.448	0.455

Li content and the hillock-like morphology became disappeared and it was completely disappeared after the Li concentration was increased up to 5 mol%, as shown in Fig. 2(c). Interestingly, this special morphology appeared in the Li–Fe–Ni–O system again, when the Fe concentration was increased up to 10 mol%, as seen in Fig. 2(f). These results indicate that both the Li– and Fe-dopants affect the microstructure, i.e., grain size and feature, of the LFNO ceramics. The possible explanation for this mechanism might be ascribed based on the difference in the diffusivity of the carriers (i.e., Ni<sup>2+</sup>, Li<sup>+</sup>, and Fe<sup>3+</sup> ions) in the LFNO ceramics, which is related linearly to their electrical conductivity [6].

Fig. 3 illustrates the influence of Li doping on the dielectric properties of the LFNO ceramics at room temperature. It is clear that the high dielectric response in the LFNO ceramics depends on the Li concentration. Both the real part  $\varepsilon'$  of complex permittivity and loss tangent  $\tan \delta$  ( $\tan \delta = \varepsilon'' / \varepsilon'$ , where  $\varepsilon''$  is the imaginary part of the complex permittivity) of the LFNO samples increase with an increase in the Li content over the measured frequency range. These results are similar to that observed in the (Li, Ti)doped NiO (LTNO) ceramics system [1]. A plateau can be observed in all the dielectric spectra, as displayed in Fig. 3(a). However, the steplike decrease in  $\varepsilon'$  is only detected in the dielectric spectrum of the Li<sub>0.02</sub>Fe<sub>0.02</sub>Ni<sub>0.96</sub>O sample. This is accompanied by the appearance of the corresponding peak tan  $\delta$  in Fig. 3(b). The disappearance of the steplike decrease in the Li<sub>0.05</sub>Fe<sub>0.02</sub>Ni<sub>0.93</sub>O and Li<sub>0.10</sub>Fe<sub>0.02</sub>Ni<sub>0.88</sub>O samples is due to the fact that it shifts out of our measuring frequency range. The effect of Fe doping on the dielectric behavior of the LFNO ceramics has also been investigated, as illustrated in Fig. 4. Clearly, the concentration of Fe affects on both the value of  $\varepsilon'$  and dielectric relaxation behavior of the LFNO ceramics. With increasing the Fe concentration,  $\varepsilon'$  decreases and the steplike decrease at the characteristic frequency shifts to lower frequencies. Looking carefully at Fig. 4(a), the dielectric spectrum of the Li<sub>0.05</sub>Fe<sub>0.10</sub>Ni<sub>0.85</sub>O sample with highest Fe concentration exhibits two steplike decreases, corresponding to the two respective peaks in tan  $\delta$ . This suggests that there exist two sets of thermally activated relaxations, i.e., low- and high-frequency relaxations (abbreviated as LFR and HFR, respectively). It is worth noting that the exponential increase in tan  $\delta$ , which is usually attributed to the dc conductivity effect [15], decreases with the increase in the Fe concentration, and disappears in the Li<sub>0.05</sub>Ti<sub>0.10</sub>Ni<sub>0.85</sub>O sample.

It has been reported that pure NiO is a Mott–Hubbard insulator with the conductivity at room temperature less than  $10^{-13}$  S cm<sup>-1</sup> [1]. However, this low conductivity can greatly be increased by doping with monovalent ions such as Li<sup>+</sup> [18]. For every added Li<sup>+</sup>, one Ni<sup>2+</sup> is promoted to the Ni<sup>3+</sup> state, which is the lost electron filling a state in the oxygen 2p valence band. The lattice now contains Ni<sup>2+</sup> and Ni<sup>3+</sup> ions on equivalent sites and is the model situation for conduction by polaron hopping [18]. Therefore, the carrier concentration in the bulk LFNO ceramics raises with increasing the Li concentration, and thus the accumulated charges at insulating layers (e.g., grain boundary, contact, impurity phase, and internal domain) in the bulk ceramics should increase. This may be responsible for the observed increase in  $\varepsilon'$  with increasing the content of Li ions, as shown in Fig. 3(a). Moreover, it has been proposed that



 $\textbf{Fig. 2.} \hspace{0.5cm} \textbf{EM} \hspace{0.5cm} \textbf{images} \hspace{0.5cm} \textbf{of} \hspace{0.5cm} \textbf{the} \hspace{0.5cm} \textbf{sumples} \hspace{0.5cm} \textbf{of} \hspace{0.5cm} \textbf{(a)} \hspace{0.5cm} \textbf{Fe}_{0.02} \textbf{Ni}_{0.98} \textbf{O}, \textbf{(b)} \hspace{0.5cm} \textbf{Li}_{0.05} \textbf{Fe}_{0.02} \textbf{Ni}_{0.96} \textbf{O}, \textbf{(c)} \hspace{0.5cm} \textbf{Li}_{0.05} \textbf{Fe}_{0.02} \textbf{Ni}_{0.98} \textbf{O}, \textbf{(e)} \hspace{0.5cm} \textbf{Li}_{0.05} \textbf{Fe}_{0.05} \textbf{Ni}_{0.90} \textbf{O}, \textbf{(a)} \hspace{0.5cm} \textbf{Li}_{0.05} \textbf{Fe}_{0.02} \textbf{Ni}_{0.88} \textbf{O}, \textbf{(e)} \hspace{0.5cm} \textbf{Li}_{0.05} \textbf{Fe}_{0.05} \textbf{Ni}_{0.90} \textbf{O}, \textbf{(a)} \hspace{0.5cm} \textbf{Li}_{0.05} \textbf{Fe}_{0.02} \textbf{Ni}_{0.88} \textbf{O}, \textbf{(b)} \hspace{0.5cm} \textbf{Li}_{0.05} \textbf{Fe}_{0.05} \textbf{Ni}_{0.90} \textbf{O}, \textbf{(c)} \hspace{0.5cm} \textbf{Li}_{0.05} \textbf{Fe}_{0.02} \textbf{Ni}_{0.88} \textbf{O}, \textbf{(c)} \hspace{0.5cm} \textbf{Li}_{0.05} \textbf{Fe}_{0.05} \textbf{Ni}_{0.90} \textbf{O}, \textbf{(c)} \hspace{0.5cm} \textbf{Li}_{0.05} \textbf{Fe}_{0.02} \textbf{Ni}_{0.88} \textbf{O}, \textbf{(c)} \hspace{0.5cm} \textbf{Li}_{0.05} \textbf{Fe}_{0.05} \textbf{Ni}_{0.90} \textbf{O}, \textbf{(c)} \hspace{0.5cm} \textbf{Li}_{0.05} \textbf{Fe}_{0.02} \textbf{Ni}_{0.88} \textbf{O}, \textbf{(c)} \hspace{0.5cm} \textbf{Li}_{0.05} \textbf{Fe}_{0.05} \textbf{Ni}_{0.90} \textbf{O}, \textbf{(c)} \hspace{0.5cm} \textbf{Li}_{0.05} \textbf{Ni}_{0.90} \textbf{O}, \textbf{(c)} \hspace{0.5cm} \textbf{Ni}_{0.90} \textbf{O}, \textbf{(c)} \hspace{0.5cm} \textbf{N$ 

dipolar effects in semiconducting materials can be induced by the hopping of localized charge carriers between spatially fluctuating lattice potentials [19], which usually causes an increase in electrical conductivity. Therefore, it is possible that the dipolar effects in the semiconducting grains of the LFNO ceramics are induced, and it should be increased by increasing the Li doping ions.

It was reported that the high dielectric response in the LTNO ceramics system could be ascribed by a simple series-layer model

 $(\varepsilon' \sim \varepsilon_{\rm gb} A/t, \ \, {\rm where} \,\,\, \varepsilon_{\rm gb}, \,\, A, \,\, {\rm and} \,\,\, t \,\,\, {\rm are} \,\,\, {\rm the} \,\, {\rm dielectric} \,\, {\rm permittivity} \,\, {\rm of} \,\, {\rm the} \,\, {\rm grain} \,\, {\rm boundary}, \,\, {\rm the} \,\, {\rm mean} \,\, {\rm grain} \,\, {\rm size}, \,\, {\rm and} \,\, {\rm the} \,\, {\rm thickness} \,\, {\rm of} \,\, {\rm grain} \,\, {\rm boundary}, \,\, {\rm respectively}). \,\, {\rm The} \,\,\, {\rm decrease} \,\, {\rm in} \,\,\, \varepsilon' \,\,\, {\rm of} \,\,\, {\rm the} \,\,\, {\rm LTNO} \,\,\, {\rm ceramics} \,\,\, {\rm was} \,\, {\rm attributed} \,\, {\rm to} \,\, {\rm the} \,\, {\rm increase} \,\, {\rm in} \,\, t, \, {\rm resulting} \,\, {\rm from} \,\, {\rm the} \,\, {\rm Ti-rich} \,\, {\rm boundaries} \,\, ({\rm second} \,\, {\rm phase} \,\, {\rm of} \,\, {\rm NiTiO_3}) \,\, [1]. \,\, {\rm According} \,\, {\rm to} \,\, {\rm this} \,\, {\rm model}, \, {\rm for} \,\, {\rm the} \,\, {\rm NiO-based} \,\, {\rm ceramics}, \, t \, {\rm should} \,\, {\rm be} \,\, {\rm tuned} \,\, {\rm and} \,\, {\rm depended} \,\, {\rm linearly} \,\, {\rm on} \,\, {\rm the} \,\, {\rm concentration} \,\, {\rm of} \,\, {\rm the} \,\, {\rm apparent} \,\, {\rm second} \,\, {\rm phase} \,\, {\rm at} \,\, {\rm the} \,\, {\rm grain} \,\, {\rm boundary}. \,\, {\rm However}, \,\, {\rm for} \,\, {\rm our} \,\, {\rm LFNO} \,\, {\rm ceramics}, \, {\rm the} \,\, {\rm second} \,\, {\rm phase} \,\, {\rm of} \,\, {\rm NiFe_2O_4} \,\, {\rm can} \,\, {\rm our} \,\, {\rm LFNO} \,\, {\rm ceramics}, \, {\rm the} \,\, {\rm second} \,\, {\rm phase} \,\, {\rm of} \,\, {\rm NiFe_2O_4} \,\, {\rm can} \,\, {\rm our} \,\, {\rm LFNO} \,\, {\rm ceramics}, \, {\rm the} \,\, {\rm second} \,\, {\rm phase} \,\, {\rm our} \,\, {\rm NiFe_2O_4} \,\, {\rm can} \,\, {\rm our} \,\, {\rm ceramics}, \, {\rm the} \,\, {\rm second} \,\, {\rm phase} \,\, {\rm our} \,\, {\rm NiFe_2O_4} \,\, {\rm can} \,\, {\rm our} \,\, {\rm our} \,\, {\rm ceramics}, \, {\rm the} \,\, {\rm ceramics}, \, {\rm ceramics}, \, {\rm the} \,\, {\rm ceramics}, \, {\rm the} \,\, {\rm ceramics}, \, {\rm ceramics}, \, {\rm ceramic$ 

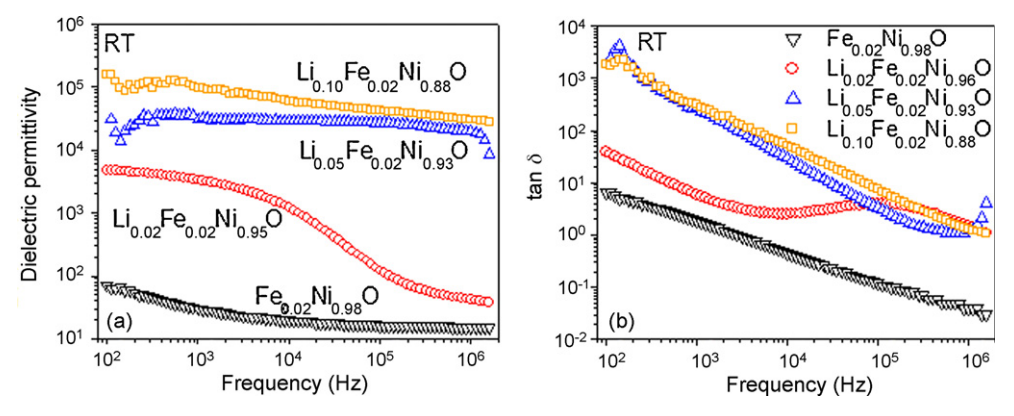


**Fig. 3.** The effect of Li concentration on frequency dependence of the (a)  $\varepsilon'$  and (b)  $\tan \delta$  for the LFNO ceramics at room temperature.

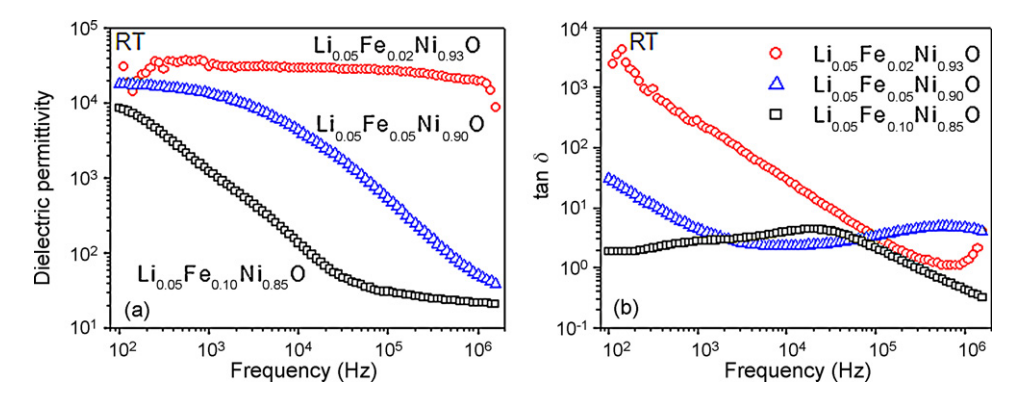


**Fig. 4.** The effect of Fe concentration on the frequency dependence of the (a)  $\varepsilon'$  and (b)  $\tan \delta$  of the LFNO ceramics at room temperature.

only be detected in the XRD pattern of the  $\text{Li}_{0.05}\text{Fe}_{0.10}\text{Ni}_{0.85}\text{O}$  sample. There, it is not suitable to deduce that the observed decrease in  $\varepsilon'$  is attributed to the increase in t, resulting from the increase in NiFe $_2\text{O}_4$  concentration in the NiO matrix. Consequently, this model fails to ascribe the effect of Fe concentration on dielectric properties of the LFNO ceramics.

To deepen the understanding on the high dielectric response mechanism in the LFNO ceramics, we have further studied the dielectric relaxation behavior, which usually provides important clues about the dielectric response mechanisms. Therefore, the frequency dependences of  $\varepsilon'$  and  $\tan \delta$  were investigated at various temperatures. As seen in Fig. 5, the steplike decreases and the corresponding  $\tan \delta$  peaks of the LFNO samples move to higher frequencies as the temperature increases, indicating the thermally excited relaxation process. This behavior is similar to those observed in the other NiO-based ceramic systems such as (Li, Ti)-, (Li, Si)-, (Na, Ti)-, (Li, V)-, and (Li, Al)-doped NiO systems [1,4,6,9,10]. Note that, the movements of the LFR and HFR in Li<sub>0.05</sub>Fe<sub>0.10</sub>Ni<sub>0.85</sub>O sample are clearly seen in Fig. 5(d). According to the observed thermally activated relaxations in the LFNO ceramics, the activation energies required for these relaxations can be calculated by using the Arrhenius law, i.e.:

$$\tau = \tau_0 \exp\left(\frac{E_a}{k_B T}\right),\tag{1}$$

where  $\tau$  is the dielectric relaxation time,  $\tau_0$  is the pre-exponential factor,  $E_a$  is the activation energy for the relaxation,  $k_B$  is the Boltzmann constant, and T is the absolute temperature. By using the extreme value relation [20]:

$$\omega \tau = \sqrt{\frac{\varepsilon_{\rm S}}{\varepsilon_{\infty}}},\tag{2}$$

where  $\varepsilon_S$  and  $\varepsilon_\infty$  are respectively the static and high frequency limits of dielectric permittivity, and  $\omega = 2\pi f_p$ , where  $f_p$  is the characteristic frequency corresponding to the peak of  $\tan \delta$ . Equation (1) can be expressed as:

$$\ln(2\pi f_{\rm p}) = \frac{-E_{\rm a}}{k_{\rm B}T} + \ln\left(\frac{\sqrt{\varepsilon_{\rm S}/\varepsilon_{\infty}}}{\tau_{\rm 0}}\right) \tag{3}$$

According to the fitted curves in Fig. 6, the activation energy ( $E_a$ ) for the relaxation processes can be calculated by using the relation in equation (3), and are summarized in Table 1. Note that the characteristic peaks of the LFR, Fig. 5(d), cannot be estimated accurately from the experimental data. Thus, two Gaussian peaks were used to fit the experimental data of  $\tan \delta$ , as shown in the inset of Fig. 5(d). The  $E_a$  values of the  $\text{Li}_{0.05}\text{Fe}_{0.02}\text{Ni}_{0.93}\text{O}$  and  $\text{Li}_{0.10}\text{Fe}_{0.02}\text{Ni}_{0.88}\text{O}$  samples cannot be obtained because their relaxation peaks shift out of the measured frequency range, as clearly seen in Fig. 3. It is inter-

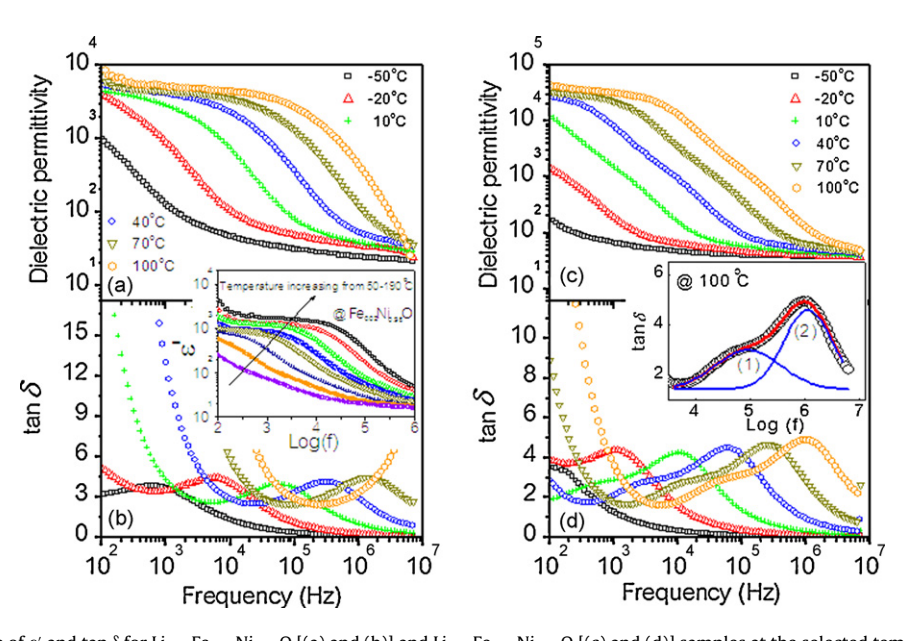


**Fig. 5.** Frequency dependence of  $\varepsilon'$  and  $\tan \delta$  for Li<sub>0.02</sub>Fe<sub>0.02</sub>Ni<sub>0.96</sub>O [(a) and (b)] and Li<sub>0.05</sub>Fe<sub>0.10</sub>Ni<sub>0.85</sub>O [(c) and (d)] samples at the selected temperatures. The inset of (a) and (b) shows frequency dependence of  $\varepsilon'$  of Fe<sub>0.02</sub>Ni<sub>0.98</sub>O sample at temperature range of 50–190 °C. The inset of (c) and (d) shows two Gaussian peaks (blue lines) which are least-squares fitting of experimental data at 100 °C; the red line is fitting result; (1) and (2) are the LFR and HFR, respectively.

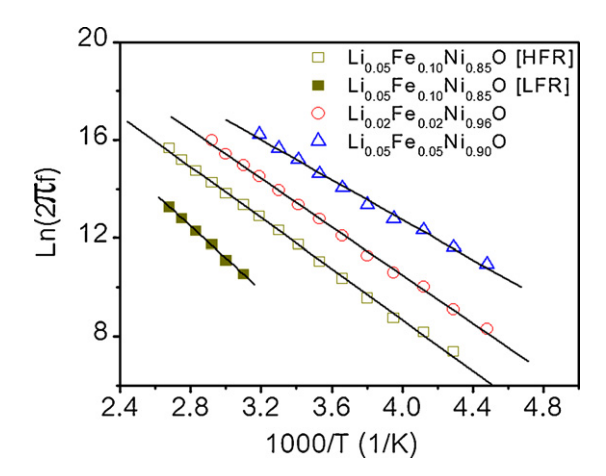
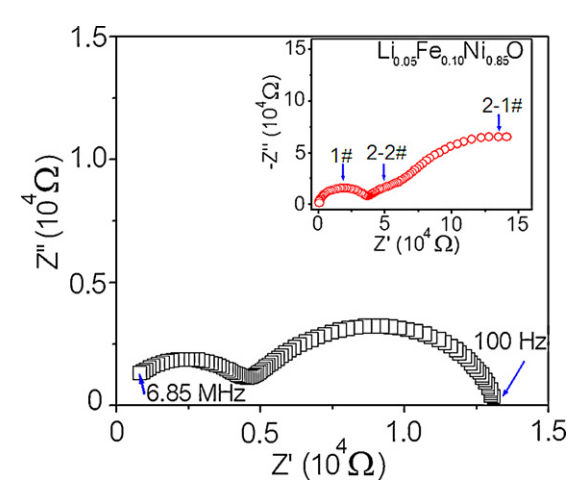


Fig. 6. Arrhenius plots of the relaxations of the LFNO ceramics.

esting that, with increasing the Fe concentration from 5 to 10 mol%,  $E_a$  increases from 0.353 to 0.448 eV for the HFR. This implies that the Fe-dopant has an influence on the polarization relaxation properties of the LFNO ceramics. It is worth noting that, the dielectric relaxation behavior of the Fe  $_{0.02}\rm Ni_{0.98}\rm O$  sample can also be observed at high temperature range, i.e., 50-200 °C, as shown in the inset of Fig. 5(a), with  $E_a \sim 0.855$  eV. This value is almost the same to the value of 0.850 eV for the dc conduction as reported in the literature for Fe-doped NiO polycrystalline ceramics [21]. The ptype semiconductivity of these ceramics was proved by using the Seebeck coefficient measurements technique, indicating that holes were major carriers in this material [21]. As a result, the dielectric response in our  $Fe_{0.02}Ni_{0.98}O$  sample should be related to the hopping motions of these holes, which might be ascribed based on the fact that the polarization relaxation in NiO-based ceramics has a close relation to their conductivity inside the grains [13,14].

It is now generally accepted that the giant  $\varepsilon'$  response in NiO-based ceramics is associated with their core/shell microstructures, which produce an electrically inhomogeneous structure confirming by the complex impedance and microstructure analyses [4,8,9–14].



**Fig. 7.** Impedance spectrum of  $Li_{0.02}Fe_{0.02}Ni_{0.96}O$  sample at room temperature; inset shows the impedance spectrum of  $Li_{0.05}Fe_{0.10}Ni_{0.85}O$  sample at room temperature.

The large difference in the conductivity between the semiconducting grains and insulating GBs of these materials (more than one order of magnitude) is often detected [13–16]. Therefore, it is suitable to associate such apparent giant  $\varepsilon'$  response with the MW polarization at GBs. However, the observed two electrical responses in the Li<sub>0.02</sub>Fe<sub>0.02</sub>Ni<sub>0.96</sub>O sample show a small difference in the conductivities, as displayed in Fig. 7. This indicates that the explanation of the giant  $\varepsilon'$  response in the LFNO ceramics based on the MW polarization at the GBs may still incomplete. Moreover, a careful inspection reveals that the enhanced arc in the low-frequency range may contain two overlapping arcs. These overlapping arcs are clearly seen in the impedance spectrum of the Li<sub>0.05</sub>Fe<sub>0.10</sub>Ni<sub>0.85</sub>O sample (the inset of Fig. 7), and the separated small hump (2-2# region) can be observed. The three sets of electrical responses in the LFNO ceramics are the suitable ascriptions for the dielectric relaxation behavior.

To obtain more details about the effects of Fe doping on dielectric behavior of the LFNO ceramics, impedance analysis (IS), which is a powerful technique to separate various electrical responses

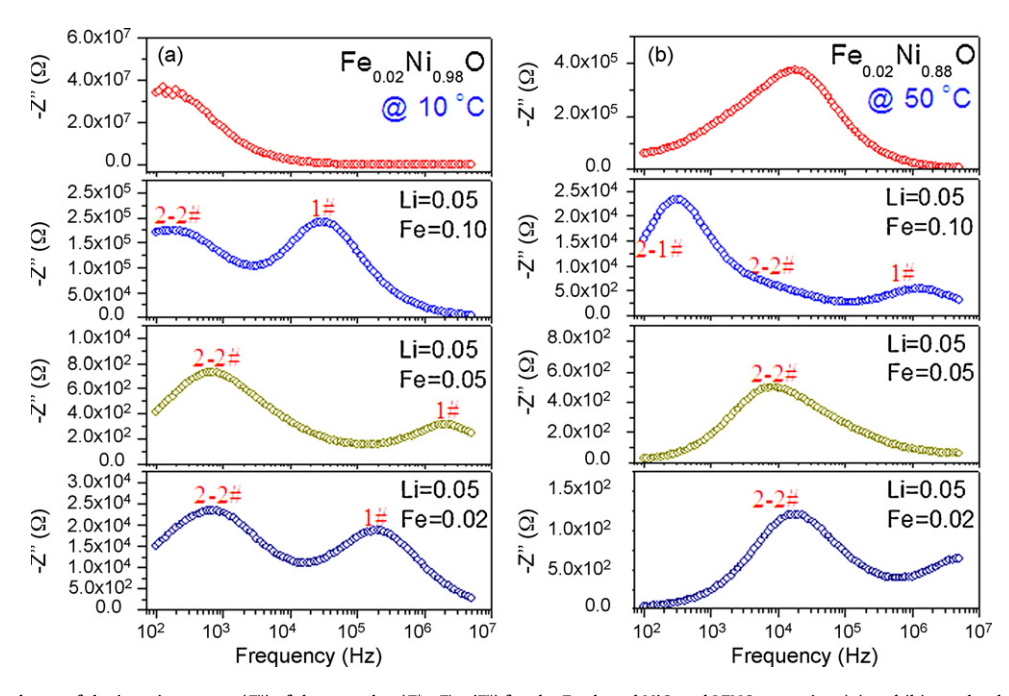


Fig. 8. Frequency dependence of the imaginary part (Z'') of the complex  $(Z^* = Z' - jZ'')$  for the Fe-doped NiO and LFNO ceramics; (a) and (b) are the data at temperatures of 10 and 50 °C, respectively.

in materials [22], was used to investigate the electrical responses in the LFNO ceramics. The frequency dependence of the imaginary part (Z'') of the complex impedance  $(Z^* = Z' - jZ'')$  for the Fe<sub>0.02</sub>Ni<sub>0.98</sub>O and LFNO ceramics is illustrated in Fig. 8. As shown in Fig. 8(a), IS data at temperature of 10 °C, two electrical responses (1# and 2-2#) can be observed in the Z" spectra of the LFNO ceramics, but just only one can be observed in the spectrum of the Fe<sub>0.02</sub>Ni<sub>0.98</sub>O ceramic. These results imply that there are at least two electrical responses in the LFNO ceramics. With increasing the temperature up to 50 °C, Fig. 8(b), the 1# and 2-2# electrical responses shift to high frequencies. The 1# electrical response of the Li<sub>0.05</sub>Fe<sub>0.05</sub>Ni<sub>0.90</sub>O sample shifts out of the measured frequency range. It is interesting that three electrical responses (1#, 2-2#, and 2-1#) can be observed in the measured frequency range of the Li<sub>0.05</sub>Fe<sub>0.10</sub>Ni<sub>0.85</sub>O sample, corresponding to the observed three semicircle arcs in the complex impedance plot, inset of Fig. 7. Clearly, there is only one electrical response in the impedance spectrum of the Fe<sub>0.02</sub>Ni<sub>0.98</sub>O sample. Of cause, this electrical response of the FNO sample is related to the effect of Fe doping. Defect dipoles  $(2Fe_{Ni}^{\bullet}$  and  $V_{Ni}^{\prime\prime})$  as well as  $[2Fe_{Ni}^{\bullet}V_{Ni}^{\prime\prime}]$  complex defects may be introduced, which are responsible for the observed electrical response in the FNO sample. More interesting, the 2-2# electrical response of these three LFNO samples is nearly in the same frequency range of the electrical response of the Fe<sub>0.02</sub>Ni<sub>0.98</sub>O sample. As results, the observed 2-2# electrical response of the LFNO samples may be related to the defect dipole and/or complex defects. Unfortunately, the distribution of the Fe doping within the structural matrix of NiO was not analyzed. Thus, the 2-2# electrical response of the LFNO samples cannot be suggested to the effect of grain boundary. However, it is related to the induced defects owing to the Fe doping, thus the 2-2# electrical response can be assigned to "Feinduced defects effect". As shown in Fig. 8(b), the observed 2-1# electrical response in the Li<sub>0.05</sub>Fe<sub>0.10</sub>Ni<sub>0.85</sub>O sample may be associated with the detected NiFe<sub>2</sub>O<sub>4</sub> phase in its XRD pattern. Therefore, the 2-1# electrical response is assigned to "insulating NiFe<sub>2</sub>O<sub>4</sub> phase effect". From these points of view, the 1#, 2-2#, and 2-1# electrical responses of the LFNO samples can be assigned as the bulk, Feinduced defects, and insulating NiFe<sub>2</sub>O<sub>4</sub> phase effects, respectively.

We now turn to attend the observed two dielectric responses in the  $\text{Li}_{0.05}\text{Fe}_{0.10}\text{Ni}_{0.85}\text{O}$  sample. According to the impedance analysis, the resistance of grains can be estimated at various temperatures, but not for the GBs which is due to the fact that the impedance spectra of electrodes and GBs are overlap and they cannot be separated accurately. However, the conduction activation energy inside the grain  $(E_g)$  of each sample can be calculated by using the polaron theory [4,13], i.e.,  $\sigma \propto T^{-1} \exp(-E/k_BT)$ , where *E* is the conduction activation energy. The calculated values of the grain conduction activation energy are summarized in Table 1. The grain conduction activation energies  $(E_g)$  are almost the same to the  $E_a$  values for the  $Li_{0.02}Fe_{0.02}Ni_{0.96}O$  and  $Li_{0.05}Fe_{0.05}Ni_{0.90}O$  samples. These strongly indicate a close relationship between the polarization relaxation and the conductivity inside the grains, which is similar to those observed in the other NiO-based ceramic systems [10–14]. Hence, it is reasonable to mention that the HFR (with  $E_a \sim 0.448 \, \text{eV}$ ) of the Li<sub>0.05</sub>Fe<sub>0.10</sub>Ni<sub>0.85</sub>O sample is related to the electrical response of the bulk grains (with  $E_{\rm g} \sim 0.455\,{\rm eV}$ ), while the LFR (with  $E_{\rm a} \sim 0.574\,{\rm eV}$ ) should be associated with the electrical response at the GBs. The disappearance of the dielectric relaxation related to the electrode effect in the lowest frequency range might be due to two possible reasons: (1) It is concealed by the high loss tangent associated with the dc conductivity at high temperature, as revealed in the dielectric loss spectrum at 100 °C in Fig. 5(d). (2) With decreasing temperature, the electrode relaxation peak may appear because charge carriers are frozen, but it moves out of the measured frequency range.

It is important to note that the increases in  $E_g$  and related  $E_a$ with the increase of the addition of Fe might be related to the point defects in the grains, which could be introduced into NiO by doping Fe ions [17], i.e.:

$$Fe_2O_3 \xrightarrow{NiO} 2Fe_{Ni}^{\bullet} + V_{Ni}'' + 3O_0 \tag{4}$$

$$Fe_{Ni}^{\bullet} \leftrightarrow Fe_{Ni}^{\times} + h$$
 (5)

Accordingly, we think that the observed decrease in  $\varepsilon'$  might be due to the effect of these defects, rather than the increase in the thickness of GBs based on the simple layer model. As previously discussed, it has been suggested that the HFR is associated with the conduction mechanism inside the grains. Therefore, the difference in the dielectric relaxation of the LFNO ceramics, as demonstrated in Fig. 4, should be attributed to the increase in  $E_{\rm g}$ , i.e., the dielectric relaxation in a ceramic with high  $E_a$  is hardly activated by thermal due to its high  $E_{\rm g}$ . Consequently, at a given temperature, the relaxation time of this ceramic should has the longest time, and then its relaxation behavior occurs at the lowest frequency.

#### 4. Conclusions

The frequency and temperature dependences of  $\varepsilon'$  and  $\tan \delta$  of the (Li, Fe)-doped NiO (LFNO) ceramics were studied. The variation of the Li and Fe concentrations had effects on the microstructure and electrical properties of these LFNO ceramics. It was suggested that the dielectric relaxation behavior and high dielectric response in this material system might be associated with both the hopping motions inside the grains and the MW polarization at the GBs.

# Acknowledgements

The authors would like to thank the Thai Microelectronics Center (TMEC) for FE-SEM facilities. P.T. would like to thank the TGIST for his Ph.D. scholarship. This work was financially supported by the Thailand Research Fund (TRF) and The Commission on Higher Education (CHE), Thailand.

# References

- J. Wu, C.W. Nan, Y.H. Lin, Y. Deng, Phys. Rev. Lett. 89 (2000) 217601.
- [2] S. Maensiri, P. Thongbai, T. Yamwong, Acta Mater. 55 (2007) 2851.
  [3] Y.H. Lin, J. Wang, L. Jiang, Y. Chen, C.W. Nan, Appl. Phys. Lett. 85 (2004) 5664.
  [4] Y.H. Lin, L. Jiang, R. Zhao, C.W. Nan, Phys. Rev. B 72 (2005) 014103.
- [5] P.K. Jana, S. Sarkar, B.K. Chaudhuri, Appl. Phys. Lett. 88 (2006) 182901.
- [6] P.K. Jana, S. Sarkar, H. Sakata, T. Watanabe, B.K. Chaudhuri, J. Phys D: Appl. Phys. 41 (2008) 065403.
- Y.J. Hsiao, Y.S. Change, T.H. Fang, T.L. Chai, C.Y. Chung, Y.H. Chang, J. Phys D: Appl. Phys. 40 (2007) 863.
- [8] P. Thongbai, Y. Yamwong, S. Maensiri, Appl. Phys. Lett. 94 (2009) 022908.
- [9] G.J. Chen, Y.J. Hsiao, Y.S. Chang, T.L. Chai, J. Alloys Compd. 474 (2009) 237-240.
- [10] S. Tangwancharoen, P. Thongbai, T. Yamwong, S. Maensiri, Mater. Chem. Phys. 115 (2009) 585-589.
- S. Pongha, P. Thongbai, T. Yamwong, S. Maensiri, Scripta Mater. 60 (2009) 870-873
- [12] B. Cheng, Y.H. Lin, A. Mei, J.N. Cai, C.W. Nan, J. He, Appl. Phys. Lett. 92 (2008) 142903.
- Y.H. Lin, M. Li, C.W. Nan, J. Li, J. Wu, J. He, Appl. Phys. Lett. 89 (2006) 032907.
- P. Thongbai, T. Yamwong, S. Maensiri, J. Appl. Phys. 104 (2008) 074109.
- P. Thongbai, S. Tangwancharoen, T. Yamwong, S. Maensiri, J. Phys.: Condens. Mater, 20 (2008) 395227.
- [16] J.B. Wu, J. Nan, C.W. Nan, Y.H. Lin, Y. Deng, S. Zhao, Mater. Sci. Eng. B B99 (2003) . 294–297.
- [17] J. Wang, J. Cai, Y.H. Lin, C.W. Nan, Appl. Phys. Lett. 87 (2005) 202501.
- A.J. Moulson, J.M. Herbert, Electroceramics, Wiley, New York, 2003.
- [19] A.K. Jonscher, Dielectric Relaxation in Solids, Chelsea, London, 1983.
- W. Li, K. Chen, Y. Yao, J. Zhu, Y. Wang, Appl. Phys. Lett. 85 (2004) 4717.
- Y.H. Lin, J. Wang, J. Cai, M. Ying, R. Zhao, M. Li, C.W. Nan, Phys. Rev. B 73 (2006)
- [22] D.C. Sinclair, A.R. West, J. Appl. Phys. 66 (1989) 3850.

ELSEVIER

Contents lists available at ScienceDirect

# Materials Chemistry and Physics

journal homepage: www.elsevier.com/locate/matchemphys



# Dielectric and electrical properties of giant dielectric (Li, Al)-doped NiO ceramics

Suwat Tangwancharoen<sup>a</sup>, Prasit Thongbai<sup>a</sup>, Teerapon Yamwong<sup>b</sup>, Santi Maensiri<sup>a,\*</sup>

- <sup>a</sup> Department of Physics, Faculty of Science, Khon Kaen University, Khon Kaen, 40002, Thailand
- <sup>b</sup> National Metals and Materials Technology Center (MTEC), Thailand Science Park, Pathumthani, 12120, Thailand

#### ARTICLE INFO

Article history: Received 10 July 2008 Received in revised form 26 November 2008 Accepted 3 January 2009

PACS: 77.22.Ch 77.22.Gm 77.84.Dv

Keywords: Ceramics Chemical synthesis Electron microscopy Dielectric properties Electrical properties

# ABSTRACT

The electrical properties of (Li, Al)-doped NiO ceramics (i.e.,  $\text{Li}_{0.05}\text{Al}_{0.04}\text{Ni}_{0.91}\text{O}$ ,  $\text{Li}_{0.05}\text{Al}_{0.06}\text{Ni}_{0.89}\text{O}$ , and  $\text{Li}_{0.05}\text{Al}_{0.10}\text{Ni}_{0.85}\text{O}$ ) synthesized by a simple thermal decomposition route were investigated. It was observed that the grain size of the ceramics was affected by the Al content. Impedance analysis confirmed that these ceramics had an electrically heterogeneous structure that was responsible for the giant dielectric response. Interestingly, the Al-dopant had not only the strong effects on the electrical transport character at grain boundaries, but also on the conductivity in the grain interiors.

© 2009 Elsevier B.V. All rights reserved.

# 1. Introduction

High permittivity NiO-based ceramic, a non-perovskite and nonferroelectric material with a formula  $A_x B_y Ni_{1-x-y} O$  (where A are monovalents of Li<sup>+</sup>, Na<sup>+</sup>, K<sup>+</sup> and B are Ti, Al, Ta, Si) [1-7], has attracted considerable attentions in recent years due to its impressive apparent high dielectric permittivity value  $(10^3-10^5)$ , which remains constant in the temperature range of -50-150 °C [1,5]. Moreover, the dielectric properties of such material systems can be tuned by changing the compositions of the additives of A and B [1]. The overall dielectric behavior of these materials is similar to those observed in  $CaCu_3Ti_4O_{12}$  (CCTO) [8–13] and CuO [14–16]. It is now widely accepted that high- $\varepsilon'$  response in such material systems is attributed to Maxwell-Wagner (M-W) relaxation model as a result of semiconducting properties inside grain and insulating properties at grain boundary (GB) [1-3,17]. The M-W relaxation or interfacial polarization usually introduces in materials that have electrically heterogeneous structure, consisting of conducting and insulating parts, which are often observed in the grain and GB, respectively. Under an alternating electric field, free charge carriers in the conducting part are accumulated at the two edge sides of insulating thin-layers, producing the interfacial polarization at the this layers. This is responsible for the observed high- $\varepsilon'$  in these materials. However, such explanation is still incomplete because the fundamental questions regarding the composition-property relationships remain missing. For examples, what are the origins of the semiconductivity and insulation in CCTO? or how do defect dipoles that was induced in NiO-based ceramics contribute to the dielectric and electrical properties of these materials?. Moreover, these materials still have to pass through extensive compatibility test before available for commercial applications in devices. Furthermore, there is a huge obstacle that hinders these materials to be actually used in practical application, i.e., the dielectric loss  $(\tan \delta)$  is too large. Exceptionally,  $K_{0.05}Ti_{0.02}Ni_{0.93}O$  (KTNO) ceramic exhibits high- $\varepsilon'$  and low tan  $\delta$ , but the preparation method of this material requires tedious work with relatively long reaction times [5]. Moreover, some preparing methods for fabrication of KTNO ceramic do not provide such a superior dielectric properties [18]. Normally, it is believed that the strategy for reducing the dielectric loss is an increase in the resistance of GB. However, the grain sizes of these ceramics are also the important factor that has an influence on the electrical properties of transition metal oxides. Therefore, the study of the relationship between dielectric properties and microstructures is important for compositional

<sup>\*</sup> Corresponding author. Tel.: +66 43 202222; fax: +66 43 202374. E-mail addresses: santimaensiri@gmail.com, sanmae@kku.ac.th (S. Maensiri).

tuning of extrinsic ceramic properties of these NiO-based ceramics.

For  $\text{Li}_x \text{Al}_y \text{Ni}_{1-x-y} \text{O}$  system, high- $\varepsilon'$  response in such system prepared by sol–gel method has been attributed to the M–W relaxation model [3]. However, the evidence of electrical heterogeneity which is the origin for the relaxation has not yet been reported. Furthermore, the dielectric dispersion and related electrical response have not yet been studied. Thus, in this paper, we study the electrical response in high- $\varepsilon'$  LANO ceramics prepared by a simple direct thermal decomposition method. It was suggested that the Al-dopant has the remarkable influences on the grain size and the electrical conductivity in the grain interiors of the LANO ceramics. This work has also confirmed that LANO ceramics have electrically heterogeneous structure consisting of semiconducting grain and insulating GB, which is responsible for such a high apparent  $\varepsilon'$ .

# 2. Experimental

In the sample preparation,  $(CH_3COO)_2Ni\cdot 4H_2O$  (UNILAB),  $C_2H_3LiO_2\cdot 2H_2O$  (Fluka), and  $C_2H_5O_4Al$ , (Aldrich) were employed as starting raw materials. The LANO powder and polycrystalline LANO ceramic samples with different addition contents of Al, i.e.,  $Li_{0.05}Al_{0.04}Ni_{0.91}O$  (LANO-04),  $Li_{0.05}Al_{0.06}Ni_{0.89}O$  (LANO-06), and  $Li_{0.05}Al_{0.10}Ni_{0.85}O$  (LANO-10) were designed and prepared by the following procedure. Firstly, stoichiometric amounts of  $(CH_3COO)_2Ni\cdot 4H_2O$ ,  $C_2H_3LiO_2\cdot 2H_2O$ , and  $C_2H_5O_4Al$  were dissolved in distilled water and mixed in alumina crucible using a magnetic stirrer. Then, the mixed powders were decomposed at a temperature of 650 °C for 10 h. The obtained LANO powders were pressed into pellets of 9.5 mm in diameter and ~1–2 mm in thickness by a uniaxial pressing method at 200 MPa. Finally, these pellets were sintered at 1280 °C for 5 h in air.

The LANO powders and sintered ceramics were characterized by X-ray diffraction (XRD) (Philips PW3040, The Netherlands), Field-emission scanning electron microscopy (FE-SEM), and energy-dispersive X-ray spectroscopy (EDS) (Hitachi S-4700, Japan). The ceramic samples were polished and electroded by silver paint on both sides of the disk-shaped samples. They were allowed to dry overnight. The dielectric response of the samples was measured using a Hewlett Packard 4194A impedance gain phase analyzer over the frequency ranging from 100 Hz to 10 MHz and at the oscillation voltage of 1.0 V. The measurements were performed over the temperature ranging from -50 to  $130\,^{\circ}\text{C}$  using an inbuilt cooling–heating system. Each measured temperature was kept constant with an accuracy of  $\pm 1\,^{\circ}\text{C}$ .

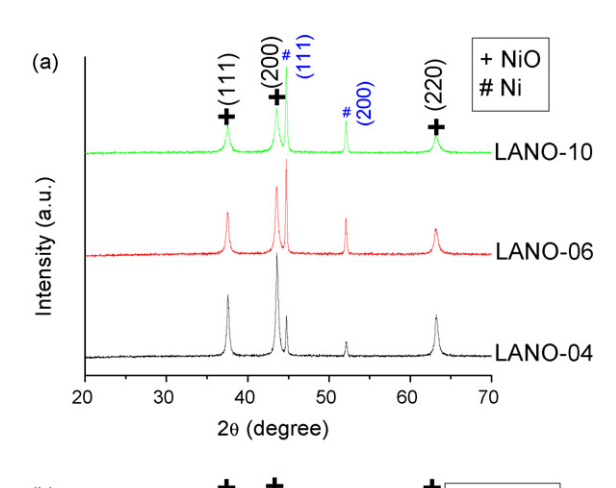
# 3. Results and discussion

The phase formation of LANO materials was characterized by X-ray diffraction. As shown in Fig. 1(a) and (b), all of LANO powders and sintered samples with different Al-doped contents exhibit a main phase of NiO. The main peaks are comparable to that of the powder diffraction pattern of NiO in JCPDS card No. 78-0429. The values of lattice parameter calculated from XRD spectra are close to the value of 0.4177 nm reported in JCPDS card No. 78-0429, as shown in Table 1. It is important to note that the second phase of Ni (JCPDS card No. 04-0850) is still detected in all XRD patterns of LANO powders, and the relative intensity of Ni phase tends to increase with increasing Al-dopant content. This implies that the Al-dopant inhibits the formation of NiO phase. Additionally, a second phase NiAl<sub>2</sub>O<sub>4</sub> can only be observed from XRD pattern of LANO-10 sintered sample. The relative amounts of the NiAl<sub>2</sub>O<sub>4</sub> second phase and NiO phase can be estimated from the XRD pattern of the LANO-10 sample by following relation [7],

NiAl<sub>2</sub>O<sub>4</sub> phase (%) = 
$$\frac{I_{\text{NiAl}_2\text{O}_4}(3\ 1\ 1)}{I_{\text{NiAl}_2\text{O}_4}(3\ 1\ 1) + I_{\text{NiO}}(2\ 0\ 0)} \times 100$$
 (1)

**Table 1** Lattice constants,  $\varepsilon'$ , and activation energies for LANO samples.

	<u> </u>	*			
Samples	Lattice parameter (Å)	$\varepsilon^{\prime}$ (300 K and 1 kHz)	$E_{\rm a}$ (eV)	$E_{\rm g}$ (eV)	$E_{\mathrm{gb}}$ (eV)
LANO-04	4.167	8468	$0.340 \pm 0.003$	$0.354 \pm 0.002$	$0.369 \pm 0.002$
LANO-06	4.168	7396	$0.354 \pm 0.003$	$0.362 \pm 0.001$	$0.374 \pm 0.002$
LANO-10	4.162	6566	$0.373\pm0.004$	$0.367 \pm 0.001$	$0.377\pm0.002$



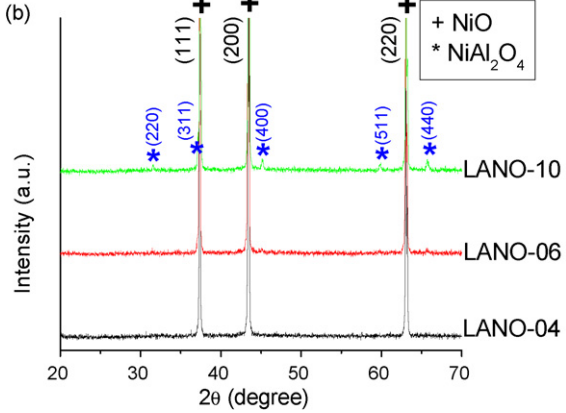


Fig. 1. XRD patterns of (a) LANO powders and (b) LANO sintered samples.

where  $I_{\rm NiAl_2O_4}(3\,1\,1)$  and  $I_{\rm NiO}(2\,0\,0)$  are the major peak intensities for the NiAl<sub>2</sub>O<sub>4</sub> (3 1 1) and NiO (2 0 0) phases, respectively. The calculated relative amount of the observed NiAl<sub>2</sub>O<sub>4</sub> second phase in the LANO-10 ceramic is 7.1%. This can be deduced that just 2.9% of Al-doping can substitute the Ni site in the NiO crystal lattice. Disappearance of such second phase in the XRD patterns of the other two samples might be attributed to the small amount of this phase.

Fig. 2 shows the surface morphologies of the LANO ceramic samples. It is clear that grain size significantly decreases with increasing the Al-doped content. As previously discussed, the phase formation of NiO is suppressed by the Al-dopant. So, it is strongly believed that the grain growth mechanism of LANO ceramics system is affected by the Al-dopant.

The microstructures of the LANO ceramics were analyzed by energy-dispersive X-ray spectroscopy, as showed in Fig. 3, revealing the distribution of Al-dopant at the grain and GB of the LANO-06 ceramic sample. It is clearly seen from the EDS analysis at different regions for the LANO-06 ceramic sample (inset (a) of Fig. 3) that Al-dopant appears in both the grain and GB which is in agreement with the XRD results. This confirms that some parts of the Al-dopant have entered into the grain interiors and other parts have formed the second phase of NiAl<sub>2</sub>O<sub>4</sub> at the GBs.

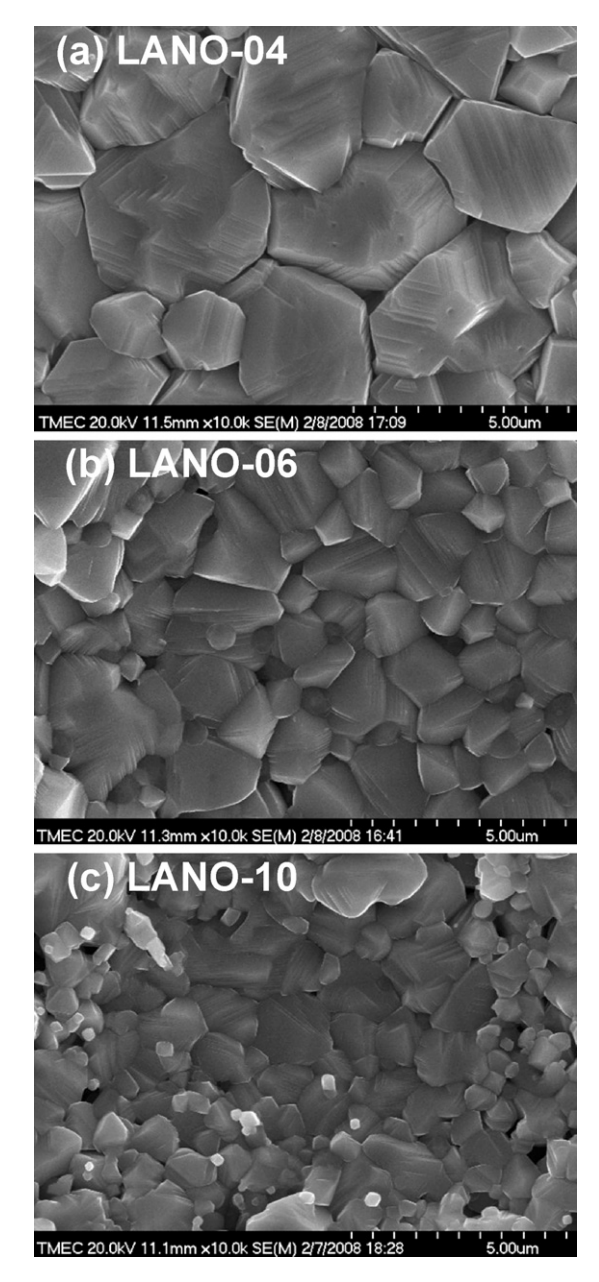
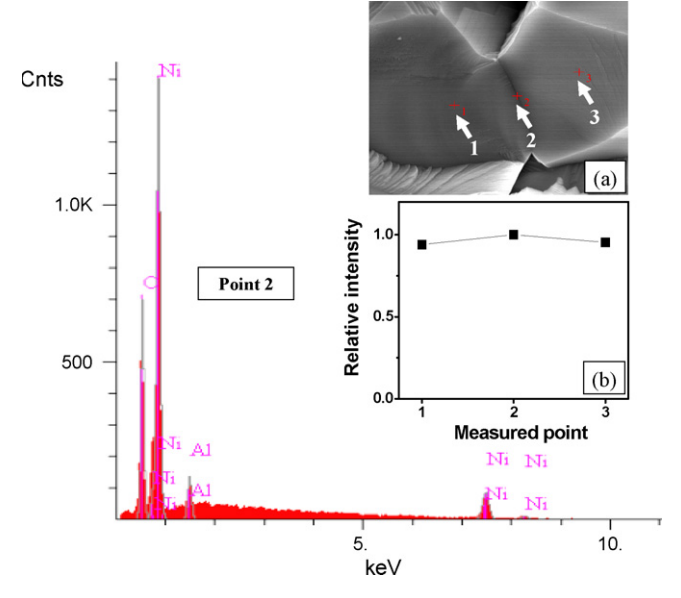


Fig. 2. SEM images of surface morphologies for (a) LANO-04, (b) LANO-06, and (c) LANO-10 sintered samples.

The temperature dependence of dielectric properties of the LANO samples was measured between -60 and 130 °C at the frequency range of 100 Hz–10 MHz. The  $\varepsilon'$  values at 1 kHz for the LANO-04, LANO-06, and LANO-10 samples are about 8468, 7396, and 6566, respectively. These results are consistent with the work reported by Lin et al. [3]. Fig. 4 demonstrates the temperature dependence of  $\varepsilon'$  and loss tangent (tan  $\delta$ ) of LANO-04 ceramic sample. At low frequency,  $\varepsilon'$  is nearly temperature independent over the measured temperature range. With increasing the frequency, however,  $\varepsilon'$  decreases rapidly at the low temperature. This characteristic temperature shifts to the higher temperatures with increasing the frequencies, corresponding to the movement of  $\tan \delta$  peak. Such behavior suggests that the M-W relaxation mechanism possibly play an important role in the high- $\varepsilon'$  response of the LANO ceramics. This dielectric behavior may be ascribed to the migration of excited electrical particles at high temperatures, which has also been observed in the  $CaCu_3Ti_4O_{12}$  [19],  $Ca(Fe_{1/2}Nb_{1/2})O_3$  system [20], and Y<sub>0.03</sub>Ti<sub>0.10</sub>Ni<sub>0.87</sub>O [21].



**Fig. 3.** EDS spectrum of grain boundary (point 2) for LANO-06 ceramic sample; inset (a) is the fractured surface of the LANO-06 sample; inset (b) is the Al element profile obtained from the EDS spectrum at different measured locations as displayed in the inset (a).

We have further studied the frequency dependence of  $\varepsilon'$  and  $\tan\delta$  for the LANO ceramic samples. As shown in Fig. 5, a frequency dependent plateau region of  $\varepsilon'$  is observed at low frequencies for LANO-04 sample, followed by a rapid decrease of  $\varepsilon'$  at higher frequencies. The plateau region expands over a wider frequency range as the temperature increases. The movement of the rapid decrease at high frequencies coincides with the translation of  $\tan\delta$  peak, which it shifts to higher frequency with increasing temperature. Generally, this relaxation behavior can be represented by a Debyelike relaxation relation, and dielectric relaxation time  $\tau$  can be obtained from the relations  $\omega\tau=1$  and  $\omega=2\pi f_p$  where  $f_p$  is the char-

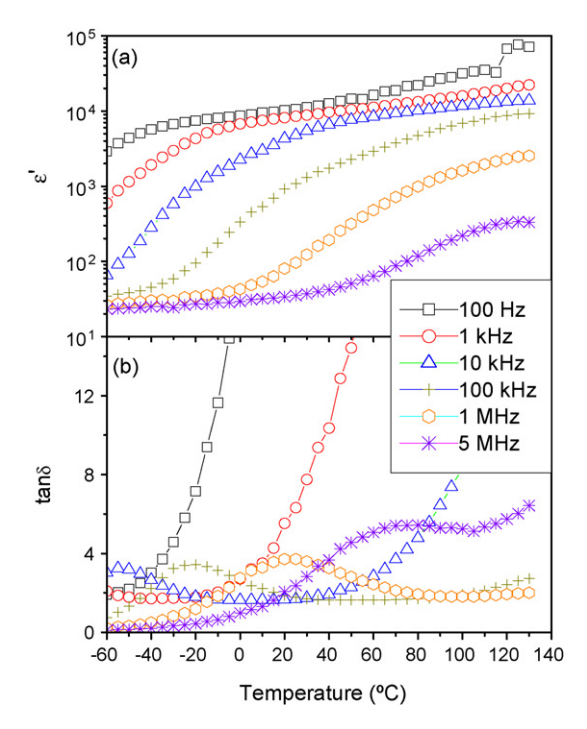


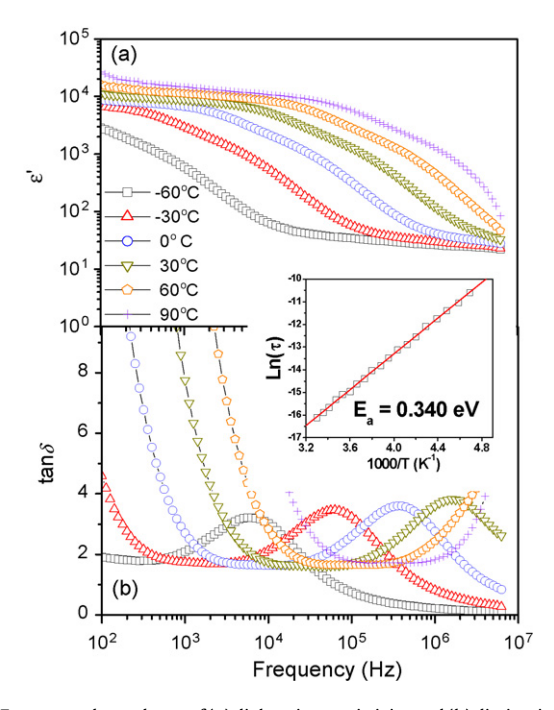
Fig. 4. Temperature dependence of (a) dielectric permittivity and (b) dissipation factor of LANO-04 sample at frequency range of  $100\,\text{Hz}$ -5 MHz.

acteristic frequency corresponding to the peak of  $\varepsilon''$ ,  $\tau$  should follow the relation [22]

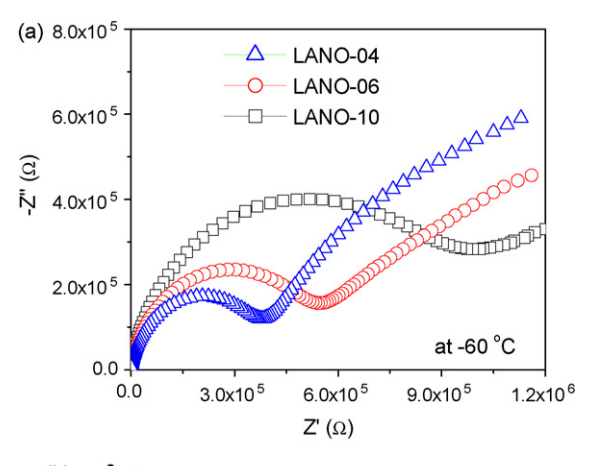
$$\tau = \tau_0 \exp(E_a/k_B T),\tag{2}$$

where  $E_{\rm a}$  is the activation energy required for relaxation,  $\tau_0$  represents the pre-exponential factor,  $k_{\rm B}$  is the Boltzmann constant, and T is the absolute temperature. According to the fitted curve using Eq. (2) as shown in the inset of Fig. 5 for LANO-04 sample, the activation energy of relaxation process ( $E_{\rm a}$ ) was obtained to be  $0.340\pm0.003\,{\rm eV}$ . The frequency dependence of the dielectric response for the samples of LANO-06 and LANO-10 (does not present) is similar to that of LANO-04 sample, but the frequency at the loss peak at the fixed temperature shifts to low frequency range with increasing Al concentration. The  $E_{\rm a}$  values of the samples of LANO-06 and LANO-10 were obtained to be  $0.354\pm0.003$  and  $0.373\pm0.004\,{\rm eV}$ , respectively.

Let us now consider the complex impedance spectroscopy which is a powerful tool in separating out the bulk and GB effects. Data collected from this technique can often be modeled on an ideal equivalent circuit consisting of two parallel RC elements connected in series, one RC element for the bulk and the other for the GB response [23]. Fig. 6(a) shows the complex impedance  $(Z^*)$  plot of all the LANO samples at -60 °C. Two impedance semicircles corresponding to the grain and GB are clearly observed in all of the samples. The observation of two semicircles suggests that the electrically heterogeneous structure exists in our LANO samples and the core/shell model is appropriate for further analysis. Thus, it is strongly indicated that such a presence of electrically inhomogeneous structure is responsible for the high- $\varepsilon'$  in the LANO ceramics. From this result, we propose that for our LANO ceramic samples the GB layers are nonconducting or less conducting, while the bulk grains are semiconductive. Under the applied electric field, the carrier-conducting access is blocked by the insulating GB layer; thus, the opposite charges accumulate at the two edges of the insulator layer to form many microcapacitors, which result in the large- $\varepsilon'$  in these LANO ceramics. This behavior is similar to that of LTNO system [17].



**Fig. 5.** Frequency dependence of (a) dielectric permittivity and (b) dissipation factor of LANO-04 sample at various temperatures; inset shows the Arrhenius plots of the relaxation process.



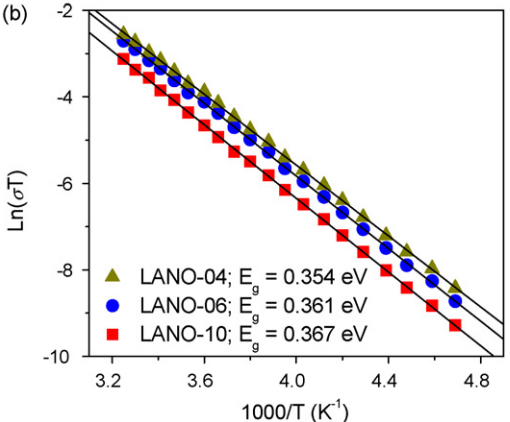


**Fig. 6.** (a) Comparison of impedance spectra for LANO samples at  $-60\,^{\circ}$ C and (b) the Arrhenius plots of the grain conduction of LANO samples.

According to the complex impedance spectra shown in Fig. 6(a), the resistance of grain  $(R_{\rm g})$  and grain boundary  $(R_{\rm gb})$  can be obtained. In polaronic scenario, the temperature dependence of the conductivity is, with a temperature dependence prefactor, ascribed as [17],

$$\sigma \propto T^{-1} \exp(-E/k_{\rm B}T),\tag{3}$$

where E is the conduction activation energy. In general, the GB effects on electric conductivity may originate from a GB potential barrier, which should be ascribed by the Al-rich boundary for LANO system [3]. From Fig. 6(b), we found that both  $\sigma_{\rm g}$  and  $\sigma_{\rm gb}$  values at different temperatures follow Eq. (3). Accordingly, the calculated values of the conduction activation energy inside the grain  $(E_{\rm g})$  were obtained to be  $0.354\pm0.002$ ,  $0.361\pm0.001$ , and  $0.367\pm0.001$  eV for LANO-04, LANO-06, and LANO-10, respectively. While, the estimated values of the GB activation energy  $(E_{\rm gb})$  were obtained to be  $0.369\pm0.002$ ,  $0.374\pm0.002$ , and  $0.377\pm0.002$  eV for LANO-04, LANO-06, and LANO-10, respectively. The observation of the small increase in  $E_{\rm g}$  with increasing the Al content may be because the parts of Al that have entered into the NiO crystal lattice (as clearly seen in Fig. 3) have small different amounts. Because of the difference in valence states of Al<sup>3+</sup> and Ni<sup>2+</sup>, the defects can be introduced inside the grains of the LANO ceramics, i.e.,

$$Al_2O_3 \xrightarrow{NiO} 2Al_{Ni} \cdot + V_{Ni}'' + 3O_o.$$

This has an influence of the electric conductivity of the grains, which induces the variation of the  $E_a$  values. This behavior was also observed in  $\text{Li}_x\text{Ti}_y\text{Ni}_{1-x-y}\text{O}$  ceramics system [17].

Generally, for  $A_x B_y N i_{1-x-y} O$  systems, B-dopants (Ti, Al, Si, Ta) normally form a second phase at GB enclosing the semiconduct-

ing core grain of A-doped NiO. Thus, the electrical characters at GB should be modified by the B-dopant. In this work, it is clear that some parts of Al-dopant accumulated at the GBs and formed the second phase of NiAl<sub>2</sub>O<sub>4</sub>, as evidenced in Figs. 1(b) and 3. Moreover, it was found that the NiAl<sub>2</sub>O<sub>4</sub> ceramic is a good insulator with the value of resistance of more than 100 M $\Omega$  cm (does not show), and as a result the GB potential barrier can be ascribed to the appearance of such second phase of NiAl<sub>2</sub>O<sub>4</sub> at GBs. Therefore, the observed high- $\varepsilon'$  in the samples of LANO ceramic is due to the M–W polarization mechanism, i.e., charge carriers in the semiconducting grain are accumulated at the insulating GB layer under the influence of electric field. Interestingly, the B-dopant (Al) in our LANO system has also a remarkable effect on the electrical properties in the grain interiors, where the resistance of the grain decreases with increasing the Al content, as evidenced in Fig. 6. This result implies that the Al-dopant may not only be able to improve the electrical character at GBs, but also strongly affect on the electrical properties inside the grains. Moreover, the effect of Al-dopant on microstructure was also clearly observed. The reason for this is that most of Al-dopant in our LANO ceramics has entered into the grains, while the concentration of Al at the GB of each sample does not significant difference in composition. This leads to the little change in  $\varepsilon'$ . It is worth nothing that all of the B-dopants in NiO-based ceramics have remarkable impact on the electrical properties inside grain due to the different physical nature of B-doped and the different synthesis method. As well known, the strategy for reducing the dielectric loss in high dielectric ceramics is an increase in the GB resistance [24]. In our LANO samples, however, the tan  $\delta$  values do not significant change with the concentrations of Al-dopant. This suggests that the electrical properties of GB for all the LANO samples are not significant difference. This observation may be attributed to the synthesis method used in the present work and/or the physical nature of Al-dopant. However, it is beyond the scope of our work and further work is needed to make a more detailed explanation. Of great interest, it is very important to seek for the preparation method that provides a good distribution of B-dopant only at GBs and to explore the suitable B-dopant which can modify the defect equilibrium at GB, leading to the higher resistance of GB.

# 4. Conclusion

High dielectric LANO ceramics have been successfully prepared by a simple thermal decomposition method. The microstructure and phase formation of the prepared LANO powders and ceramics were characterized by XRD and FE-SEM. The phase formation of NiO-based ceramics and the grain growth mechanism was suppressed by the Al-dopant. This work demonstrates that the high- $\varepsilon'$  of the LANO decreases with increasing the Al-dopant content. Giant- $\varepsilon'$  response in such ceramics was attributed to the appearance of electrically heterogeneous structure, responsible for the observed high- $\varepsilon'$  in our LANO samples. Our results also showed that the Al-dopant has a strong effect on electrical transport in the grain interiors.

# Acknowledgments

The authors would like to thank the Department of Physics, Ubon Ratchathani University for providing XRD facilities, and the Thai Microelectronics Center (TMEC) for FE-SEM facilities. S. Tangwancharoen and P. Thongbai would like to thank The National Science and Technology Development Agency for financial supports of their studies through the YSTP and TGIST Programs, respectively. This work is financially supported by The Thailand Research Fund (TRF) and The Higher Commission on Education (CHE), The Ministry of Education, Thailand.

# References

- [1] J. Wu, C.W. Nan, Y. Lin, Y. Deng, Phys. Rev. Lett. 89 (2002) 217601.
- S. Maensiri, P. Thongbai, T. Yamwong, Acta Mater. 55 (2007) 2851. Y. Lin, J. Wang, L. Jiang, Y. Chen, C.W. Nan, Appl. Phys. Lett. 85 (2004) 5664. Y. Lin, L. Jiang, R. Zhao, C.W. Nan, Phys. Rev. B 72 (2005) 014103.
- [5] P.K. Jana, S. Sarkar, B.K. Chaudhuri, Appl. Phys. Lett. 88 (2006) 182901.
- [6] P.K. Jana, S. Sarkar, H. Sakata, T. Watanabe, B.K. Chaudhuri, Phys. D: Appl. Phys. 41 (2008) 065403.
- Y.J. Hsiao, Y.S. Change, T.H. Fang, T.L. Chai, C.Y. Chung, Y.H. Chang, J. Phys. D: Appl. Phys. 40 (2007) 863.
- [8] M.A. Subramanian, D. Li, N. Duan, B.A. Reisner, A.W. Sleight, J. Solid State Chem. 151 (2000) 323.
- A.P. Ramirez, M.A. Subramanian, M. Gardel, G. Blumberg, D. Li, T. Vogt, S.M. Shapiro, Solid State Commun. 115 (2000) 217.
- [10] P. Thongbai, C. Masingboon1, S. Maensiri, T. Yamwong, S. Wongsaenmai, R. Yimnirun, I. Phys.: Condens, Matter 19 (2007) 236208.
- [11] S. Maensiri, P. Thongbai, T. Yamwong, Appl. Phys. Lett. 90 (2007) 202908.
- [12] C. Masingboon, P. Thongbai, S. Maensiri, T. Yamwong, S. Seraphin, Mater. Chem. Phys. 109 (2008) 262.
- [13] P. Thongbai, T. Yamwong, S. Maensiri, J. Appl. Phys. 103 (2008) 114107; S. Sarkar, P.K. Jana, B.K. Chaudhuri, H. Sakata, Appl. Phys. Lett. 89 (2006) 212905.
- [14] P. Thongbai, S. Meansiri, T. Yamwong, J. Appl. Phys. 104 (2008) 036107.
- [16] P. Thongbai, T. Yamwong, S. Maensiri, Solid State Commun. 147 (2008) 385.
- Y.H. Lin, M. Li, C.W. Nan, J. Li, J. Wu, J. He, Appl. Phys. Lett. 89 (2006) 032907.
- [18] P. Thongbai, T. Yamwong, S. Maensiri, unpublished.
- [19] W. Li, R.W. Schwartz, A. Chen, J. Zhu, Appl. Phys. Lett. 90 (2007) 112901.
- [20] Y.Y. Liu, X.M. Chen, X.Q. Liu, L. Li, Appl. Phys. Lett. 90 (2007) 262904.
- [21] B. Cheng, Y.H. Lin, A. Mei, J.N. Cai, C.W. Nan, J. He, Appl. Phys. Lett. 92 (2008) 142903.
- [22] J.R. Macdonald, Impedance Spectroscopy, Wiley, New York, 1987.
- [23] D.C. Sinclair, T.B. Adams, F.D. Morrison, A.R. West, Appl. Phys. Lett. 80 (2002) 142903.
- [24] E.A. Patterson, S. Kwon, C.C. Huang, D.P. Cann, Appl. Phys. Lett. 87 (2005) 182911.

# Nanocrystalline CaCu<sub>3</sub>Ti<sub>4</sub>O<sub>12</sub> powder by PVA sol-gel route: synthesis, characterization and its giant dielectric constant

Chivalrat Masingboon • Prasit Thongbai • Santi Maensiri • Teerapon Yamwong

Received: 30 August 2007 / Accepted: 24 November 2008 © Springer-Verlag 2009

**Abstract** Nanocrystalline CaCu<sub>3</sub>Ti<sub>4</sub>O<sub>12</sub> powders were synthesized by a simple PVA sol-gel route and calcined at 700 and 800°C in air for 8 h. The diameter of the powders ranges from 40–100 nm. The calcined CaCu<sub>3</sub>Ti<sub>4</sub>O<sub>12</sub> powders were characterized by TG-DTA, XRD, FTIR, SEM, and TEM. Sintering of the powders was conducted in air at 1100°C for 16 h. The XRD results indicated that all sintered samples had a typical perovskite CaCu<sub>3</sub>Ti<sub>4</sub>O<sub>12</sub> structure although the sintered samples contained some amount of CaTiO<sub>3</sub>. SEM of the sintered CaCu<sub>3</sub>Ti<sub>4</sub>O<sub>12</sub> ceramics showed the average grain sizes of 13–15 µm. The samples exhibit a giant dielectric constant,  $\varepsilon' \sim 10^5$  at 150 to 200°C with weak temperature dependence below 1 kHz in the sample sintered using the powders calcined at 700°C. The Maxwell–Wagner polarization mechanism is used to explain the high permittivity in these ceramics. It is also found that all sintered samples have the same activation energy of grains, which is  $\sim$ 0.122 eV.

**PACS** 61.72.Ff · 77.22Gm · 81.05.Je · 81.07.Wx · 81.20.Ev

C. Masingboon · P. Thongbai · S. Maensiri (☒) Small & Strong Materials Group (SSMG), Department of Physics, Faculty of Science, Khon Kaen University, Khon Kaen 40002, Thailand

e-mail: sanmae@kku.ac.th Fax: +66-43-202374

S. Maensiri

e-mail: santimaensiri@gmail.com

Published online: 13 January 2009

T. Yamwong

National Metals and Materials Technology Center (MTEC), Thailand Science Park, Pathumthani 12120, Thailand 1 Introduction

Materials with high dielectric constant are widely used in technological applications such as capacitors and memory devices. Giant dielectric constants allow smaller capacitive components, thus offering the opportunity to decrease the size of electronic devices [1]. Recently, a newly discovered a perovskite-type compound, CaCu<sub>3</sub>Ti<sub>4</sub>O<sub>12</sub>, (CCTO) was extensively investigated due to its giant dielectric constant ( $\varepsilon' \sim 10^4 - 10^5$ ) and weak temperature dependence in a wide temperature range from -173 to  $327^{\circ}$ C [2–5]. This material does not undergo any structural change over the same temperature range [2, 3] although its dielectric constant abruptly decreases to less than 100 below -173°C and shows a Debye-like relaxation [6]. The characteristic relaxation frequency follows approximately the Arrhenius law. In addition to its interesting dielectric property, CCTO has remarkably strong linear current-voltage characteristics without the addition of dopants [7]. These excellent properties render this material particularly attractive for a wide range of applications.

So far, several models of the dielectric behavior of CCTO material have been proposed to be due to either intrinsic or extrinsic effect. Since the giant dielectric response of this material was found to be very sensitive to the microstructure (such as grain size) and processing conditions (such as sintering temperature and time, cooling rate, and partial pressure) [5, 6, 8–10], more investigations tend to believe that the high dielectric constant originates from the extrinsic effect such as internal barrier layer capacitor (IBLC) [8, 10], contact-electrode effect [11, 12], and special inhomogeneity of local dielectric response [13]. Although still unclear, the IBLC explanation of extrinsic mechanism is widely accepted.



CCTO powder is usually prepared by a standard solidstate reaction method [2–5]. This method requires tedious work and a high temperature in the powder preparation process. Moreover, it suffers from the disadvantages of inhomogeneity. In contrast, synthesis from a solution affords the reaction with a homogeneous mixing of the metal ions at the atomic scale, and at lower temperature in the powder preparation process [14]. However, there have been only a few reports on the solution methods to synthesize CCTO powders [6, 15–18]. Therefore, alternative simple solution routes benign precursors for preparation of CCTO powders are still a challenge.

In this study, we report the synthesis and giant dielectric properties of CCTO prepared by the simple PVA sol–gel route using  $\text{Ca}(\text{NO}_3)_2 \cdot 4\text{H}_2\text{O}$ ,  $\text{Cu}(\text{NO}_3)_2 \cdot 4\text{H}_2\text{O}$ , and Titanium(diisoproproxide) bis(2,4-pentanedionate). The synthesized nanocrystalline CCTO powders were characterized by thermogravimetric and differential thermal analysis (TG-DTA), X-ray diffraction (XRD), Fourier-Transform Infrared (FT-IR) spectroscopy, scanning electron microscopy (SEM) and transmission electron microscopy (TEM). The giant dielectric behaviors of the sintered CCTO were also investigated.

# 2 Experimental procedure

Nanocrystalline CCTO was prepared by a PVA sol-gel route. In a typical procedure, Ca(NO<sub>3</sub>)<sub>2</sub> · 4H<sub>2</sub>O (99.9% purity, Kento, Japan), Cu(NO<sub>3</sub>)<sub>2</sub> · 4H<sub>2</sub>O (99.5% purity, Carlo Erba Reacgenti, Italy), and 75 wt% Titanium(diisoproproxide) bis(2,4-pentanedionate) in 2-propanol (99%, Acros organics, USA), in a mole ratio corresponding to the nominal composition of CaCu<sub>3</sub>Ti<sub>4</sub>O<sub>12</sub>, were dissolved in 60 ml de-ionized water under vigorous stir at room temperature (27°C) until homogeneous solution was obtained. The nitrate solution was then mixed in 1140 ml 5 wt% poly(vinyl alcohol) ( $M_n = 72,000$ , Fluka) aqueous solution in the ratio of 1:4 with stirring and heating at 80°C until a viscous gel was formed. Then, the gel was dried at 100°C. This blacksolid mass precursor was ground and passed through 106 µm sieve. In order to determine the temperature of possible decomposition and crystallization of the nanoparticles, the dried precursor was subjected to thermogravimetricdifferential thermal analysis (TG-DTA) (Pyris Diamond TG-DTA, PerkinElmer Instrument, USA). The crystallization seemed to occur at temperature above 600°C (Fig. 1). The dried CCTO precursor then was calcined in a boxfurnace at 700 and 800°C for 8 h in air. The calcined CCTO powders were reground and passed through 106 µm sieve again to break up large agglomerates. The prepared CCTO powers were characterized by X-ray diffraction (PW3040 Philips X-ray diffractometer with CuKα ra-

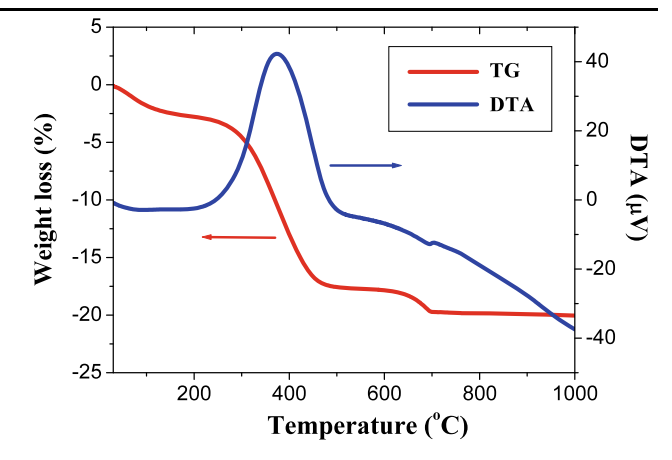


Fig. 1 The TG/DTA curves of the thermal decomposition of  $CaCu_3Ti_4O_{12}$  precursor at a heating rate of 15°C/min in static air

diation ( $\lambda=0.15406$  nm), The Netherlands), Fourier Transform infrared spectrometer (Spectrum One FT-IR Spectrometer, PerkinElmer Instruments, USA), scanning electron microscopy (LEO SEM VP1450, UK) and transmission electron microscopy (TEM, JEOL TEM 2010, Japan).

The prepared CCTO powders were pressed uni-axially in a 16 mm die with an applied pressure of 100 MPa. The compacts were pressureless-sintered at 1100°C for 16 h in air in a box-furnace with heating and cooling rates of 5°C/min. The sintered disc samples of  $\sim$ 14 mm in diameter with a thickness of ~2 mm were obtained. The average grain size of each sintered CCTO ceramic was measured using a standard line intercept technique from SEM micrographs of sintered CCTO surfaces and counting at least 200 intercepts for each micrograph. Throughout this article, we assigned symbols of CCTO\_PVA700 and CCTO\_PVA800 for the sintered CCTO samples fabricated using the CCTO powders calcined at 700 and 800°C, respectively. The capacitance, C, and loss tangent,  $\tan \delta$ , were carried out as a function of frequency (100 Hz to 10 MHz) and temperature (-40 to 200°C), using a Hewlett Packard 4194A Impedance Gain Phase Analyzer at an oscillation voltage of 1 V. Each measured temperature was kept constant with an accuracy of ±1°C. Silver paint was coated on both surfaces of the samples and dried overnight. The complex permittivity,  $\varepsilon^*$ , was calculated as follows:

$$\varepsilon^* = \varepsilon' - i\varepsilon'',\tag{1}$$

where

$$\varepsilon' = \frac{Cd}{\varepsilon_0 A},\tag{2}$$

$$\varepsilon'' = \varepsilon' \tan \delta, \tag{3}$$

and where  $\varepsilon_0$  is the permittivity in free space, A is the sample area, and d is the sample thickness.



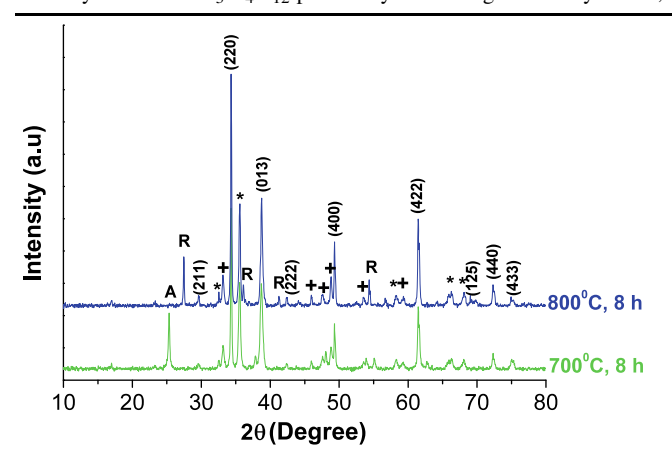


Fig. 2 XRD patterns of the  $CaCu_3Ti_4O_{12}$  nanopowders calcined in air for 8 h at 700 and  $800^{\circ}C$  (+:  $CaTiO_3$ , \*: CuO, A: Anatase– $TiO_2$ , R: Rutile– $TiO_2$ )

## 3 Results and discussion

The simultaneous TG-DTA curves of the gel precursor in flowing air are shown in Fig. 1. The TG curve in Fig. 1 shows a minor weight loss step between ~30 and 300°C. A major weight loss was observed between 300 and 600°C, and almost no weight loss was observed at above 600°C. The first weight loss (30 to 300°C) is related to the losses of moisture, trapped solvent (water and carbon dioxide), alkoxide, and nitrates. A major weight loss was observed between 300 and 600°C, relating to the losses of organic species associated in the precursor, or the residual carbon. Almost no weight loss could be observed at above 600°C, suggesting the formation of crystalline CCTO as a decomposed product. This is confirmed by the XRD results as shown in Fig. 2. On the DTA curve (Fig. 1), one exothermic was observed at 375°C. The one exothermic peak confirms that the thermal events were associated with the burnout of organic species involved in the precursor powders of the residual carbon or due to direct crystallization of CCTO from the amorphous component. No further weight loss and no thermal effect were observed above 600°C, indicating that no decomposition occurs above this temperature. Note that this precursor was calcined in air at 700 and 800°C for 8 h.

Figure 2 shows XRD patterns of CCTO powders after calcination in air at (a) 700°C and (b) 800°C for 8 h. The main peaks of all calcined CCTO powders are comparable to those of the standard powder XRD pattern of CCTO in the JCPDS card No. 75-2188. In addition, the following phases of CaTiO<sub>3</sub> (JCPDS card No. 82-0228), CuO (JCPDS card No. 80-0076), Anateses–TiO<sub>2</sub> (JCPDS card No. 78-2486), and Rutile–TiO<sub>2</sub> (87-0920) are also observed. From the line broadening of the main peaks, the crystallite size (*D*) was estimated using the Scherrer formula [19]:

$$D = K\lambda/(\beta\cos\theta),\tag{4}$$

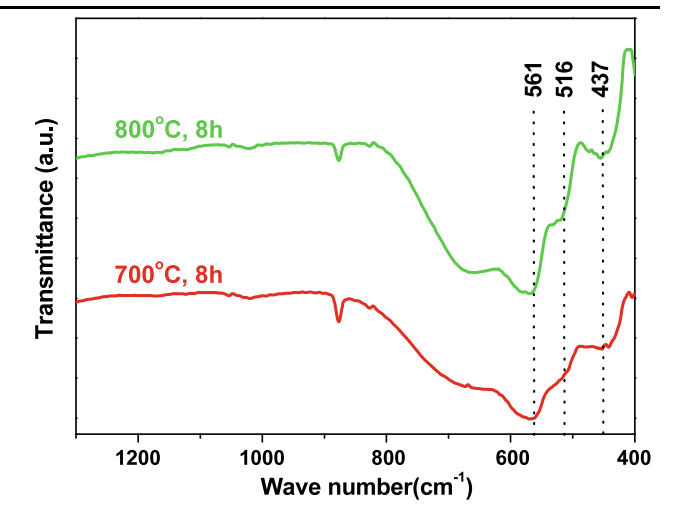


Fig. 3 FT-IR patterns of the  $CaCu_3Ti_4O_{12}$  nanopowders calcined in air for 8 h at 700 and  $800^{\circ}C$ 

**Table 1** Summary of particle size analysis obtained from XRD and TEM; and lattice parameter (from XRD) of CCTO powders compared to the ASTM value

Material	Particle size from XRD (nm)	Particle size from TEM (nm)	Lattice parameter <i>a</i> (Å)
ASTM(75-2188)	_	_	$7.391 \pm 0.001$
ASTM(75-2188) 700°C powders	$-55.9 \pm 20.8$	$-42.9 \pm 15.9$	$7.391 \pm 0.001$ $7.383 \pm 0.001$

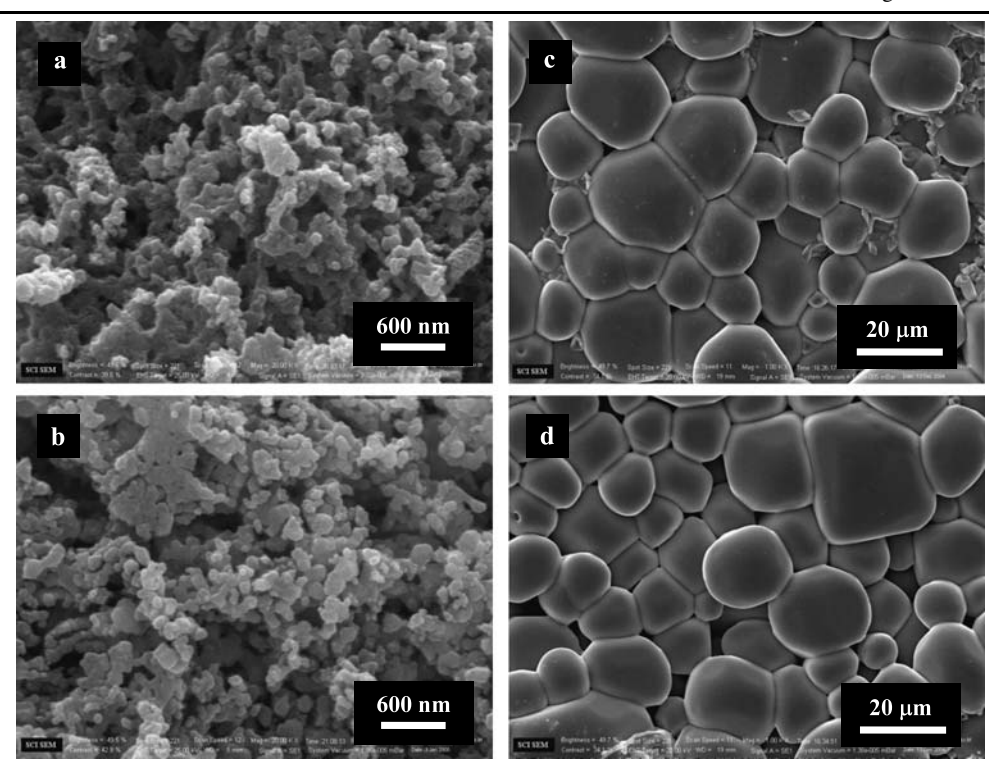
where  $\lambda$  is the wavelength of the X-ray radiation, K is a constant taken as 0.89,  $\theta$  is the diffraction angle.  $\beta$  is the full width at half maximum (FWHM) and is given by  $\beta = (\beta_O^2 - \beta_i^2)^{1/2}$ , where  $\beta_O$  and  $\beta_i$  are the widths from the observed X-ray peak and the width due to instrumental effects, respectively. The particle sizes are found to be  $55.9 \pm 20.8$  and  $63.3 \pm 31.6$  nm for the powders calcined at 700 and  $800^{\circ}$ C, respectively. The values of lattice parameter  $\alpha$  calculated from the XRD spectra were obtained to be  $7.383 \pm 0.001$  and  $7.390 \pm 0.001$  Å for the CCTO powders calcined at 700 and  $800^{\circ}$ C, respectively. The particle sizes and lattice parameters are also summarized in Table 1.

Figure 3 shows FT-IR spectra of the dried precursor and CCTO powders after calcination in air at 700 and 800°C for 8 h. The calcined CCTO powders show the main absorption bands at 561, 516, and 437 cm<sup>-1</sup>. These bands are assigned to the absorption regions for Ti ion, which are associated to  $\nu_{\text{Ti-O}}$  of 653–550 cm<sup>-1</sup> and  $\nu_{\text{Ti-O-Ti}}$  of 495–436 cm<sup>-1</sup> [20, 21].

Morphology of the calcined CCTO powders and microstructure of the sintered CCTO ceramics' samples revealed by SEM are shown in Fig. 4. Figure 4(a) and 4(b) show CCTO particles with sizes of about 60 and 100 nm for the 700 and 800°C calcined samples, respectively. These



Fig. 4 SEM micrographs of the CCTO powders and sintered CCTO materials. a, b Powders calcined for 8 h in air at 700 and 800°C, respectively. c, d Microstructure of the sintering CCTO\_PVA700 and CCTO\_PVA800, respectively



values were larger than those obtained from X-ray line broadening calculation. Some agglomerates were observed in all of the calcined powders. The particle size of the powder increased with increasing calcination temperature. After sintering at  $1100^{\circ}\text{C}$  for 16 h, the bulk CCTO ceramics with different microstructure were obtained. The CCTO\_PVA700 (Fig. 4(c)) and CCTO\_PVA800 (Fig. 4(d)) showed mean grain sizes of  $14.7 \pm 4.2~\mu m$  and  $13.5 \pm 4.8~\mu m$ , respectively.

Figure 5 shows TEM images and the corresponding selected area electron diffraction (SAED) patterns of the calcined CCTO powders. It is clearly seen from the TEM bright-field images that both powder samples consist of nanocrystalline CCTO particles, whose size increases with increasing calcination temperature although a small amount of ATO (Anatases–TiO<sub>2</sub>) was present in the 700°C calcined sample. The 700°C calcined sample contains nanoparticles of  $42.9 \pm 15.9$  nm in size whereas the  $800^{\circ}$ C calcined sample contains nanoparticles of  $97.6 \pm 29.3$  nm. The observed particle sizes are in good agreement with results determined from X-ray line broadening (see summary in Table 1). Electron diffraction of particles with higher calcination temperature contains more intense spots as shown in the 800°C calcined powders, indicating the larger particle size of highly crystalline compared to the 700°C calcined samples. The interplanar spacings  $(d_{hkl})$  measured from the selected-area electron diffraction patterns are in good agreement with the values obtained from the standard data JCPDS: 75-2188 (for CCTO) and 78-2486 (for ATO) as summarized in Table 2.

**Table 2** Measured interplanar spacings ( $d_{hkl}$ ) obtained from selectedarea electron diffraction patterns of CCTO powders calcined at 700 and 800°C for 8 h shown in Fig. 5. Corresponding values from the standard data JCPDS: 75-2188 are also provided for a comparison

Ring	Measured interplated of CCTO samples	1 0	Standard d	
	700°C powder	800°C powder	d <sub>hkl</sub> (Å)	h k l
$R_1$	_	3.7258	3.6955	200
$R_2$	2.6556	2.6415	2.6131	220
$R_3$	2.3113	2.3113	2.3240	222
$R_4$	1.8629	1.8491	1.8477	400
$R_5$	1.6789	_	1.6526	024
R <sub>6</sub>	_	1.5086	1.5037	422

Figure 6 shows XRD patterns of the CCTO ceramics sintered in air at 1100°C for 16 h, confirming a main phase of CCTO and a small amount of CaTiO3 in both the CCTO\_PVA700 and CCTO\_PVA800. The values of lattice parameter a calculated from the XRD spectra were 7.387  $\pm$  0.003 and 7.388  $\pm$  0.003 Å for the CCTO\_PVA700 and CCTO\_PVA800, respectively (see summary in Table 3).

Figure 7 shows the real and imaginary parts of dielectric dispersion for the samples of CCTO\_PVA700 and CCTO\_PVA800 at various temperatures between -40 and -10°C. By considering these results, we cannot apply the empirical Cole-Cole relation to fit these data because the samples contain numerous grain boundaries or grain bound-



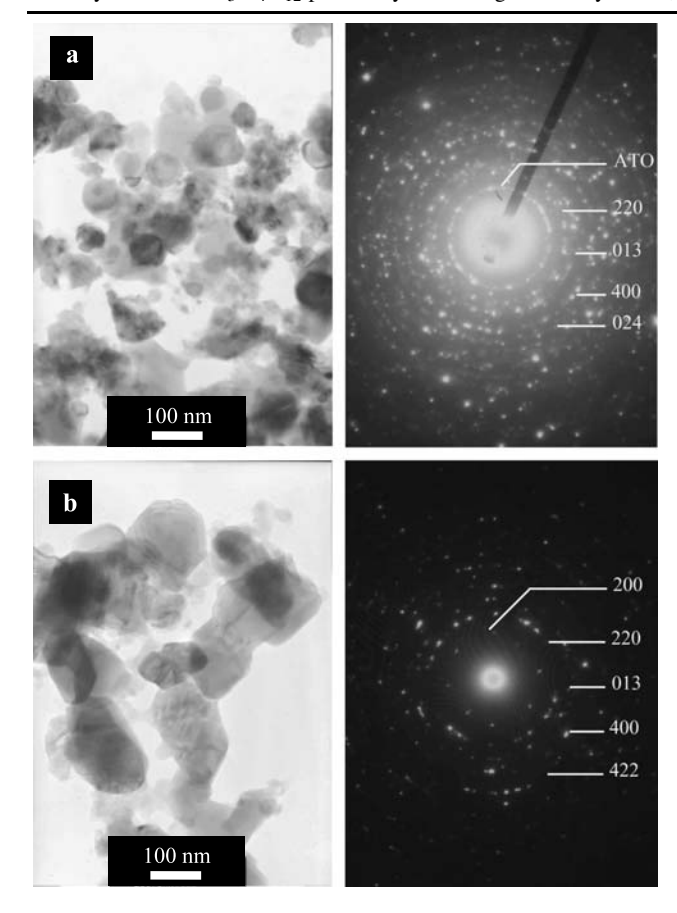


**Fig. 5** Bright-field TEM images with corresponding selected-area electron diffraction (SAED) pattern of  $CaCu_3Ti_4O_{12}$  powders calcined in air for 8 h at different temperatures: **a** 700°C and **b** 800°C, respectively (ATO: Anatase– $TiO_2$ )

aries relaxation which was affected by low frequency [22]. However, it is clearly seen from Figs. 7(a.1) and 7(b.1) that both samples have very high dielectric constant,  $\varepsilon'$ , of  $\sim 2 \times 10^4$  (at 1 kHz). From the inset of Fig. 7(a.1), the sample exhibits a giant dielectric constant,  $\varepsilon' \sim 10^5$  at 150 to 200°C with weak frequency dependence below 1 kHz in the CCTO\_PVA700 while its  $\tan \delta$  is high  $(\tan \delta \sim 7)$  at a frequency of 100 Hz and temperature from 150 to 200°C. The values are similar to those reported by Bender and Pan [9] who reported values of  $\varepsilon' \sim 10^4 - 10^5$  (at 1 kHz) for CCTO samples prepared from a solid state reaction method. These values, however, are much higher than  $10^3 - 10^4$  of the solution routed CCTO ceramics reported by Liu et al. [6], Jha et al. [15], and Jin et al. [17].

The imaginary parts of dielectric dispersion,  $\varepsilon''$ , are shown in Figs. 7(a.2) and 7(b.2) for the samples of CCTO\_PVA700 and CCTO\_PVA800, respectively. We can apply the Debye-like relaxation model to these data since there are the relaxations contributed from the grains. The  $\varepsilon''$  shows a clear Debye-like relaxation peak shifting from a constant value at low frequency to a small saturated value at higher frequency. The electrical response from the grains has a very

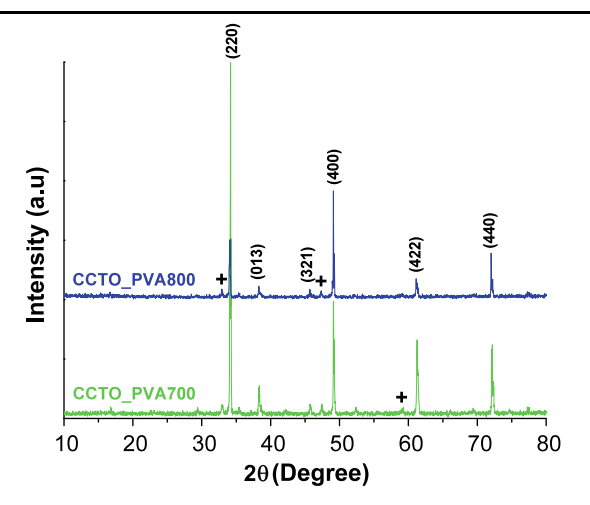


**Fig. 6** XRD patterns of **a** 700°C; and **b** 800°C, respectively. All sintering was done in air at 1100°C for 16 h. The indexed planes indicated in all pattern are for CCTO main structure (+: CaTiO<sub>3</sub>)

**Table 3** Summary of grain size (from SEM), lattice parameter (from XRD) and activation energy of grains (obtained from the curve fitting using (5) and (7))

Material	Grain size (μm)	Lattice parameter <i>a</i> (Å)	Activation energy of grains (eV)	Activation energy of the dc conductivity (eV)
ASTM(75-2188)	_	$7.391 \pm 0.001$	_	_
CCTO-PVA700	$14.7 \pm 4.2$	$7.387 \pm 0.003$	0.122	0.132
CCTO-PVA800	$13.5 \pm 4.8$	$7.388 \pm 0.003$	0.122	0.112

high response frequency because of their small resistance and capacitance [6]. We can determine the dielectric relaxation time,  $\tau$ , by following the Arrhenius law of

$$\tau = \tau_0 \exp(E_\tau / k_B T),\tag{5}$$

where  $\tau_0$  is the pre-exponential factor,  $E_{\tau}$  is the activation energy for the relaxation,  $k_B$  is the Boltzmann constant, and T is the absolute temperature. The activation energy of an electrical response, at different temperature can be derived from the response time ( $\tau=1/2\pi f$ , where f is the response frequency at which the imaginary part of the complex impedance has a maximum). From the fitting shown in Fig. 8, we obtain the activation energy of the dielectric relaxation for CCTO\_PVA700 and CCTO\_PVA800 to be of the same value of 0.122 eV.

Figure 9 shows the fit of the  $\varepsilon''$  of the CCTO ceramics (CCTO PVA700 and CCTO PVA800) to the equation [23]

$$\varepsilon'' \approx \frac{\sigma_{\rm dc}}{\varepsilon_0 \omega},$$
 (6)

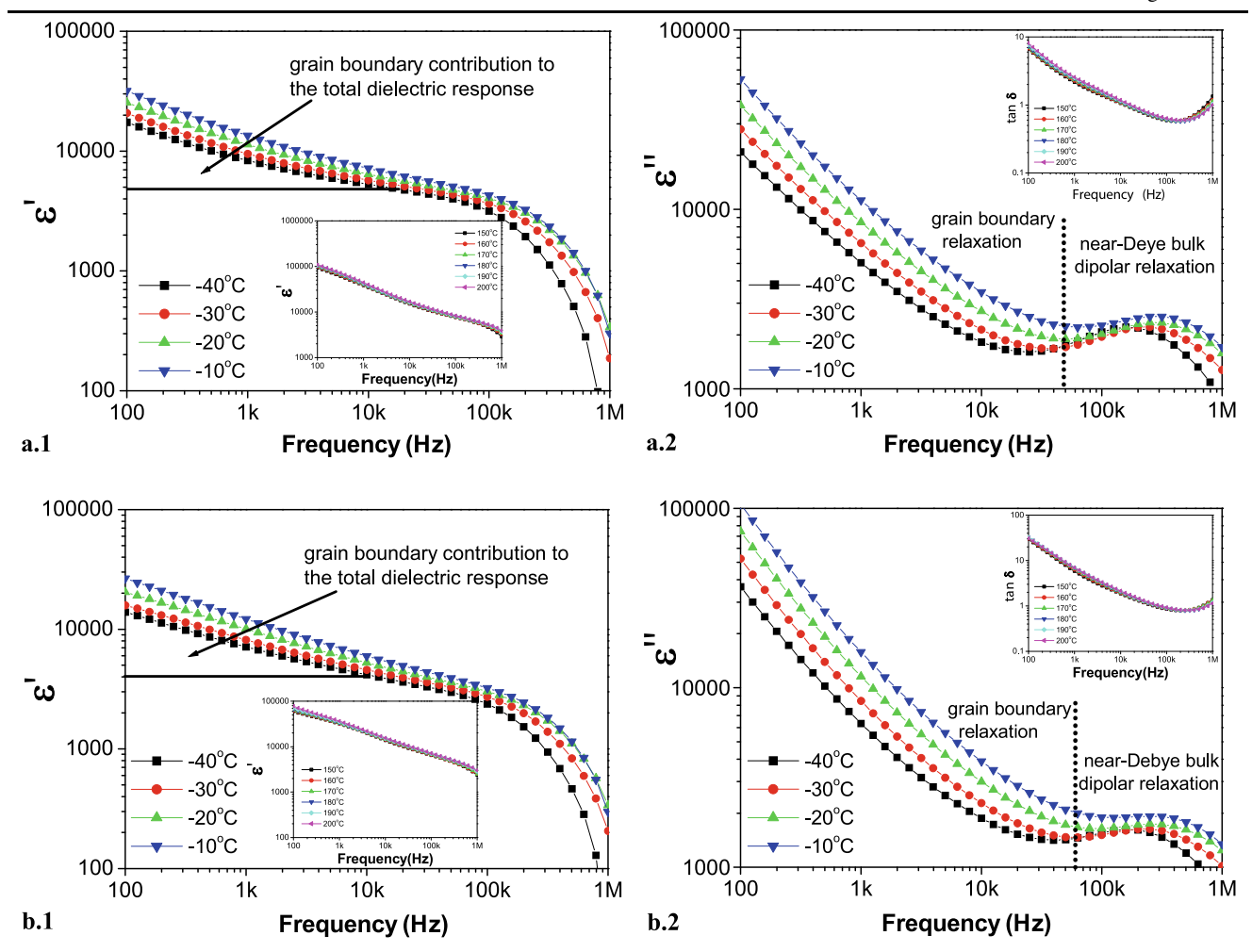


Fig. 7 The frequency dependence of the dielectric constant,  $\varepsilon^*$ , at low temperature between -40 and  $-10^{\circ}$ C for a.1, a.2 CCTO\_PVA700 and b.1, b.2 CCTO\_PVA800, respectively. a.1, b.1 display the real part  $\varepsilon'$ ;

and **a.2**, **b.2** display the imaginary part  $\varepsilon''$ . The *inset* in **a.1**, **b.1** shows the real part  $\varepsilon'$  and **a.2**, **b.2** shows  $\tan \delta$  at high temperature between 150 and 200°C for CCTO\_PVA700 and CCTO\_PVA800, respectively

where  $\sigma_{dc}$  is conductivity at low frequency at various temperature between 160 and 200°C. As expected, at high temperature and low frequency, the  $\varepsilon''$  is increased mainly due to the increase of the dc conductivity [23, 24]. From the fitted results, we can obtain the dc conductivity for the CCTO ceramics at different temperatures and then we can fit  $\sigma_{dc}$  also by following the Arrhenius law of

$$\sigma_{\rm dc} = \sigma_{\rm dc}^0 \exp(-E_{\rm dc}/k_B T),\tag{7}$$

where  $\sigma_{\rm dc}^0$  is the pre-exponential factor,  $E_{\rm dc}$  is the activation energy for the dc conductivity. The correlation of these values is shown in Fig. 10. From the fitting, we obtain the activation energy of the dielectric relaxation for CCTO\_PVA700 and CCTO\_PVA800 to be 0.132 and 0.112 eV, respectively. These values are close to the activation energy derived from Debye-like relaxation peak.

To interpret the dielectric in the CCTO ceramics, the Maxwell-Wagner relaxation was used to describe a series

array of two sub-circuits, one in the grain and the other at the grain boundaries [6, 8]. In each sub-circuit, the resistor and capacitor are in parallel. In this circuit, we can present the dielectric relaxation time,  $\tau$ , in the following form

$$\tau = \frac{R_g R_{gb} (C_g + C_{gb})}{R_g + R_{gb}},\tag{8}$$

where  $C_g$  and  $C_{gb}$  are the capacitance of grain and grain boundaries, respectively;  $R_g$  and  $R_{gb}$  are the resistor of grain and grain boundaries, respectively; and  $\tau$  is the time constant

Using the conditions,  $R_{gb} \gg R_g$  and  $C_{gb} \approx 10C_g$  [6, 8], we can approximately obtain the time constant,  $\tau$ , from (8)

$$\tau \approx R_g C_{gb} = (R_g C_g) \frac{C_{gb}}{C_g} = \tau_g \frac{C_{gb}}{C_g}, \tag{9}$$

where  $\tau_g = R_g C_g$  is the response time of the grain. It has been reported that  $C_g$  and  $C_{gb}$  are independent of tempera-

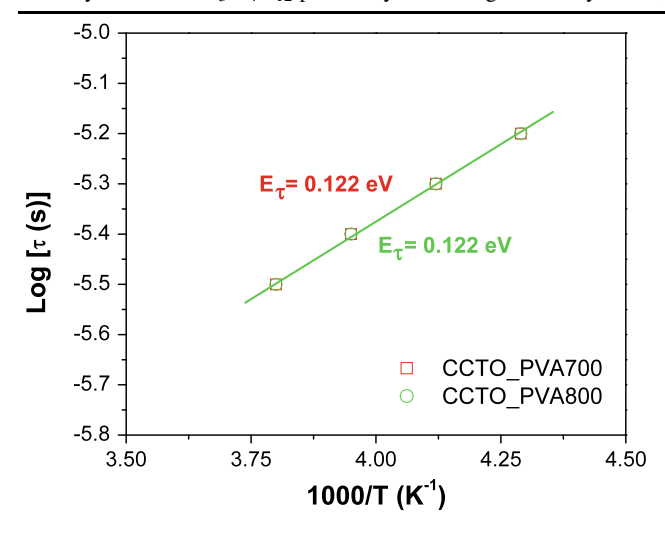
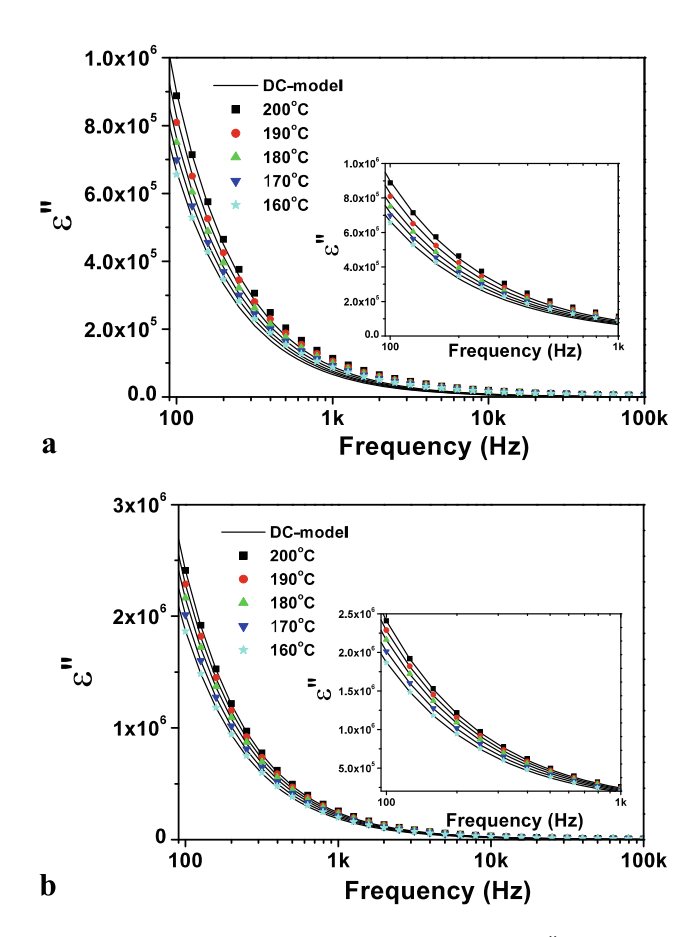
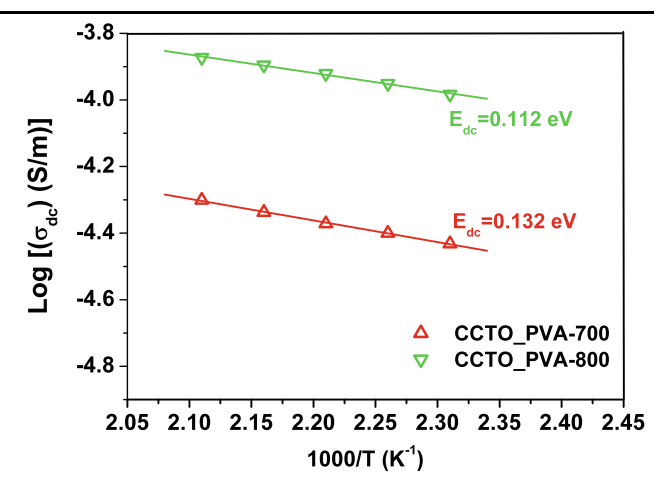


Fig. 8 Arrhenius plot of the relaxation time,  $\tau$ , for the sintered CCTO ceramics



**Fig. 9** The frequency dependence of the dielectric loss  $\varepsilon''$  at high temperature ranging between 160 and 200°C for **a** CCTO\_PVA700, and **b** CCTO\_PVA800, respectively. The *solid lines* are the fits according to (6)

ture [8]; thus, we can deduce  $\tau_g$  that follows the Arrhenius law, (5). Let  $\tau_g = \tau_g^0 \exp(E_g/k_BT)(\tau_g^0)$  is pre-exponential



**Fig. 10** Arrhenius plot of dc conductivity,  $\sigma_{dc}$ , for the CCTO ceramics

factor and  $E_g$  is the activation energy of the grain conduction process), then we modify (9) to

$$\tau \approx R_g C_{gb} = \frac{C_{gb}}{C_g} \left( \tau_g^0 \exp(E_g / k_B T) \right). \tag{10}$$

From (10),  $\tau$  and  $\tau_0$  have the same temperature dependence and the electrical response of the grains has the same activation energy as that of the observed dielectric relaxation. Thus, we conclude that the activation energy for the response of the grains in CCTO\_PVA700 and CCTO\_PVA800 are 0.122 eV, which are close to the values of 0.109 eV for a chemical solution synthesized CCTO [6]. However, the value of 0.122 eV is lager than 0.08 eV, which was reported for samples made by solid-state reaction [8].

At the present, the origin of semi-conducting grains and insulating grain boundaries has not been clearly established. Liu et al. [6] have proposed that the grains made by different method could have very different electrical property. Therefore, the larger activation energy of grains in CCTO\_PVA700 and CCTO\_PVA800 compared to that of a sample made by solid-state reaction implies that there are fewer oxygen vacancies in the grains of CCTO\_PVA700 and CCTO\_PVA800. This is reasonable because CCTO\_PVA700 and CCTO\_PVA800 were sintered from powders, which were calcined at low temperature (700 and 800°C) compared to the temperature needed for the solid-state processing. However, it is premature to associate the increase in grain activation energy of all CCTO ceramics with its large dielectric constant.

Finally, let us consider the role of CaTiO<sub>3</sub> secondary phase for the giant dielectric response in our CCTO samples. From the XRD analysis, we know that a small amount of CaTiO<sub>3</sub> secondary phase exists in our CCTO ceramics. Thus, the influence of CaTiO<sub>3</sub> secondary phase cannot be ignored. If considering that the segregated CaTiO<sub>3</sub> content is dispersed at the grain boundaries. CaTiO<sub>3</sub> is a dielectric



insulator with  $\varepsilon' \sim 200$  [25]. It is suggested that CaTiO<sub>3</sub> secondary phase acts as the barrier layers at the grain boundaries [26], which contribute largely to the high dielectric constant observed in our CCTO ceramics.

#### 4 Conclusions

Nanocrystalline CCTO powders have been synthesized by a simple PVA sol–gel route. The synthesized powders were characterized by TG-DTA, XRD, FTIR, SEM and TEM. The powders calcined at 700 and 800°C were used to prepared bulk CCTO ceramics, which were sintered at 1100°C for 16 h. The giant dielectric constant is in the order of  $10^4$ – $10^5$ . The dielectric behavior of all CCTO ceramics exhibits Debye-like relaxation which can be explained based on Maxwell–Wagner polarization mechanism.

Acknowledgements The authors would like to thank the Department of Chemistry, Khon Kaen University for providing TG-DTA facility, and the Faculty of Science Electron Microscopy Unit, Khon Kaen University for providing SEM facility. C. Masingboon would like to thank the University Staff Development Program, Kasetsart University Chalermphrakiat Sakon Nakhon Province Campus, Thailand for financial support of his PhD study. This work is financially supported by The Commission on Higher Education (CHE) and Thailand Research Fund (TRF).

# References

- 1. R.J. Cava, J. Mater. Chem. 11, 54 (2001)
- A.P. Ramirez, M.A. Subramanian, M. Gardel, G. Blumberg, D. Li, T. Vogt, S.M. Shapiro, Solid State Commun. 115, 217 (2000)
- M.A. Subramanian, L. Dong, N. Duan, B.A. Reisner, A.W. Sleight, J. Solid State Chem. 151, 323 (2000)
- 4. C.C. Homes, T. Vogt, S.M. Shapiro, S. Wakimoto, A.P. Ramirez, Science 293, 73 (2001)

- P. Thongbai, C. Masingboon, S. Maensiri, T. Yamwong, S. Wongsaenmai, R. Yimnirun, J. Phys., Condens. Matter 19, 236208 (2007)
- J. Liu, Y. Sui, C. Duan, W.N. Mei, R.W. Smith, J.R. Hardy, Chem. Mater. 18, 3878 (2006)
- 7. S. Chung, I. Kim, S. Kang, Nat. Mater. 3, 774 (2006)
- D.C. Sinclair, T.B. Adams, F.D. Morrison, A.R. West, Appl. Phys. Lett. 80, 2153 (2002)
- 9. B.A. Bender, M.J. Pan, Mater. Sci. Eng. B 117, 339 (2005)
- 10. T.T. Fang, H.K. Shiau, J. Am. Ceram. Soc. 87, 2072 (2004)
- P. Lunkenheimer, V. Bobnar, A.V. Pronin, A.I. Ritus, A.A. Volkov, A. Loidl, Phys. Rev. B 66, 052105 (2002)
- P. Lunkenheimer, R. Fichtl, S.G. Ebbinghaus, A. Loidl, Phys. Rev. B 70, 172102 (2004)
- M.H. Cohen, J.B. Neaton, L.X. He, D. Vanderbilt, J. Appl. Phys. 94, 3299 (2003)
- B.L. Cushing, V.L. Kolesnichenko, C.J. O'Connor, Chem. Rev. 104, 3893 (2004)
- 15. P. Jha, A.K. Arora Pand Ganguli, Mater. Lett. 57, 2443 (2003)
- C. Masingboon, P. Thongbai, S. Maensiri, Adv. Sci. Technol. 45, 2345 (2006)
- S. Jin, H. Xia, Y. Zhang, J. Guo, J. Xu, Mater. Lett. 61, 1404 (2007)
- L. Liu, H. Fan, P. Fang, L. Jin, Solid State Commun. 142, 573 (2007)
- B.D. Cullity, S.R. Stock, *Elements of X-ray Diffraction* (Prentice Hall, New Jersey, 2001)
- A.F.L. Almeida, R.S. de Oliveira, J.C. Góes, J.M. Sasaki, A.G. Souza Filho, J. Mendes Filho, A.S.B. Sombra, Mater. Sci. Eng. B 96, 275 (2002)
- C.L. Kretly, A.F.L. Almeida, P.B.A. Fechine, R.S. De Oliveira, A.S.B. Sombra, J. Mater. Sci.: Mater. Electronics 15, 657 (2004)
- M.A. Ramirez, P.R. Bueno, J.A. Varela, E. Longo, Appl. Phys. Lett. 89, 212102 (2006)
- S. Maensiri, P. Thongbai, T. Yamwong, Acta. Mater. 55, 2851 (2007)
- 24. J. Wu, C.W. Nan, Y. Lin, Y. Deng, Phys. Rev. Lett. **89**, 217601
- V.V. Lemanov, A.V. Sotinkov, E.P. Smirnova, M. Weihnacht, R. Kunze, Solid State Commun. 110, 611 (1999)
- S.F. Shao, J.L. Zhang, P. Zheng, C.L. Wang, J.C. Li, M.L. Zhao, Appl. Phys. Lett. 91, 042905 (2007)







MATERIALS CHEMISTRY AND PHYSICS

Materials Chemistry and Physics 109 (2008) 262-270

www.elsevier.com/locate/matchemphys

# Synthesis and giant dielectric behavior of CaCu<sub>3</sub>Ti<sub>4</sub>O<sub>12</sub> ceramics prepared by polymerized complex method

Chivalrat Masingboon<sup>a</sup>, Prasit Thongbai<sup>a</sup>, Santi Maensiri<sup>a,\*</sup>, Teerapon Yamwong<sup>b</sup>, Supapan Seraphin<sup>c</sup>

Received 7 August 2007; received in revised form 7 November 2007; accepted 13 November 2007

#### **Abstract**

Nano-sized powders of  $CaCu_3Ti_4O_{12}$  were synthesized by a polymerized complex method and calcined at 600, 700 and 800 °C in air for 8 h. The diameter of the powders ranges from 30 to 100 nm. The  $CaCu_3Ti_4O_{12}$  powders were characterized by TG-DTA, XRD, FTIR, SEM and TEM. Sintering of the powders was conducted in air at 1100 °C for 16 h. The XRD results indicated that all sintered samples have a typical perovskite  $CaCu_3Ti_4O_{12}$  structure with some amount of  $CaTiO_3$  and CuO. SEM micrographs of the sintered  $CaCu_3Ti_4O_{12}$  ceramics showed the average grain size of  $10-15~\mu m$ . The samples exhibit a giant dielectric constant,  $\varepsilon'$  of 10,000-20,000. It is found that  $\varepsilon$  is independent on the frequency and weakly dependent on temperature. The Maxwell–Wagner polarization mechanism is used to explain the high permittivity in these ceramics. It is also found that all three sintered samples have the same activation energy of grains, which is 0.116~eV. On the other hand, the activation energy of grain boundaries is found to be 0.219, 0.391 and 0.641~eV for  $CaCu_3Ti_4O_{12}$  ceramics prepared using the  $CaCu_3Ti_4O_{12}$  powders calcined at 600, 700 and 800 °C, respectively.

© 2007 Elsevier B.V. All rights reserved.

Keywords: Powder processing; Electron diffraction; Scanning electron microscopy; X-ray diffraction (XRD); Dielectrics

# 1. Introduction

Dielectric materials with high dielectric constant, good thermal stability and Ba/Pb-free have particularly attracted ever-increasing attention for their practical applications in microelectronics such as capacitors and memory devices. Recently, there has been a great interest in synthesis and characterization of a perovskite-type compound, calcium copper titanate (CaCu<sub>3</sub>Ti<sub>4</sub>O<sub>12</sub>, commonly called CCTO) [1–14]. This non-ferroelectric material, unlike commonly used ferroelectrics, exhibits giant dielectric constant of  $\varepsilon' \sim 10^4$  for polycrystalline ceramics [1,2] and  $\varepsilon' \sim 10^5$  (for single crystals) [3] in the kilohertz region over a large temperature range (from 100 to 600 K). This material does not undergo any structural change over the same temperature range although its dielectric constant abruptly

decreases to less than 100 below 100 K, showing a Debye-like relaxation [13]. In addition to its interesting dielectric property,  $CaCu_3Ti_4O_{12}$  has remarkably strong linear current–voltage characteristics without the addition of dopants [15]. These excellent properties render this material particularly attractive for a wide range of applications.

So far, several explanations for the origin of the colossal dielectric property of CaCu<sub>3</sub>Ti<sub>4</sub>O<sub>12</sub> material have been proposed to be due to either intrinsic or extrinsic effect. Since the giant dielectric response of this material was found to be very sensitive to the microstructure (such as grain size) and processing conditions (such as sintering temperature and time, cooling rate and partial pressure) [11–13,16,17], more investigations tend to believe that the high dielectric constant originates from the extrinsic effect such as internal barrier layer capacitor (IBLC) [11,16], contact-electrode effect [18,19], and special inhomogenity of local dielectric response [20]. Although still unclear, the IBLC explanation of extrinsic mechanism is widely accepted at the present stage [21–26].

<sup>\*</sup> Corresponding author. Tel.: +66 43 202222–9x2248; fax: +66 43 202374. *E-mail addresses:* sanmae@kku.ac.th, santimaensiri@gmail.com
(S. Maensiri).

CCTO was generally prepared by a standard solid-state reaction method [1–3]. This method requires tedious work and a high temperature in the powder preparation process. Moreover, it suffers from the disadvantages of inhomogeneity. In contrast, synthesis from a solution affords the reaction with a homogeneous mixing of the metal ions at the atomic scale, shorter reaction time and at lower temperature [13]. However, it has been only a few reports on the solution methods to synthesize CCTO [8,10,13].

In this paper, we report the synthesis and giant dielectric properties of CCTO prepared by polymerized complex (PC) method. The PC method is a chemical solution process, which has received considerable attention due to its relative simplicity and usefulness for obtaining a homogeneous and fine powder precursor. The synthesized fine CCTO powders were characterized by thermogravimetric and differential thermal analysis (TG-DTA), X-ray diffraction (XRD), Fourier-transform infared (FT-IR) spectroscopy, scanning electron microscopy (SEM) and transmission electron microscopy (TEM). The effects of particle size of the synthesized powders on microstructure and giant dielectric behavior of the sintered CCTO were also investigated.

# 2. Experimental procedure

The nano-sized powders of the CCTO were prepared by a simple modified sol-gel method. The PC method was first developed by Pechini [27] and has been used to synthesize polycations oxides powders [28–35]. It is based on metallic citrate polymerization with the use of ethylene glycol. A hydrocarboxylic acid, such as citric acid, is used to chelate cations in aqueous solution. The addition of a glycol, such as ethylene glycol, leads to organic ester formation. Polymerization, promoted by heating the mixture, results in a homogeneous resin in which metal ions are uniformly distributed throughout the organic matrix. To prepare the CCTO powders, citric acid (99.7% purity, BDH, England) was first dissolved in ethylene glycol (99.5% purity, Carlo Erba Reacgenti, Italy) by heating and stirring at 80 °C. Subsequently, Ca(NO<sub>3</sub>)<sub>2</sub>·4H<sub>2</sub>O (99.9% purity, Kento, Japan), Cu(NO $_3)_2 \cdot 4H_2O~(99.5\%~purity, Carlo Erba Reacgenti, Italy) and$ 75 wt% titanium(diisoproproxide) bis(2,4-pentanedionate) in 2-propanol (99%, Acros organics, USA) in a mole ratio corresponding to the nominal composition of CaCu<sub>3</sub>Ti<sub>4</sub>O<sub>12</sub>. Citric acid and ethylene glycol were mixed in the respective proportions of 4 and 16 moles for each mole of metal cation. The transparent blue-colored mixture was then stirred at 280 °C until the formation of the dark blue-colored polymer between ethylene glycol and metal citrate complexes was promoted (for about 10h). As the colloidal solution was condensed, it became highly viscous. This viscous polymeric product was decomposed to a dark mass precursor at 350 °C for several hours in air. This black-solid mass precursor was ground, passed through 106 µm sieve (Test sieve, Endecotts Limited, England) and each separate portion calcined at 600, 700 and 800 °C for 8 h in air. The calcined powder precursors were reground and passed through  $106\,\mu m$  sieve again to break up large agglomerates. The final products were black powders. The prepared CCTO powers were characterized by TG-DTA (Pyris Diamond TG/DTA, PerkinElmer Instrument, USA), X-ray diffraction (PW3040 Philips X-ray diffractometer with Cu K $\alpha$  radiation ( $\lambda = 0.15406$  nm), The Netherlands), Fourier transform infrared spectrometer (Spectrum One FT-IR Spectrometer, PerkinElmer Instruments, USA), scanning electron microscopy (LEO SEM VP1450, UK) and transmission electron microscopy (TEM, Hitachi H8100 200 kV). The sieved powders were pressed uni-axially in a 16 mm die with an applied pressure of 100 MPa. The compacts were pressureless-sintered at 1100 °C for 16 h in air in a box furnace, heating and cooling rates of 5 °C min<sup>-1</sup>. The sintered disc samples of  $\sim$ 11 mm in diameter with a thickness of  $\sim$ 2 mm were obtained. The average grain size of each sintered CCTO ceramic was measured using a standard line intercept technique from SEM micrographs of sintered CCTO surfaces and counting at least 200 intercepts for each micrograph. Throughout this article, we assigned symbols of CCTO\_PC600, CCTO\_PC700

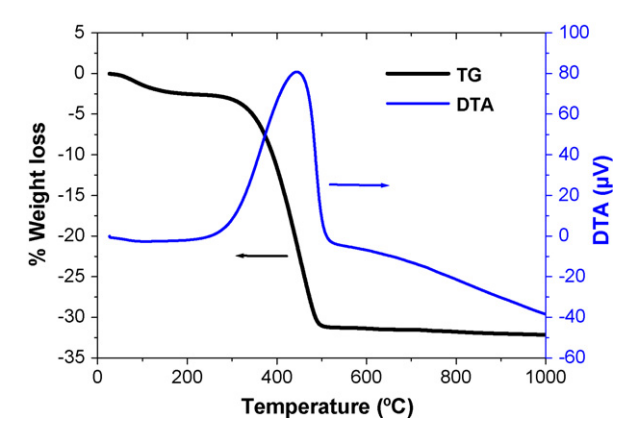


Fig. 1. The TG-DTA curves of the thermal decomposition of CCTO precursor at a heating rate of  $15\,^{\circ}\text{C}$  min $^{-1}$  in static air.

and CCTO\_PC800 for the CCTO bulk samples fabricated using the powders calcined at 600, 700 and 800 °C, sintered in air at 1100 °C for 16 h, respectively.

The capacitance, C, and loss tangent,  $\tan \delta$ , were carried out as a function of frequency (100 Hz–1 MHz) and temperature ( $-50\,^{\circ}\mathrm{C}$  to  $-200\,^{\circ}\mathrm{C}$ ), using a Hewlett Packard 4194A Impedance Gain Phase Analyzer at an oscillation voltage of 1 V. Each measured temperature was kept constant with an accuracy of  $\pm 1\,^{\circ}\mathrm{C}$ .

The complex permittivity,  $\varepsilon^*$ , was calculated as follows:

$$\varepsilon^* = \varepsilon' - i\varepsilon'' \tag{1}$$

where

$$\varepsilon' = \frac{Cd}{\varepsilon_0 A} \tag{2}$$

$$\varepsilon'' = \varepsilon' \tan \delta \tag{3}$$

where  $\varepsilon_0$  is the permittivity in free space, A is the sample area and d is the sample thickness.

# 3. Results and discussion

Fig. 1 shows the thermal analysis, TG-DTA curves of the powder precursor of CCTO firing with a heating rate of 15 °C min<sup>-1</sup> in static air from room temperature to 1000 °C. The TG curve shows a major weight loss from 300 to  $\sim$ 500 °C; no further weight loss was observed up to 1000 °C. The weight loss is related to the combustion of organic matrix. The clear plateau formed between 500 and 1000 °C on the TG curve indicates the formation of CCTO as decomposition product, as confirmed by XRD analysis (discuss in detail later). On the DTA curve, a main exothermic effect were observed between 300 and 500 °C with maxima at 450 °C, indicating that the thermal events was associated with the burnout of organic species involved in the precursor powders (organic mass remained from citric acid and ethylene glycol), of the residual carbon or due to direct crystallization of CCTO from the amorphous component. No further weight loss and no thermal effect were observed above 500 °C, indicating that no decomposition occurs above this temperature. Note that these precursors were calcined in air at 600, 700 and  $800\,^{\circ}\text{C}$  for  $8\,\text{h}$ .

Fig. 2 shows XRD patterns of CCTO powders after calcination in air at (a) 600 °C, (b) 700 °C and (c) 800 °C for 8 h. The main peaks of all calcined CCTO powders are compara-

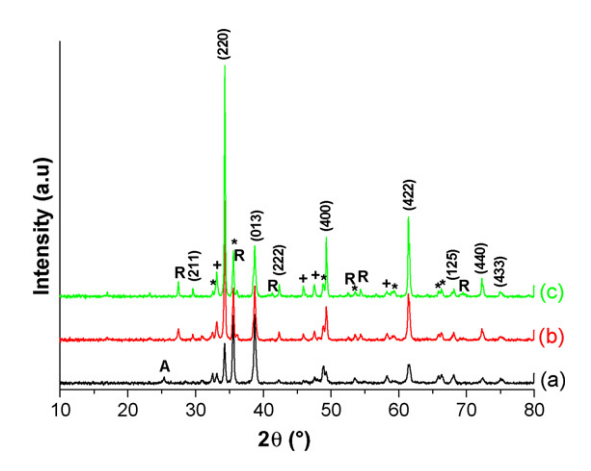


Fig. 2. XRD patterns of CCTO powders calcined for 8 h in air at (a)  $600\,^{\circ}$ C, (b)  $700\,^{\circ}$ C and (c)  $800\,^{\circ}$ C, respectively. +CaTiO<sub>3</sub>, \*CuO, A Anatese TiO<sub>2</sub> and R Rutile TiO<sub>2</sub>.

ble to those of the standard powder XRD pattern of CCTO in the JCPDS card No. 75-2188. In addition, the following phases of CaTiO3 (JCPDS card No. 82-0228), CuO (JCPDS card No. 80-0076), Anateses-TiO<sub>2</sub> (JCPDS card No. 78-2486) and Rutile-TiO<sub>2</sub> (JCPDS card No. 87-0920) were also observed. It is suggested by Guilleemet-Fritsch et al. [36] that the pure CCTO phase is obtained only when the ratio of calcium, copper and titanium are close to the stoichiometric ones. The CaTiO<sub>3</sub> and TiO<sub>2</sub> phase appear if an excess of titanium is present. It is the excess of titanium that leads to the precipitation of CaTiO<sub>3</sub> and TiO<sub>2</sub>, even if there is no excess of calcium [36]. The formation of CaTiO<sub>3</sub> may also cause the excess of Cu with respect with the stoichiometry of CCTO. As a result, the precipitation of the CuO is observed. From the line broadening of the main peaks, the crystallite size (D) was estimated using the Scherrer formula [37]:

$$D = \frac{K\lambda}{(\beta\cos\theta)} \tag{4}$$

where  $\lambda$  is the wavelength of the X-ray radiation, K is a constant taken as 0.9,  $\theta$  is the diffraction angle.  $\beta$  is the full width at haft maximum (FWHM) and is given by  $\beta = (\beta_o^2 - \beta_i^2)^{1/2}$ , where  $\beta_o$  and  $\beta_i$  are the widths from the observed X-ray peak and the width due to instrumental effects, respectively. The particle sizes are found to be  $43.8 \pm 15.6$ ,  $55.4 \pm 20.1$  and  $70.9 \pm 22.6$  nm for the powders calcined at 600, 700 and 800 °C, respectively.

Fig. 3 shows FT-IR spectra of CCTO powders after calcination in air at 600, 700 and 800 °C for 8 h. All three samples show the main absorption bands at 561, 516 and 437 cm<sup>-1</sup>. These bands are assigned to the absorption regions for Ti ion, which are associated to  $\nu_{\text{Ti-O}}$  of 653–550 cm<sup>-1</sup> and  $\nu_{\text{Ti-O-Ti}}$  of 495–436 cm<sup>-1</sup> [4].

Morphology and microstructure of the calcined CCTO powders and sintered CCTO ceramic samples revealed by SEM are shown in Fig. 4. Fig. 4(a)–(c) shows CCTO particles with sizes of about 50, 80 and 100 nm for the 600, 700 and 800 °C calcined samples, respectively. These values were larger than those obtained from X-ray line broadening calculation. Some agglomerates were observed in all of the calcined powders.

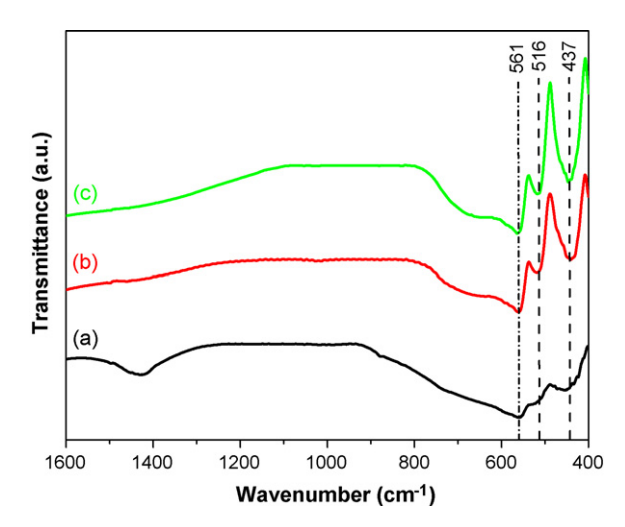


Fig. 3. FT-IR spectra of CCTO powders calcined for 8 h in air at (a)  $600\,^{\circ}$ C, (b)  $700\,^{\circ}$ C and (c)  $800\,^{\circ}$ C, respectively.

The particle size of the powder increased with increasing calcination temperature. After sintering at  $1100\,^{\circ}\text{C}$  for 16 h, the bulk CCTO ceramics with different microstructure were obtained. The CCTO\_600 (Fig. 4(d)), CCTO\_700 (Fig. 4(e)) and CCTO\_800 (Fig. 4(f)) showed a mean grain size of  $11.9 \pm 4.0 \,\mu\text{m}$ ,  $14.8 \pm 6.2 \,\mu\text{m}$  and  $10.8 \pm 4.5 \,\mu\text{m}$ , respectively.

Fig. 5 shows TEM images and the corresponding selected area electron diffraction (SAED) patterns of the calcined CCTO powders. It is clearly seen from the TEM bright-field images that all of the samples are consist of nanocrystalline CCTO particles, whose size increases with increasing calcination temperature. The 600 °C calcined sample contains nanoparticles of  $30.9 \pm 7.8$  nm in size whereas the 700 °C calcined sample contains nanoparticles of  $58.7 \pm 45.4$  nm. As expected, the 800 °C calcined sample consists of nanoparticles with the largest particle sizes of  $85.3 \pm 39.9$  nm. It is noted that the particle sizes observed by TEM are not in agreement with results determined by XRD and SEM (see Table 1). The error in the particle sizes obtained from the XRD results is large, and the average values obtained from SEM are significantly larger than that obtained from XRD. These differences could be resulted from some dispersion or inhomogeneity in the particles size of the samples. Electron diffraction of particles with higher calcination temperature contains more intense spots as shown in the 700 and 800 °C calcined powders, indicating the larger particle size of highly crystalline compared to the 600 °C calcined samples. The interplanar spacings  $(d_{hkl})$  measured from the selected-area electron diffraction patterns are in good agreement with the values

Table 1 Summary of particle size analysis obtained from XRD and TEM; and lattice parameter (from XRD) of CCTO powders compared to the ASTM value

Material	Particle size from XRD (nm)	Particle size from TEM (nm)	Lattice parameter <i>a</i> (Å)
ASTM (75-2188)	_	_	$7.391 \pm 0.001$
600 °C powders	$43.8 \pm 15.6$	$30.9 \pm 7.8$	$7.374 \pm 0.002$
700 °C powders	$55.4 \pm 20.1$	$58.7 \pm 45.4$	$7.389 \pm 0.001$
800 °C powders	$70.9 \pm 22.6$	$85.3 \pm 39.9$	$7.398 \pm 0.002$

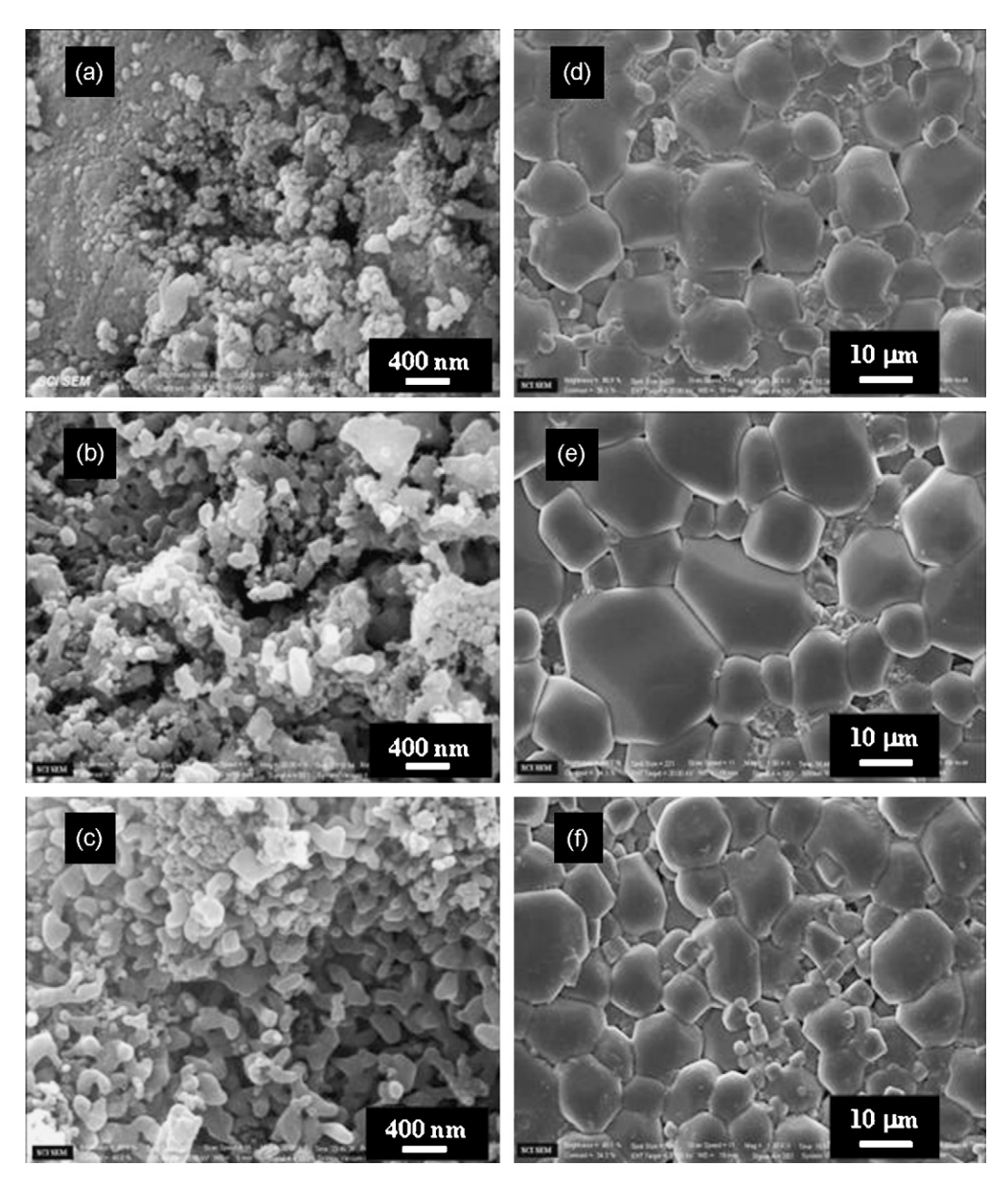


Fig. 4. SEM micrographs of the CCTO powders and sintered CCTO materials. (a)–(c) are the powders calcined for 8 h in air at 600, 700 and 800 °C, respectively. (d)–(f) are the microstructure of the sintering CCTO\_PC600, CCTO\_PC700 and CCTO\_PC800, respectively.

obtained from the standard data JCPDS: 75-2188 (for CCTO) and 89-0056 (for CaTiO<sub>3</sub>) as summarized in Table 2.

Fig. 6 shows XRD patterns of the CCTO ceramics sintered in air at 1100 °C for 16 h, confirming a single phase of CCTO in all the samples although a small amount of CaTiO<sub>3</sub> and CuO were present in all the sintered samples. The presence of additional CaTiO<sub>3</sub> in the sintered samples is possibly due to the presence of excess titanium as suggested Guilleemet-Fritsch et al. [36]. Therefore, we think that the excess of titanium leads to the precipitation of CaTiO<sub>3</sub> in our sintered samples. For the presence of the CuO phase, it is possible that the Cu rich phase derives from the diffusion of Cu to the defects present, after which gross excess causes the crystallization of the separate CuO phase [38]. The CuO phase within the ceramics implies that excess copper

is in the form of a copper rich phase at the grain boundaries [38,39]. However, further work on careful investigation of the stoichiometry of the CCTO ceramics using energy dispersive spectroscopy (EDS) is needed to confirm the Ca/Cu/Ti cationic ratio in our CCTO ceramics.

Fig. 7 shows the frequency dependence of the  $\varepsilon'$  and  $\varepsilon''$  of the sintered CCTO ceramics (CCTO\_PC600, CCTO\_PC700 and CCTO\_PC800) at various temperature between -50 and  $-10\,^{\circ}$ C. Fig. 7(a.1)–(c.1) shows that the CCTO ceramics (CCTO\_PC600, CCTO\_PC700 and CCTO\_PC800) have very high dielectric constant,  $\varepsilon'$ , of 10000–20000 at 1 kHz.  $\varepsilon'$  has little frequency dependence at low frequency (below 100 kHz). The high  $\varepsilon'$  at low frequency may possibly be a contribution from grain boundary in these sintered CCTO ceramics [40]. The val-

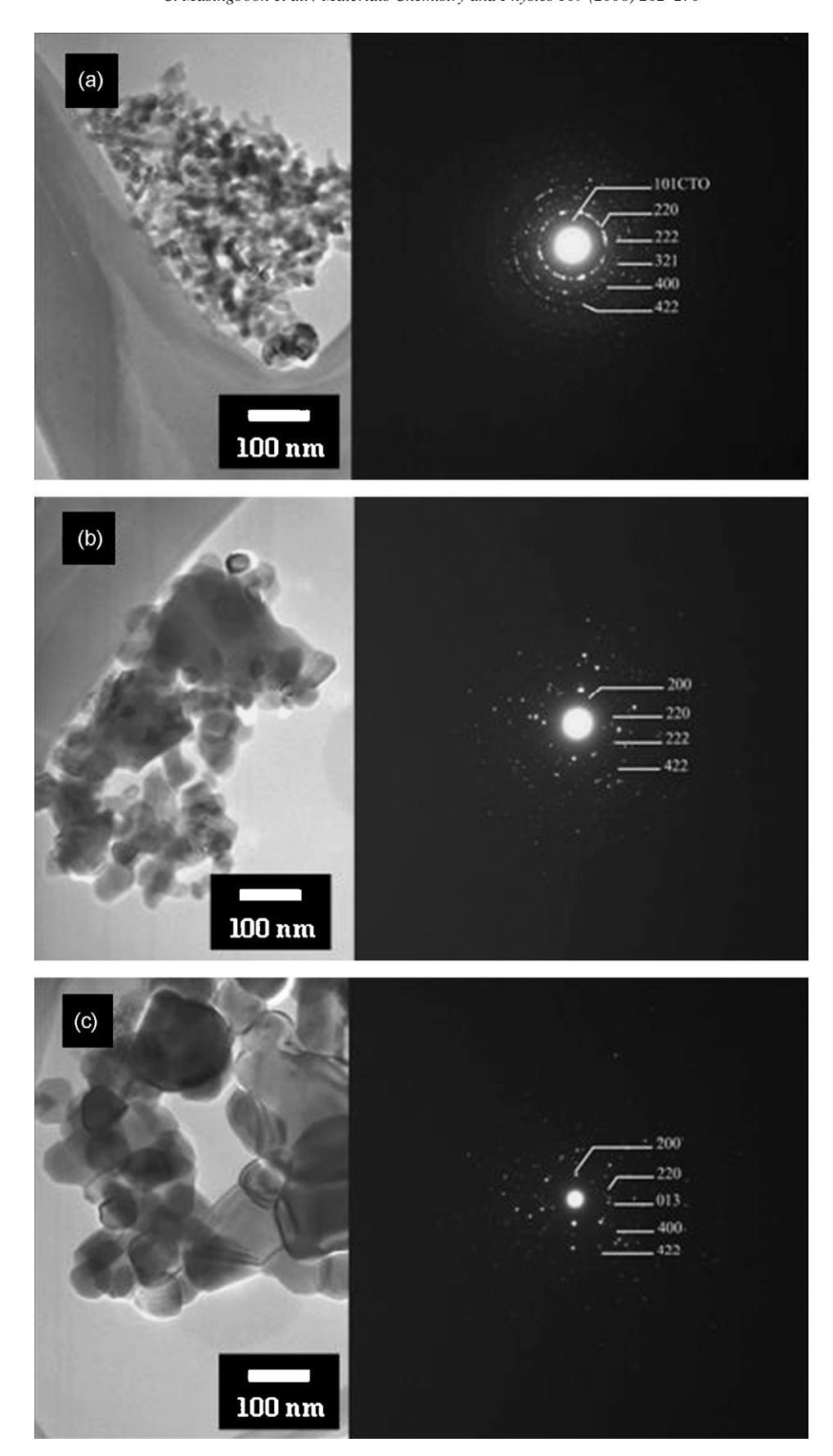


Fig. 5. Bright field TEM images with corresponding selected-area electron diffraction (SAED) patterns of CCTO powders calcined in air for 8 h: (a)  $600\,^{\circ}$ C; (b)  $700\,^{\circ}$ C; (c)  $800\,^{\circ}$ C, respectively. 101CTO stands for (1 0 1) plane of CaTiO<sub>3</sub>.

Table 2 Measured interplanar spacings ( $d_{hkl}$ ) obtained from selected-area electron diffraction patterns of CCTO samples calcined at 600, 700 and 800 °C for 8 h shown in Fig. 5

	Measured interplanar	Measured interplanar spacing of CCTO samples $d_{hkl}$ (Å)			Standard data (JCPDS: 75-2188)	
	600°C powder	700°C powder	800 °C powder	$d_{hkl}$ (Å)	hkl	
$R_1$	_	3.5735	3.5735	3.6955	200	
$R_2$	2.6703	2.6413	2.6557	2.6131	220	
$R_3$	_	_	2.3143	2.3372	013	
$R_4$	2.1696	2.1504	_	2.1336	222	
R <sub>5</sub>	1.9597	_	_	1.9753	321	
$R_6$	1.7802	_	1.7868	1.8477	400	
R <sub>7</sub>	1.567	1.5379	1.5527	1.5086	422	

Corresponding values from the standard data JCPDS: 75-2188 are also provided for a comparison.

ues are similar to the those reported by Jin et al. [10] and Liu et al. [13], who reported values of  $\varepsilon' \sim 10^4$  (at 1 kHz) for samples prepared from a solution route; and by Ramirez et al. [1] and Bender and Pan [12], whose samples prepared from a solid-state reaction method. These values, however, are much higher than 3000 of the sol–gel synthesized CCTO ceramics reported by Jha et al. [8].

The frequency dependence of the observed dielectric relaxation,  $\varepsilon''$ , shown in Fig. 7(a.2)–(c.2). By considering these results, we cannot apply the empirical Cole–Cole relation to fit these data because at low frequency the samples contain numerous grain boundaries or grain boundaries relaxation [40]. However, we can apply the Debye-like relaxation peak due to the presence of the grains. The  $\varepsilon''$  shows a clear Debye-like relaxation peak shifting from a constant value at low frequency to a small saturated value at higher frequency. The electrical response from grains has a very high response frequency because of their small resistance and capacitance [13]. We can determine the dielectric relaxation time,  $\tau$ , also by following the Arrhenius

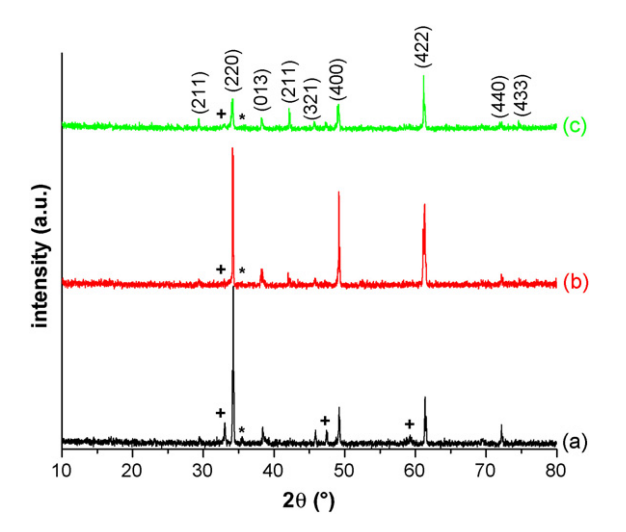


Fig. 6. XRD patterns of (a)  $600 \,^{\circ}$ C, (b)  $700 \,^{\circ}$ C and (c)  $800 \,^{\circ}$ C, respectively. All sintering was done in air at  $1100 \,^{\circ}$ C for 16 h. The indexed planes indicated in (c) pattern are for CCTO main structure. +CaTiO<sub>3</sub> and \* CuO.

law of

$$\tau = \tau_0 \exp\left(\frac{U}{k_{\rm B}T}\right) \tag{5}$$

where  $\tau_0$  is the pre-exponential factor, U is the activation energy for the relaxation,  $k_{\rm B}$  is the Boltzmann constant and T is the absolute temperature. Fig. 8 illustrates the relationship of  $\tau$  and T for all three CCTO samples. The activation energy of an electrical response, at different temperature can be derived from the response time ( $\tau = 1/2\pi f$ , where f is the response frequency at which the imaginary part of the complex impedance has a maximum). From the fitting (Fig. 8), we obtain the activation energy of the dielectric relaxation for CCTO\_PC600, CCTO\_PC700 and CCTO\_PC800 to be of the same value of 0.116 eV.

Fig. 9 shows the fit of the  $\epsilon''$  of the CCTO ceramics (CCTO\_PC600, CCTO\_PC700 and CCTO\_PC800) to equation [41]

$$\varepsilon'' pprox \frac{\sigma_{
m dc}}{\varepsilon_0 \omega}$$
 (6)

where  $\sigma_{dc}$  is conductivity at low frequency at various temperature between 160 and 200 °C. As expected, at high temperature and low frequency, the  $\varepsilon''$  is increased mainly due to the increase of the dc conductivity [34,42]. From the fitted results, we can obtain the dc conductivity for the CCTO ceramics at different temperatures and then we can fit  $\sigma_{dc}$  also by following the Arrhenius law of

$$\sigma_{\rm dc} = \sigma_{\rm dc}^0 \exp\left(\frac{U_{\rm dc}}{k_{\rm B}T}\right) \tag{7}$$

where  $\sigma_{dc}^0$  is the pre-exponential factor,  $U_{dc}$  is the activation energy for the dc conductivity. The correlation of these values is shown in Fig. 10. From the fitting, we obtain the activation energy of the dielectric relaxation for CCTO\_PC600, CCTO\_PC700 and CCTO\_PC800 to be 0.219, 0.391 and 0.647 eV, respectively. These values are close to the activation energy of the grain boundaries reported earlier in the literature for the CCTO, 0.24 [9], 0.34 [26] and 0.60 eV [11]. Our results support the hypothesis of the existence of internal barrier layers between the grains. In other words, our results indicate that the behavior of  $\varepsilon''$  at low frequency (in Fig. 7) is a result of the grain boundaries barrier.